PHOTOLUMINESCENCE AND RAMAN CHARACTERIZATION OF PLEE AND MBE GROWN SEMICONDUCTOR EPILAYERS

submitted in partial fufillment of
the Master of Science degree

by

DALE A. HARRISON ©

July, 1994

Department of Physics
Lakehead University
Thunder Bay, Ontario
Canada

ISBN 0-315-97044-8

Photoluminescence and Raman Characterization of PLEE and MBE Grown Semiconductor Epilayers

by

Dale A. Harrison

Submitted to the Department of Physics
on 21 July 1994, in partial fulfillment of the
requirements for the degree of
Master of Science

Abstract

Photoluminescence and Raman investigations of selected alloy semiconductor epilayers are reported. Correlations relating optical spectra and a number of intrinsic and extrinsic properties of the materials studied are found. Of particular interest, preliminary measurements on a promising new quaternary system (InGaAlAs/InP) are reported and mixed mode AlAs-like LO Raman scattering processes in this material are identified for the first time. In addition, evidence for defect related photoluminescence associated with the $E_o + \Delta_o$ energy gap region in CdTe is also reported.

Thesis Supervisor: Dr. W.J. Keeler
Title: Physics Chair, Lakehead University

Acknowledgments

I would like to express my sincere gratitude to my supervisor Dr. W.J. Keeler for his continued support and invaluable guidance throughout the last two years.

As well, I would like to thank Dr. M.H. Hawton for many helpful discussions regarding various sections of this work.

I also wish to thank Dr. Z.R. Wasilewski and Dr. J.J. Dubowski of the National Research Council for providing the high quality materials that formed the focus of this study.

Finally, I would like to thank my wife, Michelle, for her enduring patience and relentless support.

Contents

List of Figures

List of Tables

Chapter 1

Introduction

Semiconductors are of widespread interest because of the large number of devices (both electronic and opto-electronic) which can be made from them. Many different techniques designed to investigate the properties of these materials have been developed and applied to a large number of elemental and alloy (i.e. binary and ternary) compound semiconductors. Expansion into new classes of semiconductors has continued to the point where quaternary alloys are presently of special interest since they allow independent control of both the intrinsic band gap, E_g, and lattice constant of the material.

Materials are chosen as possible candidates for use in specific device applications based on a knowledge of their intrinsic structural properties. To further determine the suitability of a semiconducting material to a particular application, its electronic transport and radiative recombination properties must be considered. Hence, many of the subsequent assessment needs of such materials are concerned with the appropriate control of these attributes. Such properties ultimately depend on the presence or absence of appropriately selected impurities.

Semiconductor materials with all intrinsic and some extrinsic properties well suited to a particular application may not be usable, however, due to other hard to control extrinsic properties. For example, some wide-gap II-VI materials which are ideally suited for visible luminescence devices are not yet commercially available since the satisfactory, simultaneous control of both donor and acceptor dopant concentrations necessary to produce p-n junctions of appropriate quality has been difficult to achieve [1, 2]. One becomes very concerned with the relative proportions of these selected dopants and their spatial distribution throughout the crystal. As well, the detection and control of unwanted residual impurities and various

defects, whose influence is often quite significant, is also of fundamental importance. Many diverse assessment tools are employed to characterize the presence of such impurities and defects in these materials and a substantial fraction of these methods are based upon optical techniques.

While optical spectra are taken at a variety of temperatures, a substantially larger amount of information is usually obtained at temperatures $\leq 0.1\Theta_D$; where Θ_D is the Debye temperature[1] of the host lattice [3]. A significant loss of spectral information, resulting from thermal broadening of no-phonon lines and additional spectral obscuration by Stokes phonon replica's, is usually encountered by measurements taken at temperatures above this value. As a result, most optical measurements are taken in the lower part of the normal range of cryogenic temperatures, (i.e. below 77 K). The actual measurement temperature will depend primarily on the investigative technique employed, (i.e.luminescence measurements usually require lower temperatures than those of absorption). However, optical characterization techniques are not strictly limited to low temperature regions and are still capable of providing much useful information at higher temperatures [4, 5, 6].

The temperature region of interest for the operation of the large majority of semiconducting devices is quite often in excess of 300 K. While it is not intuitively obvious that low temperature optical characterization techniques can provide a wealth of useful information on room temperature device operation, there are in fact, numerous benefits associated with such measurements. Generally, optical techniques are both contact-less and highly sensitive. They allow for the fast acquisition of data on the presence and relative proportions of optically and/or electrically active impurity and defect centers incorporated into the lattice. In some cases, a single spectrum measured on one sample can provide definitive information on the precise role and manner of incorporation of the impurity in the semiconductor lattice. This includes the type of center (donor or acceptor), lattice site occupied and local symmetry. There are, however, downfalls associated with the ease and speed at which data can be collected using such methods. The abundance and complexity of information obtained in a low temperature optical measurement is quite often overwhelming, and the interpretation of results can be a difficult task. As with any assessment technique, a significant amount of background information is required before all of the information can be derived from the spectral context.

[1]The Debye temperature, Θ_D, depends on the mass and bonding between the host atoms and is usually in the range of 200 – 500 K for most semiconductors.

Materials	Crystal structure	Lattice constant	E_g (300 K)	E_g (4 K)
CdTe	Zinc-blende	6.478 Å	1.45 eV	1.61eV
CdMnTe	Zinc-blende	6.370 - 6.478 Å	1.45 - 2.78 eV	1.61-3.18 eV
InGaAlAs	Zinc-blende	5.869 Å	0.75 - 1.45 eV	0.81-1.58 eV
GaAs	Zinc-blende	5.642 Å	1.44 eV	1.52 eV
InSb	Zinc-blende	6.479 Å	0.24 eV	0.41 eV
InP	Zinc-blende	5.869 Å	1.35 eV	1.42 eV

Table 1.1: Intrinsic parameters of semiconductor compounds under investigation in this study.

The emphasis of this work will be directed at two optical characterization techniques, namely photoluminescence (PL) and Raman spectroscopy. These techniques will be employed to investigate the radiative recombination properties of a number of interesting and potentially important semiconducting materials. These materials and their possible applications can be divided into three categories.

1. II-VI/III-V heterostructures for use as both large area, low defect, II-VI growth platforms and quantum well lasers operating in the 0.2 - 0.5 eV energy range. Specifically, the materials investigated were CdTe epilayers grown on (111)GaAs and (001)InSb substrates, respectively. Both the epitaxially grown epilayers and bulk target materials used in the construction of these films were characterized.

2. Epilayers of diluted magnetic semiconductors suitable for incorporation into Faraday-effect-based devices. $Cd_{1-x}Mn_xTe$ epilayers deposited on (111)GaAs, for Mn (x) in the range ($0.44 \leq x \leq 0.69$) were investigated. Both the substrate and epilayer materials were studied.

3. Materials well-suited for use in high-speed optical communication systems operating in the $1.3 - 1.6$ μm range. Specifically, $In_{1-x-y}Ga_xAl_yAs$ epilayers lattice-matched to InP substrates (i.e. with $x + y \simeq 0.47$) were characterized in this work.

Some of the physical parameters of the heterostructures are listed in Table 1.1 (data was obtained from Refs. [7], [8], and [9], respectively).

In chapters 2 and 3, a brief theoretical treatment of photoluminescence recombination and Raman scattering will be presented. While a detailed review of these processes is beyond the scope of this work, an introduction to the basic mechanisms involved in these

phenomena is presented. The information provided in these chapters will be used later in chapter 5 to analyze and interpret the results of the experiments.

Chapter 4 will examine the experimental apparatus and methods used in this study. In chapter 5 the reasons for studying the various materials are reviewed in more detail and then results are presented and discussed. Correlations between the observed optical spectra and a number of intrinsic and extrinsic properties of the materials are described. Conclusions arrived at as a consequence of these discussions are summarized in chapter 6.

Chapter 2

Photoluminescence Theory

2.1 Introductory Concepts

Photoluminescence (PL) is the optical radiation emitted by a physical system (in excess of the thermal equilibrium blackbody radiation) resulting from excitation to a non-equilibrium state by irradiation with light. Three processes can be distinguished in this phenomena:

1. Electron-hole (e-h) pairs are created by the absorption of exciting radiation.
2. These carriers thermalize, migrate and subsequently radiatively recombine.
3. Photons resulting from this recombination escape from the sample.

In the ground state of an ideal, impurity-free, semiconducting crystal at low temperature there exist a set of fully occupied electronic energy levels (valence band), separated from a set of unoccupied levels (conduction band) by a finite energy gap. The origin of the energy gap can be viewed in terms of the covalent bonds between the atoms in the semiconductor. The valence band is composed of low-energy bonding states and the conduction band is composed of higher-energy anti-bonding states [10]. Electronic excitation in these crystals occurs when an electron from the filled valence band is promoted to the empty conduction band. This process leaves an unoccupied state in the otherwise occupied valence band which can be thought of as region of net positive charge in the crystal lattice, commonly referred to as a "hole". Once they are created in their respective bands the

electron and the hole quickly[1] proceed to the lowest energy state accessible to them. The electron drops to the bottom of the conduction band and the hole rises to the top of the valence band. Once in these energy states, the two interact through Coulombic attraction. The electronic state of the semiconducting crystal resulting from such an excitation was first discussed by Wannier [11] and is referred to as an exciton.[2]

Since the energy gaps of interest are typically no more than a few electron volts, the excitation processes usually takes place through the absorption of an optical photon. As energy must be conserved during this transition it follows that the energy of the exciting photon must be greater than or equal to that of the band gap, that is $h\nu \geq E_g$. Hence, neglecting other effects, a photon whose energy is less than that of the band gap energy of a crystal will propagate unattenuated through it. The energy at which the crystal starts to absorb radiation, E_g, is referred to as the fundamental absorption edge. The optical properties of crystals in the vicinity of the absorption edge are strongly influenced by the fact that the electron and hole produced in the excitation process interact with each other and usually combine to form excitons (to be discussed in section 2.2).

As a result of the absorption of photons with $h\nu \geq E_g$ near the surface of the crystal, an inhomogeneous and non-equilibrium carrier distribution is established in a restricted volume defined by the diffusion length of the incident radiation. In an attempt to regain homogeneity and equilibrium, the excess electron-hole pairs produced in this region quickly diffuse away from the surface of the crystal. The lifetime of the excitons produced within this region depends not only on the form of crystal lattice, but also on the types and concentrations of impurities, dislocations and defects within it. Eventually, however, the excitons will recombine radiatively or non-radiatively. Any non-radiative recombination events are not detected in the PL technique and subtract from the overall signal. Hence, we are primarily concerned with the radiative transitions as they are observable with very high sensitivity.

The theoretical description of exciton states in a solid is a many-body problem that cannot be solved without making numerous simplifying assumptions (see for example Refs. [12] and [13]). While it is not the purpose of this work to extensively review the details of the process, a basic understanding of exciton theory and how it relates to semiconductors

[1] Within time of the order of a nanosecond, the free carriers "thermalize" to a kinetic energy of approximately kT by the rapid creation of phonons.

[2] J. Frenkel first introduced the concept of the exciton in 1931. The localized model which formed the basis of his approach, however, was completely inadequate in describing the excited states in semiconductors.

is essential in designing, performing and analyzing successful PL experiments and will be examined briefly below.

2.2 Basic Excitonic Theory

Let us consider a semiconducting crystal with the electronic band structure as shown in Fig. 2.1. As mentioned earlier, in the ground state of such a crystal the lower (valence) band states are completely occupied while the upper (conduction) band states are empty. Low energy single-electron processes are shown in the figure by processes A and B. Process A represents the transfer of an electron from an initial state near the valence band maximum to a state with the same wave vector, $\vec{k}$, near the conduction band minimum. This process can occur with the absorption of a photon and is usually referred to as a direct transition. Process B represents the transfer of an electron from the same initial state near the valence band maximum to a state near the conduction band minimum with a different wave vector. In this process the absorption of an optical photon must be accompanied by the creation or annihilation of a lattice phonon. This process is referred to as an indirect transition and the resulting excited state is termed an indirect exciton.

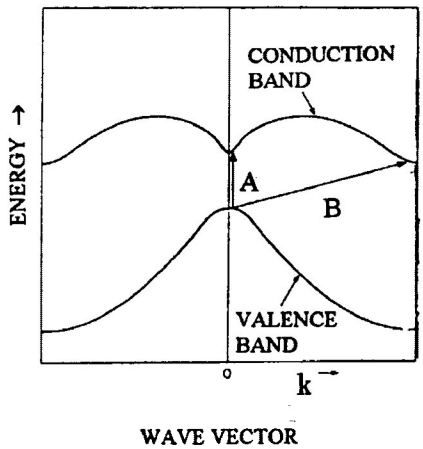

Figure 2.1: Schematic representation of a simple band structure, illustrating both direct (process A) and indirect (process B) electronic transitions.

Consider a simple model in which the band energies for isotropic, parabolic, and

non-degenerate conduction and valence bands in the vicinity of $\vec{k} = 0$ are given by

$$E_c(\vec{k}) = E_c(0) + \frac{\hbar^2 k^2}{2m_e^*} \tag{2.1}$$

and

$$E_v(\vec{k}) = E_v(0) - \frac{\hbar^2 k^2}{2m_h^*} \tag{2.2}$$

respectively. This is an idealized model, but when it does apply, the electron and hole behave dynamically like particles of mass m_e^* and m_h^* and charges $-|e|$ and $+|e|$, respectively [14]. Their total kinetic energy is given by

$$\frac{\vec{p}_e^{\,2}}{2m_e^*} + \frac{\vec{p}_h^{\,2}}{2m_h^*} \tag{2.3}$$

where $\vec{p}_e$ and $\vec{p}_h$ are the electron and hole momenta. Hence, the effective Hamiltonian for the two particles when interacting in a medium of dielectric constant, ε, is given by

$$H_{eff} = \frac{-\hbar^2 \nabla_e^2}{2m_e^*} - \frac{\hbar^2 \nabla_h^2}{2m_h^*} - \frac{e^2}{\varepsilon\,|\vec{r}_e - \vec{r}_h|} \tag{2.4}$$

where $\hbar$ is Planck's constant divided by 2π and $\vec{r}_e$ and $\vec{r}_h$ are the coordinates of the electron and hole.

The Schrödinger equation for the excited electron-hole pair is then given by

$$\left(\frac{-\hbar^2 \nabla_e^2}{2m_e^*} - \frac{\hbar^2 \nabla_h^2}{2m_h^*} - \frac{e^2}{\varepsilon\,|\vec{r}_e - \vec{r}_h|}\right) \psi_\alpha(\vec{r}_e, \vec{r}_h) = E_\alpha \psi_\alpha(\vec{r}_e, \vec{r}_h) \tag{2.5}$$

where the index α represents a complete set of quantum numbers. This equation separates when center-of-mass and relative coordinates are used. These coordinates are defined by

$$\vec{R} = (m_e^* \vec{r}_e + m_h^* \vec{r}_h)/(m_e^* + m_h^*) \tag{2.6}$$

and

$$\vec{r} = \vec{r}_e - \vec{r}_p. \tag{2.7}$$

The solutions of Eq. 2.5 are of the form

$$\psi_\alpha = F_\beta(\vec{r}) G_\gamma(\vec{R}). \tag{2.8}$$

Substituting Eqs. 2.6, 2.7 and 2.8 into Eq. 2.5, the quantities F and G are found to satisfy

$$\left(\frac{-\hbar^2}{2\mu}\nabla^2 - \frac{e^2}{\varepsilon r}\right) F_\beta = (E_\alpha - \epsilon_\gamma) F_\beta \tag{2.9}$$

and

$$\left(\frac{-\hbar^2}{2M^*}\nabla^2_{\mathbf{R}}\right) G_\gamma = \epsilon_\gamma G_\gamma. \tag{2.10}$$

Equations 2.9 and 2.10 have been expressed in terms of the reduced mass μ and the effective mass M^* of the exciton, respectively. These quantities are defined as follows:

$$\frac{1}{\mu} = \frac{1}{m_e^*} + \frac{1}{m_h^*} \tag{2.11}$$

and

$$M^* = m_e^* + m_h^*. \tag{2.12}$$

From examination of the form of Eq. 2.9, it is clear that the quantity in parentheses on the right-hand side of the expression is equal to the usual hydrogenic eigenvalues. Hence, it can be shown that

$$E_\alpha - \epsilon_\gamma = -\mu e^4/2\hbar^2\varepsilon^2 n^2 \tag{2.13}$$

where n is the principal quantum number. The remaining quantum numbers (l, m_l, m_s), which along with n are collectively called β, will not be considered here.

It is seen from Eq. 2.10 that ϵ_γ is the spectrum of eigenvalues for a free particle of mass M^*. This equation can also be solved to give the center-of-mass wave function

$$G_\gamma = A\exp(i\vec{\mathbf{K}}\cdot\vec{\mathbf{R}}) \tag{2.14}$$

where A is a constant. Hence, the allowed eigenvalues for the kinetic energy of the combined system are

$$\epsilon_\gamma = \hbar^2\vec{\mathbf{K}}^2/2M^*. \tag{2.15}$$

The exciton total wave vector $\vec{\mathbf{K}}$ is thus seen to suffice as a set of quantum numbers, γ. It is clear then, that the total energy of the exciton consists of both internal and kinetic parts:

$$E_n(\vec{\mathbf{K}}) = E_g - \frac{\mu e^4}{2\hbar^2\varepsilon^2 n^2} + \frac{\hbar^2\vec{\mathbf{K}}^2}{2M^*}. \tag{2.16}$$

The energy E_g in Eq. 2.16 is the band gap energy, $E_c(0) - E_v(0)$. It is the energy required to create one electron-hole pair of zero kinetic energy ($\vec{\mathbf{K}} = \mathbf{0}$) which is not bound ($n = \infty$). This merely sets the zero energy point.

In a typical semiconductor the second term in Eq. 2.16 (which we will denote as the exciton binding energy, E_x) is much smaller for a given n, than the usual Rydberg term

in atomic hydrogen. The binding energy, E_x, is related to the energy of the corresponding state of a hydrogen atom by

$$E_x = \frac{\mu}{m_e \varepsilon^2} E_n^H \tag{2.17}$$

where m_e is the free-electron mass and E_n^H is the energy of the hydrogen atom. For CdTe with an electron effective mass of $m_e^* = 0.096 m_e$ [16], light and heavy hole effective masses of $m_{lh}^* = 0.12 m_e$ [17] and $m_{hh}^* = 1.09 m_e$ [18], and a dielectric constant given by $\varepsilon = 9.0$ [16], we find the binding energy for the ground state exciton to be approximately 11.2 meV (taking $E_1^H = 13.6$ eV).

Hence, from examination of Eq. 2.16 we see that there exist a series of hydrogen-like energy levels. These excitonic levels are conventionally shown as existing below the conduction band as in Fig. 2.2. These levels become closer together for higher energies and finally merge into a continuum. The continuum is taken as the bottom of the conduction band, where the electron is free.

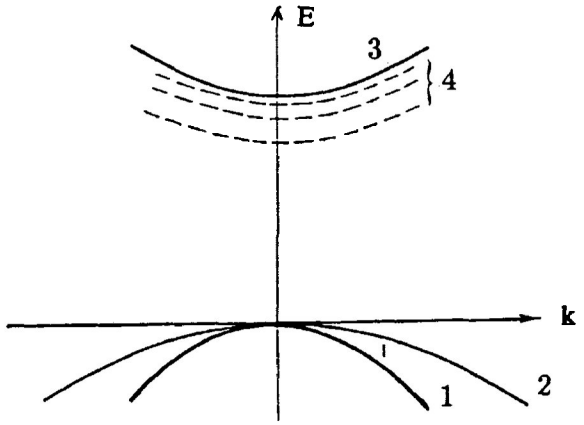

Figure 2.2: Exciton levels for direct transitions. (1) Light-hole valence band, (2) Heavy-hole valence band (3) Conduction band, (4) Exciton energy levels.

The spatial extent of the Wannier exciton state in the simple model considered here is given by the modified Bohr radius of the state. This is expressed as

$$\langle r \rangle_n = n^2 a_o \tag{2.18}$$

where

$$a_o = \frac{\hbar^2 \varepsilon}{\mu e^2} = \frac{m_e}{\mu} \varepsilon a_o^H, \tag{2.19}$$

and a_o^H, the Bohr orbit radius for the hydrogen atom is taken as 0.53 Å. Using CdTe as an example again, we find the radius of the first Bohr orbit of its exciton to be approximately $\langle r \rangle_1 = 71$ Å. This is an extremely large radius and the corresponding eigenstates extend over thousands of unit cells.

Free excitons quickly bind to different types of defects in the crystal. These include neutral and ionized impurities, vacancies, and surface structures. In general, exciton states are only observed in relatively pure semiconducting crystals. This occurs for a number of reasons. First, the electron-hole interaction is strongly shielded by the presence of other free carriers in the system. However, if only the free-carrier effects were important, one might expect to observe discrete exciton absorption in heavily doped but compensated materials. This is in fact, not the case. In addition to the free-carrier effects, the presence of a high concentration of impurity atoms results in a broadening of the exciton absorption lines such that above a certain impurity concentration the discrete spectra are wiped out.

We mentioned earlier that for a Wannier exciton, the electron and hole interact via a screened Coulomb interaction. The question as to what dielectric constant should be used in this interaction term arises? This can be determined from an estimate of the angular frequency of the exciton as found by equating the angular momentum to Planck's constant. Thus,

$$\omega = \left(\frac{\text{angular momentum}}{\text{mass} \times \text{radius}^2} \right) = \frac{\hbar}{\mu a_o^2}. \tag{2.20}$$

If $\omega < \omega_o$, where ω_o is an optical mode vibrational frequency, the lattice can follow the motion of the pair; it will polarize, and the low-frequency lattice dielectric constant will be appropriate to the Coulomb interaction. We may invert this whole argument and assert that the high-frequency lattice constant will be appropriate if the exciton radius is small enough, i.e. if $a_o < (\hbar/\mu\omega_o)^{\frac{1}{2}}$. Hence, in the case of CdTe with $a_o = 71$ Å, $\omega_{LO} = 5.15 \times 10^{12}$ Hz and $\omega_{TO} = 4.20 \times 10^{12}$ Hz [12], we find that $(\hbar/\mu\omega_o)^{\frac{1}{2}} = 184$ Å and 204 Å respectively and we are able to use the high-frequency lattice constant for the Coulomb interaction term.

It should be noted that these are rather simplified calculations since a zinc-blende cubic semiconductor like CdTe has degenerate valence bands which means that two types of holes,[3] have to be included in the dynamical excitonic problem. This has been found to result in several consequences as noted in Ref. [19]: existence of "heavy" and "light" excitons, anisotropy of the exciton dispersion, non-parabolic dispersion of excitons (even though the

[3]For $\vec{k} = 0$ in CdTe the Γ_8 level splits into two bands, each of the bands having different curvatures and consequently different effective masses for holes (i.e. light and heavy).

valence and conduction bands are parabolic) and non-hydrogenic excitonic energy levels.

2.3 Radiative Recombination

2.3.1 Intrinsic Recombination Processes

In photoluminescence measurements the sample is normally excited with a laser having $h\nu > E_g$. This creates electron-hole (e-h) pairs which recombine in several ways, some of which are radiative and emit photons which can be detected. The photon energy of the emitted light depends on the recombination process, illustrated in Fig. 2.3, where five of the most commonly observed PL transitions are shown [20].

Band-to-band transitions

The simplest recombination mechanism in an intrinsic semiconductor that results in photon emission corresponds to an electron in the conduction band recombining with a hole in the valence band. This transition, referred to as band-to-band recombination, is illustrated in Fig. 2.3 (a).

At low temperatures and excitation densities, mobile carriers can combine to form free excitons which may then become additionally bound to impurities and other defects so that the luminescence spectrum is dominated by recombination from these states rather than by band-to-band recombination. While at high temperatures ($k_BT > E'$; where E' is an energy characteristic of the binding of the carriers) thermal dissociation again results in a domination by band-to-band recombination. In the case of indirect gap semiconductors (see Fig. 2.1) this process is complicated by the fact that phonon assistance is required for momentum conservation. This requirement reduces the overall probability for indirect transitions. Generally, this probability is so low that radiative recombination of free carriers cannot be conveniently studied in indirect gap materials. However, at low temperatures and high illumination intensities, the carriers can condense into an electron-hole liquid drops from which enhanced recombination of all types can proceed.

Free exciton transitions

At low temperatures and relatively low excitation densities in sufficiently pure materials, the excess electrons and holes predominately form excitons which subsequently

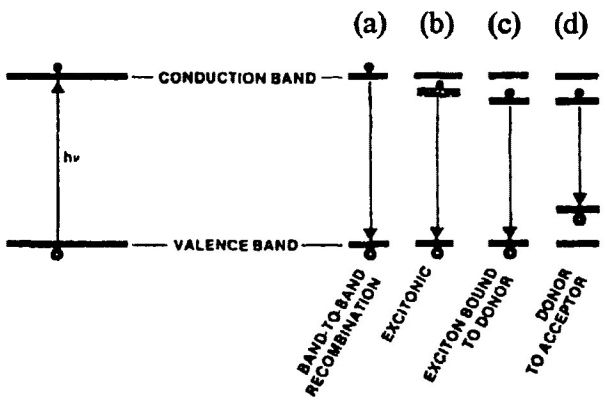

Figure 2.3: Common transitions observed with photoluminescence. Excitation can occur via absorption of a photon as shown on the extreme left. Radiative recombination can occur by any of the processes illustrated on the right-hand side of the figure.

decay via the free-exciton recombination mechanism illustrated in Fig. 2.3 (b). The free exciton (FE) represents the lowest energy intrinsic excitation of such a system. Once formed, the FE is capable of moving through the crystal. However, since it is a bound e-h pair, both the electron and hole move together resulting in no photoconductivity. The energy of a photon created by the recombination of this correlated state was given previously in Eq. 2.16. In indirect-gap materials the decay process must also be accompanied by the emission of a momentum conserving phonon. The energy of an emitted photon in the indirect gap case is thus given by

$$h\nu = E_g - E_x - \hbar\omega \tag{2.21}$$

where $\hbar\omega$ is the energy of the required phonon and E_x is the exciton binding energy as given in Eq. 2.17. A characteristic feature of the spectra of indirect gap materials is that a set of exciton recombination replica's appear due to the emission of different phonons.

Excitonic molecules

With increasing density, the FE's interact attractively and may form new bound states. Possibilities include a four particle complex analogous to a positronium molecule, resulting from the binding of the two free excitons, or an electron-hole "liquid" state, corresponding to the condensation of FE's. In the electron-hole "droplet" the condensate behaves

like a liquid metal and is composed of a neutral two component plasma of electrons and holes whose average energy is lower than that of the FE. The formation of this liquid can be viewed as a phase transition of the FE gas analogous to ordinary gas-liquid transformations.

2.3.2 Extrinsic Recombination Processes

The intrinsic recombination processes discussed above are seldom the dominant processes at low temperatures and low excitation densities. The presence of impurities in semiconductors is unavoidable and has a profound influence on the radiative recombination spectra even when impurity concentrations are low ($< 10^{14}\text{cm}^{-3}$). The variety of these extrinsic processes is immense, however, an understanding of the basic transitions involved is helpful in determining the nature of impurities in semiconductors as well as the efficiency of radiative recombination rates.

Free to bound transitions

Consider the presence of a single type of impurity (e.g. donor or acceptor) in an otherwise homogenous crystal lattice. For temperatures $T > 0$, the impurity is partially occupied so that some impurity centers are neutral while others are ionized. Two types of radiative transitions can occur when electrons and holes are excited is such a semiconductor. If the impurity is a donor then these transitions would be i) an electron to ionized donor transition ($e - D^+$) and ii) a hole to neutral donor transition ($D - h$) (see Fig. 2.3(c)). Since the energy binding a carrier to a donor or acceptor is generally in the meV range, the ($e - D^+$) transitions occur in the far infrared spectral range. Thus, since small energies are involved, phonon emission offers very effective competition and the radiative efficiency is quite low. Transitions of the ($D - h$) type occur close to the fundamental band gap energy and are usually several kT wide. Examining the spectral shape of such transitions can yield information about free-carrier distributions and impurity binding energies. Similar transitions are also possible when only acceptor impurities are present, i.e. ($e - A$) and ($A^+ - h$).

Donor-acceptor pair transitions

When a semiconductor has both donor and acceptor impurities, a radiative transition involving an electron bound to a donor and a hole bound to an acceptor becomes

possible. This process, illustrated in Fig. 2.3 (d) is referred to as a donor-acceptor pair (DAP) transition. The radiative probability for such transitions depends on the overlap of the wave functions of the electron at the donor and the hole at the acceptor and is quite small. At temperatures $k_BT \ll E_i$ (ionization energy of the impurities), the carriers cannot escape once they are captured at these impurities and DAP transitions become one of the dominant radiative processes. The impurities are neutral in the initial state of the DAP transition and ionized in the final state. The coulombic interaction between these ionized impurities lowers the energy of the final state so that energy of the emitted photon is increased by this amount.

Assuming a simple coulomb interaction between ionized impurities, the photon energy is given by

$$h\nu(r) = E_g - (E_A + E_D) + e^2/\varepsilon r \tag{2.22}$$

where E_A (E_D) is the acceptor (donor) ionization energy, E_g is the band gap energy, ε is the static dielectric constant, e is the electronic charge and r is the distance between donors and acceptor lattice atoms. [4] For substitutional impurities (located on lattice sites), r changes discretely and gives rise to a multitude of closely spaced, sharp lines. Different energy spacings occur depending on whether the two impurities are on similar or dissimilar lattice sites. The intensity of various lines is a function of the number of available lattice sites for a given pair separation r. There exist two limits of interest:

- If we assume that a free carrier cannot bind to an ionized DAP for donor-acceptor separation less than the normal Bohr radius of the isolated bound carrier, then the intensity of the DAP lines cutoff abruptly for r less than some critical value, r_c.
- For large r the relative increase in r from one shell to the next is so small that the lines merge to form a relatively broad band (both sharp lines due to close pairs and a broad band due to distant pairs have been observed in GaP [21]).

From such spectra one can deduce $(E_A + E_D)$ and whether or not donors and acceptors occupy similar or opposite lattice sites. As well, one can estimate E_A or E_D from the series cutoff at r_c.

[4] We note that $h\nu$ above may be larger that E_g for small values of $E_A + E_D$. Such photons are usually reabsorbed before escaping the sample.

The overlap of the wave functions of an electron at a donor and a hole at an acceptor depends on their separation r. Thus, the radiative transition probability decreases with increasing r (decreasing photon energy). However, the number of possible pairings decreases as r decreases. Consequently, the emission intensity must go through a maximum as the separation distance r is varied. With increasing excitation intensity the DAP spectrum is expected to shift to higher energy as the low energy (large r) states are saturated. This has been shown by Zacks *et al.* [22]. A multitude of sharp lines with increasing separation energy and a broad band at lower energies with the two properties described above form the characteristic signature of DAP transitions.

Bound exciton recombination

Under certain circumstances, the binding energy of an exciton is increased by the presence of a point defect like a neutral or ionized impurity. Energy is the fundamental criterion that determines whether or not an exciton can be trapped at an impurity. If the total energy of the system is reduced (corresponding to an increase in the binding energy of the exciton) when the exciton is in the vicinity of an impurity, then it is energetically favorable for the exciton to remain near the defect. The exciton then becomes "bound" to the impurity and hence, is referred to as a bound exciton (BE). Obviously if the energy of the system is increased when the exciton is near the defect, the exciton will choose to remain free.

An exciton, X, bound to an ionized donor, D^+, forms a complex consisting of a donor ion, an electron, and a hole. Such a construction is commonly denoted as (D^+, X) in the literature. In this molecule, the electron bound to the donor still travels in a wide orbit about the donor. The associated hole which moves in the electrostatic field of the "fixed" dipole, determined by the instantaneous position of the electron, also travels about this donor. The companion complex of a (D^+, X) is an exciton bound to an ionized acceptor (A^-, X). Other complexes of interest include an exciton bound to a neutral donor (D^o, X), consisting of the donor ion, two electrons and a hole, and an exciton-neutral acceptor complex (A^o, X), consisting of the acceptor ion, two holes and an electron.

The theoretical treatment of these multiparticle states is obviously very difficult, but they have nonetheless attracted much attention because of their great importance in recombination and luminescence phenomena [23]. The localization of the electron and the

hole in the vicinity of the same impurity leads to a large overlap of their wave functions, and therefore to a large BE oscillator strength[5] and recombination probability [24]. In addition, impurities typically have a large capture cross section for excitons making BE recombination an effective decay channel [25].

At low temperatures, near band gap luminescence spectra of many semiconductors show strong sharp lines due to the recombination of BE's. The photon energy of such lines is given by

$$h\nu = E_g - E_x - E_b - n\hbar\omega \tag{2.23}$$

where E_b is the binding energy of the exciton to the donor or acceptor. As evident from the presence of the last term in the above expression, bound exciton decay may proceed with or without the emission of n phonons, (where $n = 0, 1, 2, 3, ...$). The ratio of the no-phonon ($n = 0$) assisted BE line to the phonon assisted ($n > 0$) BE line in a given material increases with increasing exciton-to-impurity binding energy E_b [26]. This observation may be understood by noting that as E_b increases the BE has a larger fraction of its wavefunction at $\vec{k} = \mathbf{0}$ and hence the no-phonon component of the transition is stronger. Bound exciton transitions are prominent in low temperature PL spectra since their line widths are very narrow[6]. Hence, the spectral intensity of even a small population of these complexes can be quite large.

The existence of charged impurity-exciton complexes appears to depend critically upon the ratio of the effective masses for the electron and hole and upon details of band structure. Excitons can always bind to neutral donors or acceptors with some small localization energy, but not to ionized donors or acceptors unless $\sigma = m_e^*/m_h^*$ is appropriately much less than or much greater than one, respectively [27]. This relationship predicts that excitons cannot bind to both ionized donors and ionized acceptors in a single semiconductor. No deviations from this relationship have been reported.

At high excitation densities the donors and acceptors bind more than one exciton and additional satellite lines are seen in the spectrum associated with the cascade decay of multi-bound excitonic complexes. A detailed review of these complexes is given by Thewalt in Ref. [28].

[5]The oscillator strength is proportional to R^3; where R is the radial extent of the BE wavefunction. Since the BE's are usually weakly bound to impurity sites, R is large and hence the oscillator strength is large.

[6]The FWHM for BE transitions are typically $\leq kT/2$ and resemble slightly broadened delta functions, i.e. at $T = 11.5K$ we expect a line width of approximately 0.5meV.

2.4 Application to Material Characterization

2.4.1 Impurity identification

Photoluminescence is a non-destructive, highly sensitive technique for the simultaneous determination of many types of impurities (assuming they involve radiative transitions) in semiconductors. It is particularly well suited to the detection of shallow level impurities but can also be used to detect certain deep level impurities (as long as radiative transitions dominate). Examples of interest include the use of this method to determine the presence of Cu, Ag, Li, and Na acceptors and In and Cl donors in CdTe bulk and thin film materials [29, 30, 31, 32, 33]. The sharp luminescence lines obtained at low temperatures in these studies yield well defined energy assignments. These levels provide direct information about the chemical nature of the impurities associated with them. It has been estimated that the extreme sensitivity of the luminescence technique allows one to detect the presence of certain impurities down to concentrations of 10^{10} atoms/cm^{-3} (or one part in 10^{13}) [34].

Exciton binding to neutral donors and acceptors has been observed in many systems and found in some [35], to exhibit systematic trends which obey Haynes' rule [36]. Essentially, this rule states that the ratio of excitonic binding energy, E_b, to the ionization energy of the donor or acceptor to which the exciton is bound, measured for a variety of defects in different crystals, is essentially the same in all cases. It has been noted that for acceptor states, $E_b/E_A = 0.1$ and for donor states, $E_b/E_D = 0.2$ [37, 38]. While this simple proportionality has been shown to fail for selected III-V compounds, it still provides a very useful aid in the determination of recombination centers.

2.4.2 Defect identification

As mentioned earlier, excitons may be localized at neutral impurity or ionized crystal defects (i.e. native point or extended defects, substitutional or interstitial impurity atoms). Recombination of excitons localized at such defects yield emission spectra which reflect, in great detail, the structural imperfections present within the crystalline semiconductor. A representative collection of studies using the PL method to investigate such imperfections in CdTe are found in Refs. [39, 40, 41, 42]. In the work of Seto *et al.* [39] PL studies (before and after annealing) were used to determine that a prominent emission line, commonly observed in p-type CdTe crystals, was the result of the recombination of

excitons bound to Cd-vacancy/donor complexes. Amirtharaj *et al.* [42] studied the PL signal of In-doped CdTe films before and after several commonly used chemical treatments had been applied. Based on this study they were able to ascertain that the conventional surface preparation (etching) techniques applied to the films resulted in perturbations in the physical properties of the samples. Specifically, they found that the chemical treatment introduced a Cd-vacancy defect into the near surface region of the material.

2.4.3 Band gap and lattice parameters

The PL technique has become increasing useful in determining fundamental lattice and band gap parameters in ternary and quaternary compounds [43]. Many photoluminescence studies of these materials have recently been undertaken. In particular, Böhrer *et al.* [9] recently determined the dependence of the band gap energy and alignment type on Al concentration in $In_{1-x-y}Ga_xAl_yAs$ lattice matched to InP using low temperature PL measurements. The ability to deduce compositional information using this method is particularly useful when dealing with quaternary alloys, since x-ray diffraction measurements alone cannot quantify the composition of such films. In another study, Olsthoorn *et al.* investigated alloy clustering and carrier localization in $Al_{0.48}In_{0.52}As$ films by analyzing their PL properties as a function of temperature and excitation density [44]. In this work the authors note that line widths of PL peaks in alloys are generally determined by the presence of ionized impurities and by alloy fluctuations. The former depends on excitation density because an increase in this density increases the number of ionized impurities. In contrast, the latter broadening is independent of the excitation density. Using this criteria and the observed dependence of the PL line width on the excitation density, Olsthoorn *et al.* concluded that significant alloy fluctuations and clustering were present within the films.

2.4.4 Impurity concentration

As noted above, impurity identification using the PL technique is very precise due to the extremely high energy resolution associated with the method. Impurity concentration determination, on the other hand, is much more difficult. It is not easy to correlate the spectral intensity of a given PL signal to the concentration of impurities causing it. This is due to differential non-radiative effects associated with deep level bulk or surface recombination centers. Since the concentration of such recombination centers can vary unpredictably

from sample to sample (or location to location on a given sample), for a constant shallow level impurity concentration, it is not surprising that the PL signal can vary greatly.

A novel approach to this problem has been presented by several workers in an evaluation of thin films with different resistivities [26, 45, 46, 47]. It was found that samples with higher resistivities showed higher intensities of intrinsic peaks (i.e. FE peaks) relative to corresponding impurity peaks (i.e. BE peaks). By using this ratio technique it is possible to eliminate the effects of differential non-radiative transitions. It was estimated by Tajima *et al.* [46] that in silicon crystals, boron concentrations as low as 10^{11} cm^{-3} and phosphorus concentrations as low as 10^{12} cm^{-3} could be reliably detected using this method. Furthermore, both concentrations could be calculated from the same spectra once a power calibration curve had been established. This technique was only found to work well at low impurity concentrations where the intrinsic peaks were not obscured by impurity peaks.

Chapter 3

Theory of Raman Scattering From Crystals

3.1 Introduction

The measurement of the Raman spectrum of a crystal is one of the primary methods for obtaining information about its lattice vibration frequencies. The Raman effect in crystals has been known for a long time [48, 49] and exhaustive theoretical treatments of the process have been performed [50, 51, 52, 53, 54]. During the Raman event, incident light of angular frequency ω_o interacts with the crystal to create or destroy one or more lattice vibration quanta (phonons), and the energy $\hbar\omega$ gained or lost by the lattice is compensated by a decrease or increase in the frequency ω_s of the scattered light ($\omega_s = \omega_o \pm \omega$).

The lattice vibrations of the majority of crystals have a maximum wavenumber somewhere in the range from 100 to 1,000 cm^{-1}. The first-order Raman spectrum occupies a range of this extent on either side of the exciting frequency. The fraction of scattered light with lower frequency than that of the incident light is called the Stokes component, while the fraction of light with higher frequency is denoted the anti-Stokes component. Although both optic and acoustic phonons give rise to first-order Raman scattering, only lattice vibrations having certain types of symmetry result in Raman scattering. Such vibrations are deemed to be Raman-active. The phonon wavevector can assume any value lying in the Brillouin zone, the maximum value being of the order π/a, where a is the lattice constant. This maximum value is typically around 3×10^8 cm^{-1}. Incident light of wavelength $\lambda = 514.53$

nm ($\bar{\nu} = 19,435\ \mathrm{cm}^{-1}$), for example, has a wavevector[1] inside the crystal of the order of $2\times10^5\ \mathrm{cm}^{-1}$. This is very small in comparison with π/a and thus, the phonons of importance in the first-order Raman effect have wavelengths very long relative to the lattice constant. The smallness of the wavevector, $\vec{\mathrm{k}}$, of the first-order Raman-active phonons leads to a great simplification in the discussion of their properties.

The first-order Raman effect is a scattering process in which a single phonon is either created or destroyed. In the second-order Raman effect, two phonons participate in the scattering process. They may both be created (giving rise to a Stokes component in the scattered light), one may be created and the other destroyed (resulting in both Stokes and anti-Stokes components), or finally both may be destroyed (producing only an anti-Stokes component).

The emphasis of this chapter will be on providing a summarized general account of the nature and theory of the Raman effect in crystals as it is found in Ref. [50]. The Raman scattering process will be discussed, symmetry properties of crystals will be outlined and applications of the process to semiconductor characterization will be summarized.

3.2 Scattering Theory

As mentioned above, the Raman process involves the inelastic scattering of photons by a crystal. Photons of energy $\hbar\omega_o$, and direction specified by the momentum $\vec{\mathrm{k}}_o$, are incident on a crystal and scattered to give photons of energy $\hbar\omega_s$ and momentum $\vec{\mathrm{k}}_s$. The initial state of the crystal, i, has energy E_i, and the final state, f , an energy E_f. The probability of the scattering process is given by the golden rule of second-order perturbation theory [55] as:

$$w = \frac{2\pi}{\hbar}\rho(\omega_s)\left|H(\vec{\mathrm{k}}_o, i : \vec{\mathrm{k}}_s, f)\right|^2 \delta(\hbar\omega_o + E_i - \hbar\omega_s - E_f) \tag{3.1}$$

where $\rho(\omega_s)$ is the density of states of the photons, given by

$$\rho(\omega_s)d\omega_s d\Omega = \left(\frac{1}{2\pi c}\right)^3 \frac{\omega_s^2}{\hbar} d\omega_s d\Omega \tag{3.2}$$

where $d\Omega$ is an element of solid angle. The interaction between the photons and the crystal is specified by the Hamiltonian, H.

[1]Note that the wavevector, $\vec{\mathrm{k}} = 2\pi \times n \times \bar{\nu}$; where n is the refractive index of the material and $\bar{\nu}$ is the wavevector of the light.

When treated in its most general form, the interaction between electromagnetic radiation and crystalline matter is a very complicated problem. The situation is somewhat simplified in the Raman process, however, where the wavelengths of both the incident and scattered light are much greater than the size of the atoms with which they are interacting. Furthermore, the electric fields associated with the light nearly always give rise to Raman scattering. As a result, the interaction Hamiltonian may be written in terms of the polarizability, P, of the crystal such that

$$H = \sum_{\alpha\beta} P_{\alpha\beta}(\vec{\mathbf{k}}_o i : \vec{\mathbf{k}}_s f) E_\alpha(o) E_\beta(s) \tag{3.3}$$

where $\vec{\mathbf{E}}(o)$ and $\vec{\mathbf{E}}(s)$ are the electric fields associated with the incident and scattered light, and α and β denote the Cartesian coordinates. Before the result can be substituted into Eq. 3.1 it is necessary to rewrite the electric field terms as functions of the photon creation, $b^+(\vec{\mathbf{k}})$, and annihilation, $b(\vec{\mathbf{k}})$, operators (after Ref. [56])

$$\vec{\mathbf{E}}(o) = i(2\pi\hbar\omega_o)^{\frac{1}{2}} \vec{\varepsilon}(o)[b(\vec{\mathbf{k}}_o) - b^+(-\vec{\mathbf{k}}_o)] \tag{3.4}$$

where we have introduced the polarization vector for the photons, $\vec{\varepsilon}(o)$. The electric field varies in space with the wavevector of the photon, through an $\exp(i\vec{\mathbf{k}}_o \cdot \vec{\mathbf{R}})$ term.

The conventional expression for Raman scattering, as developed in Ref. [57], is stated in terms of the energy scattered for a particular incident electric field. The energy scattered is $\hbar\omega_s w$ and the number of quanta can be given in terms of the incident electric field by $\bar{n} = (\vec{\mathbf{E}}(o) \cdot \vec{\mathbf{E}}(o))/2\pi\hbar\omega_o$. Combining these results with Eqs. 3.2 and 3.3, allows one to express the intensity of the Raman scattering process from state i to state f of the crystal as

$$I d\Omega d\omega_f = \frac{\omega_f^4}{2\pi c^3} \sum_{\alpha\beta\gamma\delta} P_{\alpha\beta}(\vec{\mathbf{k}}_o i : \vec{\mathbf{k}}_s f) P^+_{\gamma\delta}(\vec{\mathbf{k}}_o i : \vec{\mathbf{k}}_s f) E_\alpha(o) E_\gamma(o) \varepsilon_\beta(s) \varepsilon_\delta(s) \delta(E_i + \hbar\omega_o - E_f - \hbar\omega_s) \tag{3.5}$$

The total Raman scattering intensity is then obtained by averaging over the initial and final states of the crystal and weighting them by the appropriate thermodynamic factors. This yields

$$I d\Omega d\omega_f = \frac{\omega_f^4}{2\pi C^2} \sum_{\alpha\beta\gamma\delta} E_\alpha(o) E_\gamma(o) \varepsilon_\beta(s) \varepsilon_\delta(s) I_{\alpha\beta\gamma\delta} \tag{3.6}$$

where

$$I_{\alpha\beta\gamma\delta} = \sum_{if} \rho_i P_{\alpha\beta}(\vec{\mathbf{k}}_o i : \vec{\mathbf{k}}_s f) P^+_{\gamma\delta}(\vec{\mathbf{k}}_o i : \vec{\mathbf{k}}_s f) \delta(E_i + \hbar\omega_o - E_f - \hbar\omega_s) \tag{3.7}$$

In the expression above, the thermodynamic probability is given by $\rho_i = \exp(-\beta E_i)/Z$, the inverse temperature, β, is given by $1/k_B T$ and the partition function [58] is represented by Z.

Upon rewriting the delta function in the above expression as an integral over time and introducing a polarizability operator, Eq. 3.7 becomes

$$I_{\alpha\beta\gamma\delta} = \frac{1}{2\pi}\int_{-\infty}^{\infty} \ll P_{\alpha\beta}(\vec{\mathbf{k}}_o\vec{\mathbf{k}}_s,t)P^{+}_{\gamma\delta}(\vec{\mathbf{k}}_o\vec{\mathbf{k}}_s,o) \gg \exp(i\omega t)dt \tag{3.8}$$

where the polarizability operators are written in the Heisenberg representation, ω denotes the frequency transfer,

$$\omega = \omega_o - \omega_s \tag{3.9}$$

and the brackets, $\ll \ldots \gg$, indicate the thermodynamic average.

3.3 Normal Modes of Vibration of Crystals

The displacements of atoms from their equilibrium positions in crystals are described by their normal modes of vibration. The theory of these normal modes has been extensively developed elsewhere [57, 59, 60, 61] and only the results will be reviewed in order to establish notation required for later considerations.

To begin, the potential energy of the crystal is expanded in a power series of the displacements of the ions from their equilibrium positions. Neglecting anharmonic terms, this series can be written as:

$$\phi = \phi_o + \frac{1}{2}\sum_{l_1 l_2}\sum_{k_1 k_2}\sum_{\alpha\beta}\phi_{\alpha\beta}\begin{pmatrix} l_1 & l_2 \\ k_1 & k_2 \end{pmatrix} U_\alpha \begin{pmatrix} l_1 \\ k_1 \end{pmatrix} U_\beta \begin{pmatrix} l_2 \\ k_2 \end{pmatrix} + \ldots \tag{3.10}$$

where ϕ_o is the potential energy of the static crystal, $\vec{\mathbf{U}}(\, lk)$ is the displacement of the kth type of atom in the lth unit cell, and $\phi_{\alpha\beta}\begin{pmatrix} l_1 & l_2 \\ k_1 & k_2 \end{pmatrix}$ is the appropriate second derivative of the potential which is minus the force on the atom $(l_1 k_1)$ in the α direction when the atom $(l_2 k_2)$ is displaced a unit amount in the β direction.

The equation of motion of the atom $(l_1 k_1)$ can be expressed as

$$M_{k_1}\ddot{U}_\alpha \begin{pmatrix} l_1 \\ k_1 \end{pmatrix} = -\sum_{\beta l_2 k_2}\phi_{\alpha\beta}\begin{pmatrix} l_1 & l_2 \\ k_1 & k_2 \end{pmatrix} U_\beta \begin{pmatrix} l_2 \\ k_2 \end{pmatrix} \tag{3.11}$$

where the mass of the atoms of type k_1 are given by M_{k_1}. This equation is simplified by introducing Bloch waves for the displacements so that

$$\vec{\mathbf{U}}(lk) = \left(\frac{1}{NM_k}\right)^{\frac{1}{2}} \sum_{\vec{\mathbf{q}}} \vec{\mathbf{U}}(k \mid \vec{\mathbf{q}}) \exp i(\vec{\mathbf{q}} \cdot \vec{\mathbf{R}}(lk) - \omega t) \tag{3.12}$$

where N is the number of unit cells in the crystal. Substituting Eq. 3.12 into Eq. 3.11 yields

$$\omega^2 U_\alpha(k \mid \vec{\mathbf{q}}) = \sum_{\beta k'} D_{\alpha\beta}(kk' \mid \vec{\mathbf{q}}) U_\beta(k' \mid \vec{\mathbf{q}}) \tag{3.13}$$

where the dynamical matrix, (after Born *et al.* [57]) is given by

$$D_{\alpha\beta}(kk' \mid \vec{\mathbf{q}}) = \left(\frac{1}{M_k M_{k'}}\right)^{\frac{1}{2}} \sum_l \phi_{\alpha\beta} \begin{pmatrix} o & l \\ k & k' \end{pmatrix} \exp i\vec{\mathbf{q}} \cdot \left(\vec{\mathbf{R}} \begin{pmatrix} l \\ k' \end{pmatrix} - \vec{\mathbf{R}} \begin{pmatrix} o \\ k \end{pmatrix}\right) \tag{3.14}$$

The normal modes of vibration are obtained by diagonalizing the dynamical matrix to give the eigenvalues $\omega^2(\vec{\mathbf{q}}j)$ and the eigenvectors $\mathbf{e}(k \mid \vec{\mathbf{q}}j)$ of the jth normal mode. The normalization condition for these eigenvalues is given by

$$\sum_k \mathbf{e}(k \mid \vec{\mathbf{q}}j) \cdot \mathbf{e}^+(k \mid \vec{\mathbf{q}}j') = \delta_{jj'} \tag{3.15}$$

It is useful, at this point, to introduce the phonon coordinates $A(\vec{\mathbf{q}}j)$ which are the sum of phonon creation and destruction operators

$$A(\vec{\mathbf{q}}j) = a(\vec{\mathbf{q}}j) + a^+(-\vec{\mathbf{q}}j) \tag{3.16}$$

When written in terms of these operators, the displacements of the atoms may be given by

$$\mathbf{U}(lk) = \sum_{\mathbf{q}j} \left(\frac{\hbar}{2\omega(\vec{\mathbf{q}}j)NM_k}\right)^{\frac{1}{2}} \mathbf{e}(k \mid \vec{\mathbf{q}}j) \exp[i\vec{\mathbf{q}} \cdot \vec{\mathbf{R}}(lk)] A(\vec{\mathbf{q}}j) \tag{3.17}$$

The formal development of phonon theory is completed by studying the time development of the operators $a(\vec{\mathbf{q}}j)$ and $a^+(\vec{\mathbf{q}}j)$. In the Heisenberg representation $A(\vec{\mathbf{q}}j, t)$ is given by

$$A(\vec{\mathbf{q}}j, t) = a(\vec{\mathbf{q}}j, o) \exp(i\omega(\vec{\mathbf{q}}j)t) + a^+(-\vec{\mathbf{q}}j, o) \exp(-i\omega(\vec{\mathbf{q}}j)t) \tag{3.18}$$

With the aid of Bose statistics [62], the thermodynamic expectation value of these operators may be expressed as:

$$\ll a(\vec{\mathbf{q}}j) a^+(\vec{\mathbf{q}}j) \gg = n(\vec{\mathbf{q}}j) + 1$$

$$\ll a^{+}(\vec{\mathbf{q}}j)a(\vec{\mathbf{q}}j) \gg = n(\vec{\mathbf{q}}j) \tag{3.19}$$

where the population factor is given by:

$$n(\vec{\mathbf{q}}j) = 1/\{\exp[\beta\hbar\omega(\vec{\mathbf{q}}j)] - 1\} \tag{3.20}$$

Although the above development is quite formal it does allow the frequencies of the normal modes of vibration to be obtained if the interatomic potential is known. The (Fourier-transformed) dynamical matrix, D, is a Hermitian square matrix of size three times the number of atoms in each unit cell, s. Thus, there are $3s$ different frequencies for each wavevector $\vec{\mathbf{q}}$. A complete description of the normal modes is a list of these frequencies and the associated eigenvectors for all wavevectors lying within the first Brillouin zone. It is usually necessary to make use of a model of the crystal before the phonon dispersion curves for a particular material may be calculated, as little theoretical progress has been made in making a-priori calculations.

3.4 One-Phonon and Two-Phonon Raman Processes

In Section 3.2, the Raman scattering intensity was deduced in terms of the polarizability of the crystal. In this section the polarizability will be expanded in terms of the normal mode coordinates, $A(\vec{\mathbf{q}}j)$, introduced in the previous section. In Raman scattering experiments in which the incident frequency is (i) much greater than the frequency transfer (i.e. $\omega_o \geq \omega$) and (ii) not close to any of the electronic excitation frequencies of the crystal, it may be assumed that the polarizability is symmetric in α and β and thus, may be expanded in a series as:

$$P_{\alpha\beta} = P^{o}_{\alpha\beta} + \sum_{\vec{\mathbf{q}}j} P_{\alpha\beta}\begin{pmatrix}\vec{\mathbf{q}}\\ j\end{pmatrix} A\begin{pmatrix}\vec{\mathbf{q}}\\ j\end{pmatrix} + \sum_{\vec{\mathbf{q}}_1\vec{\mathbf{q}}_2,j_1j_2} P_{\alpha\beta}\begin{pmatrix}\vec{\mathbf{q}}_1 & \vec{\mathbf{q}}_2\\ j_1 & j_2\end{pmatrix} A\begin{pmatrix}\vec{\mathbf{q}}_1\\ j_1\end{pmatrix} A\begin{pmatrix}\vec{\mathbf{q}}_2\\ j_2\end{pmatrix} + \ldots \tag{3.21}$$

In this expansion the coefficients are assumed to be independent of the frequency transfer, while conservation of momentum shows for the one-phonon term that

$$\vec{\mathbf{k}}_o - \vec{\mathbf{k}}_s = \vec{\mathbf{Q}} = \vec{\mathbf{q}} \tag{3.22}$$

where $\vec{\mathbf{Q}}$ is the momentum transfer, and for the two-phonon term

$$\vec{\mathbf{Q}} = \vec{\mathbf{q}}_1 + \vec{\mathbf{q}}_2 \tag{3.23}$$

The cross-section for the one phonon Raman scattering process may be obtained by substituting the Heisenberg representation for the phonon operators (given in Eq. 3.18) and their expectation values (given in 3.19), into Eq. 3.8 to give

$$I^I_{\alpha\beta\gamma\delta} = \sum_j P_{\alpha\beta}\begin{pmatrix}\vec{\mathbf{Q}}\\ j\end{pmatrix} P^+_{\gamma\delta}\begin{pmatrix}\vec{\mathbf{Q}}\\ j\end{pmatrix} [n(\vec{\mathbf{Q}}j)\delta(\omega+\omega(\vec{\mathbf{Q}}j))+(n(\vec{\mathbf{Q}}j)+1)\delta(\omega-\omega(\vec{\mathbf{Q}}j))] \quad (3.24)$$

A cursory examination of this expression shows that one-phonon Raman scattering occurs at the frequencies of the phonons whose wavevectors are equal to the wavevector transfer in the experiment. As mentioned earlier, the process in which the light quanta lose energy during scattering is referred to as Stokes scattering, while the complimentary process in which energy is gained by the light is denoted as anti-Stokes Raman.

As the wavelength of the exciting radiation in Raman experiments is much longer than the interatomic distances within the crystal, the available momentum transfers, $\vec{\mathbf{Q}}$, are much smaller ($< 10^{-3}$) than the momentum of many of the phonons. Hence, to a first approximation one can take $\left|\vec{\mathbf{Q}}\right| = 0$ in the Raman scattering process unless the frequencies $\omega(\vec{\mathbf{Q}}j)$ vary rapidly with wavevector for small wavevectors. As evident from examination of Eqs. 3.20 and 3.24, the intensity ratios of the Stokes to anti-Stokes distributions is given by $\exp(\beta\hbar\omega)$.

The scattering cross-section for the two-phonon Raman process has been calculated in a similar manner and is given in Ref. [50]. There are two types of second-order Raman scattering (as noted in Ref. [51] by Loudon) and they give rise to a line spectrum and a continuous spectrum, respectively. The second-order line spectrum is due to processes in which the incident light suffers two successive first-order Raman scatterings. Thus, it is essential that first-order Raman scattering be allowed for the two phonons individually, as the frequency shifts which occur in the second-order line spectrum are sums and differences of the shifts occurring in the first-order spectrum. It is not necessary for energy to be conserved in the intermediate state. However, the total wavevector in this state must be the same as in the initial state and this conservation law forces the wavevector of the first phonon to be small and leads to the line nature of the resulting Raman spectrum. Since the process depends on two successive scattering events which must both take place within the crystal volume, the scattering efficiency for the second-order line spectrum increases with the size of the crystal.

The second-order continuous spectrum is due to a scattering process in which the

light interacts with a pair of phonons in a single event. If attention is restricted to the case where two phonons are created, then there are no restrictions placed on the phonon wavevectors other than the requirement that their sum should balance the change in wavevector of the scattered photon. Subject to this condition, the phonon wavevectors can range in value over the entire Brillouin zone. Since the photon wavevectors are negligible compared to the Brillouin zone dimensions, wavevector conservation effectively requires that the wavevectors of the two phonons must be equal and opposite. The continuous frequency distribution displayed by the scattered photons is thus proportional to a weighted density of lattice states in which two phonons of equal and opposite wavevector are present. The weighting is due to the frequency and wavevector dependence of the interactions involved in the scattering process. The second-order continuous spectrum results from a single scattering event and the scattering efficiency is therefore independent of the crystal size, as in the first-order Raman effect. This fact leads to an experimental means for resolving the second-order line and continuous spectra in cases where the continuum has sharp features or where the lines involved are broad.

While it is possible to approach higher order (i.e. three-phonon, etc.) Raman scattering processes using the formalism outlined earlier in this section, the calculations associated with such problems are quite involved and proper interpretation of the results becomes increasingly difficult.

3.5 The Polarizability

In most Raman experiments the frequency of the incident light is much higher than any of the normal mode frequencies of the crystal. Hence, there is poor coupling of the light to the lattice and the polarizability arises in a large extent, from electronic distortions. The most important mechanism for Raman scattering was developed by Loudon [53] and is illustrated in Fig. 3.1. In the single phonon case, Fig. 3.1 (a), the incident photon creates a virtual electron-hole pair, e_1, which either creates or absorbs a phonon resulting in the virtual pair, e_2. This second pair then recombines and emits the scattered photon. The magnitude of the polarizability can be calculated using third order perturbation theory and has been found to be proportional to

$$\sum_{e_1 e_2} \frac{\langle i \mid H_I^{\alpha} \mid e_1 \rangle \langle e_1 \mid H_{II} \mid e_2 \rangle \left\langle e_2 \mid H_I^{\beta} \mid f \right\rangle}{(\omega_{e_1} - \omega_o)(\omega_{e_2} - \omega_s)} \tag{3.25}$$

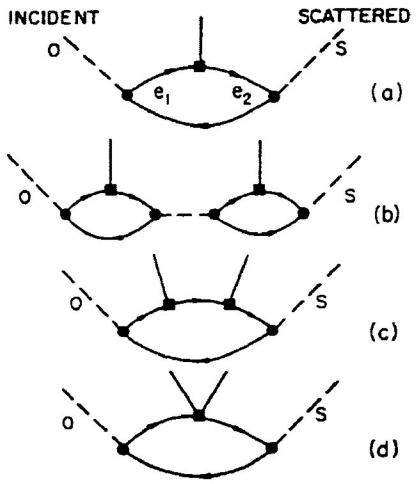

Figure 3.1: Schematic diagrams showing the Raman scattering process for one-phonon (a) and two-phonon (b-d) processes; - - - - = photon, ——— = phonon, – – = electron, – – = hole.

where H_I^α represents the coupling with the incident light polarized in the α direction, H_I^β the coupling with the scattered light in the β direction, and H_{II} the electron-phonon scattering by which state e_1 is scattered to state e_2 with the production of a Raman-active phonon.

Upon examination of this result it becomes apparent that the polarizability, as expressed in the expansion of Eq. 3.21, is independent of the frequency transfer ω only if $|\omega_{e_1} - \omega_o| \gg \omega$. If $\hbar\omega_o$ is close to one of the energies, $\hbar\omega_{e_1}$, then the polarizability is enhanced, resulting in what is commonly referred to as the resonant Raman effect. This effect is discussed in much detail in Refs. [63] and [64]. Also inferred from Eq. 3.25, is that the polarizability tensor will only be symmetric in α and β, if ω_o and ω_s may be interchanged without altering the result. This will be the case when ω_o and ω_s are both large relative to ω, and when their differences from ω_{e_1} and ω_{e_2} are also large.

Some of the possible two-phonon Raman scattering processes are shown in Figs. 3.1 (b-d). In Fig. 3.1 (b) the phonons are scattered by two successive single-phonon Raman events as found in Fig. 3.1 (a). In this transition, both phonons generated are Raman-active and their resultant spectrum will consist of lines at the frequencies of pairs of one-phonon active phonons. The processes illustrated in Figs. 3.1 (c) & (d), give rise to phonons with equal and opposite values of the wavevector, $\vec{q}$.

3.6 Symmetry Properties

3.6.1 Group Theory

In Sections 3.2 and 3.4, Raman scattering was described and translational symmetry was used to develop the momentum conservation equations, Eqs. 3.22 and 3.23. The point group symmetry of crystals, however, places further restrictions on the phonons of the scattering process. While the application of group theory to solid state physics has been extensively described elsewhere [65, 66, 67], its usefulness warrants a brief review.

Suppose the symmetry of a crystal is denoted by the group G, composed of both translational and rotational symmetry operations S. It is the object then to describe the effect of symmetry on a particular property of the crystal, represented by the functions ψ_i. The number of these functions, i, which are independent of one another will depend on the particular crystal property of interest. The effect of the symmetry element, S, on the functions ψ_i, is to transform them into one another as defined by

$$\psi_i = \sum_j S_{ij}\psi_j \tag{3.26}$$

The matrices S_{ij} form, what is referred to as, a representation of the group G, and the functions ψ_i, are designated as the basis vectors of that representation. It is possible to find linear combinations of these basis functions, such that the matrices S_{ij} are reduced to block diagonal form. These linear combinations then transform under the symmetry operators into a new limited set of functions. The simplified or reduced representation is then referred to as the irreducible representation. Since, the irreducible representation transforms under the symmetry operators in a unique manner it necessarily contains information about the symmetry of the property. The classification of a property into the irreducible representation determines the minimum number of different possible components necessary to properly describe the property and the way it transforms under the symmetry operators.

The symmetry characteristics of a particular property are calculated by first choosing a representation and then reducing that representation to see how many times each irreducible representation occurs in the description of the physical quantity. The reduction of the representation to its irreducible components is easily accomplished using what is referred to as the character of the representation. The character $\chi(S)$ of the representation of symmetry element S is the sum of the diagonal elements of the transformation matrix,

S_{ij}:

$$\chi(S) = \sum_i S_{ii} \tag{3.27}$$

For each symmetry element, group theory then states

$$\chi(S) = \sum_\lambda C_\lambda \chi^\lambda(S) \tag{3.28}$$

where C_λ is the number of times the λ irreducible representation is present in the original representation and $\chi^\lambda(S)$ is the character of symmetry element, S, in the irreducible representation. Hence, for each S, Eq. 3.28 generates a set of simultaneous equations for the C_λ and as such, enables the representation to be reduced. It is possible to separate the large number of translational elements associated with the crystal from the rotational components by use of the Bloch waves and a description of a crystal property in terms of a wavevector, $\vec{\mathbf{q}}$, restricted to one Brillouin zone. Once this is accomplished, the rotational part of the symmetry may be further divided into two parts; one which changes $\vec{\mathbf{q}}$ into a new vector $\vec{\mathbf{q}}'$, and the other which transforms $\vec{\mathbf{q}}$ in itself (or changes only its sign)[2]. The latter operations form a group which is called the group of the wavevector $\vec{\mathbf{q}}$ or $\vec{\mathbf{q}}$-group [54, 68] and produces additional symmetry requirements. ψ_i transforms under the operations of the group of $\vec{\mathbf{q}}$ by an irreducible representation of this group which is called the small representation of the space group. In symmorphic space groups (those lacking glide planes [3] and screw axes [4]) the little group is one of the crystal point groups whose irreducible representations are well known.

When this formalism is applied to the determination of selection rules is usefulness becomes clearly apparent. For example, consider the product of two functions $\phi_j \psi_i$. If both of these functions are reduced to their irreducible representations, then the product may be expressed as a sum of the products of their irreducible representations. This new representation will have characters which are the product of the individual characters of ϕ_j and ψ_i, and may also be reduced to the irreducible representations. This product representation is very useful in calculating matrix elements of the form:

[2]The transformation $\vec{\mathbf{q}} \rightarrow -\vec{\mathbf{q}}$ does not change the geometry of the system; for scattering problems it is equivalent to a reversal of the optical path of the incident and scattered light.

[3]The glide plane is defined as the composite operation of a reflection in a plane followed by a displacement, v_r, parallel to the plane; where v_r is half the lattice vector.

[4]The screw axis is a rotation around an n-fold axis followed by a displacement, v_r, along the axis.

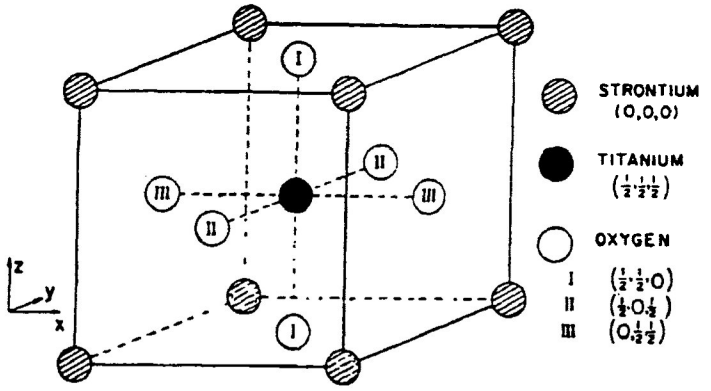

Figure 3.2: The crystal structure of strontium titanate.

$$M_{ij} = \langle \psi_i \, | o | \, \psi_j \rangle \tag{3.29}$$

Then, M_{ij} will only yield a non-zero result if the product representation of $\psi_i \psi_j$ contains at least one irreducible representation which is present in the reduction of the operator, o.

3.6.2 The Raman Tensor

The Raman scattering process is specified by the tensor $I_{\alpha\beta\gamma\delta}$ as given in Eqs. 3.7 and 3.8. Within the adiabatic approximation (i.e. $|\omega_o - \omega_e| \gg \omega$), presented on p. 35, it is symmetric for the interchange of α and β, γ and δ, and $\alpha\beta$ and $\gamma\delta$. If the wavevector, $\vec{\mathbf{q}}$, is neglected initially then the Raman tensor has the full point group symmetry of the crystal and is a fourth rank tensor [5].

To illustrate the usefulness of the techniques outlined in the previous section, they will be applied to the strontium titanate crystal as considered by Cowley in Ref. [69]. The structure of strontium titanate is cubic perovskite and the point group symmetry is classified as $m3m$, according to the notation of the *international system*[6]. Tables, like those found in Ref. [67] facilitate converting between this system and the other commonly used formalism, the *Schönflies system*. The ions of strontium titanate are situated on five interpenetrating

[5]The rank of a tensor is defined as the order of the highest order square tensor with a nonvanishing determinant contained in the tensor.

[6]It should be noted that the *international system*, does not use the improper rotation symmetry element found in the *Schönflies system*. Instead, the system uses another symmetry element, the rotary-inversion element, which is a rotation followed by an inversion, $\bar{X}$ (or $\bar{n}$), where $\bar{X}$ (or $\bar{n}$) is the main rotation axis.

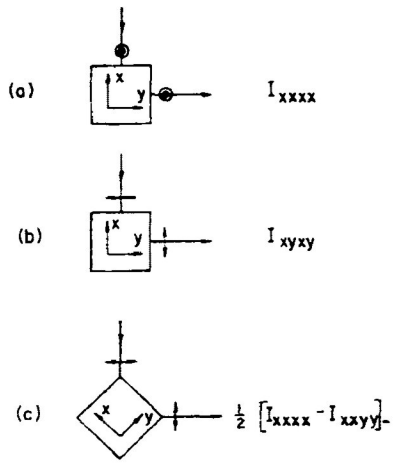

Figure 3.3: Schematic diagram showing the way in which it is possible to measure the three components of the Raman tensor in cubic crystals. The incident and scattered light are polarized either (a) perpendicular to or (b)/(c) parallel to the scattering plane.

simple cubic lattices as shown and labelled in Fig. 3.2. The symmetry of the Raman tensor for permutation of the indices permits a maximum of 21 independent coefficients of the form; I_{xxxx}, I_{xyxy}, etc. These 21 coefficients form the basis of a representation of the above point group which may be reduced to give the representations

$$3\Gamma_1 + 3\Gamma_{12} + \Gamma'_{25} + 3\Gamma'_{15} \tag{3.30}$$

using the notation of Koster [68]. Since the Raman scattering is invariant under the symmetry operations of the crystal, the measurable quantities will transform like the identity representation, Γ_1. From this result, it is clear that there exist three independent Raman scattering tensors in the cubic crystals, namely I_{xxxx}, I_{xxyy} and I_{xyxy}. A complete measurement of the Raman scattering is thus a measurement of each of these independent tensors as a function of frequency. Three different experimental geometries, like those illustrated in Fig. 3.3, would be required to measure each of these components.

3.6.3 Normal Modes of Vibration

The application of group theory to the classification of the normal modes of vibration of crystals is a very useful technique. Examples of the methods employed can be found in Refs. [70] and [71]. In such cases, the Fourier transform of the atomic displacements in the crystal, given previously in Eq. 3.12, is chosen to give a representation of the space group.

This representation is then reduced using the small group symmetry of the wavevector, $\vec{\mathbf{q}}$, to give the transformation properties of the normal modes for each wavevector.

To gain insight into the use of this approach, the technique will be applied to the normal modes of the perovskite lattice (after Cowley [69]), introduced earlier. As evident from Fig. 3.2, there are five atoms in each unit cell of the crystal structure and hence, there are 15 possible components of the displacement vector $\vec{\mathbf{U}}(k \mid \vec{\mathbf{q}})$. Using the techniques outlined in Refs. [70] and [71], the characters of the different symmetry operators may be obtained.

When $\vec{\mathbf{q}} = 0$ and hence $\zeta = (0,0,0)$, the symmetry is $m3m$ and the irreducible representations are:

$$4\Gamma_{15} + \Gamma_{25} \tag{3.31}$$

The result is, however, incorrect because the effect of the macroscopic electric field[7] has been neglected. The electric field splits the degeneracy for some of the normal modes because the boundary conditions for the longitudinal and transverse modes differ (see Ref. [57]). The degeneracies will be lifted for those normal modes which transform like an ordinary vector. Since an ordinary vector transforms like Γ_{15}, the degeneracies associated with three of the four irreducible representations Γ_{15} are split. The fourth irreducible representation corresponds to a uniform translation of the whole crystal. There are, therefore, three acoustic modes, $\omega = 0$, a triply degenerate set of normal modes, Γ_{25}, and three longitudinal and doubly degenerate transverse optical modes.

When $\vec{\mathbf{q}}$ is along the [001] direction, represented by $\zeta = (0,0,\zeta)$, the small group is $4mm$ and the irreducible representations are

$$4\Delta_1 + \Delta_2 + 5\Delta_5 \tag{3.32}$$

The normal modes Δ_1 and Δ_2 are longitudinally polarized modes, while those represented by Δ_5 are doubly degenerate transverse optical modes.

At the [001] zone boundary the little group is $4/mmm$ and the irreducible representations are

$$2M_1 + 2M_2' + M_3 + 3M_5 + 2M_5' \tag{3.33}$$

[7]It is important to realize that the effective electric field acting upon an ion is different from the macroscopic field. The latter is not simply the total field, which includes the field of the ion under consideration; it is the total field averaged over the space occupied by a lattice cell. The effective field, on the other hand, is the total field taken at the centre of the ion, with the contribution of the ion itself excluded.

The representations M_5 and M_5' correspond to doubly degenerate transverse modes, while the other modes are longitudinally polarized.

For $\zeta = (0,0,\zeta)$, the little group is mm except at the zone boundary where it is $4/mmm$. The irreducible representations are

$$5\Sigma_1 + \Sigma_2 + 5\Sigma_3 + 4\Sigma_4 \tag{3.34}$$

and

$$M_1 + M_2 + M_2' + M_3 + 2M_3' + M_4 + M_5 + 3M_5' \tag{3.35}$$

respectively. There are no degeneracies at general points, but at the zone boundary there are four doubly degenerate normal modes.

Finally, for $\zeta = (\zeta,\zeta,\zeta)$, the little group at a general point is $3m$ and its irreducible representations are

$$4\Lambda_1 + \Lambda_2 + 5\Lambda_3 \tag{3.36}$$

At the zone boundary the little group symmetry is increased to $m3m$ and the irreducible representations are given by

$$\Gamma_2 + \Gamma_{12}' + \Gamma_{25} + \Gamma_{25}' + 2\Gamma_{15}$$

In the [111] direction there are five longitudinal modes, Λ_1 and Λ_2, and five doubly degenerate transverse modes, Λ_3. At the zone boundary there are four triply degenerate normal modes, one doubly degenerate pair, Γ_{12}' and a single normal mode, Γ_2'.

3.6.4 One-Phonon Raman Scattering

In Section 3.4 the polarizability was expanded in powers of the phonon coordinates enabling the Raman scattering by one-phonon processes to be calculated. Symmetry arguments may be used, however, to restrict the different terms in the summation over the phonon branches. If processes in which the magnitude of the wavevector transfer, $\vec{\mathbf{Q}}$, are neglected (i.e. processes involving Brillouin scattering[8] and piezoelectric crystals[9]), then deducing the restrictions using group theory is a relatively straightforward process. Within

[8]Brillioun scattering is scattering by acoustic modes for which the frequencies of the created phonons clearly depend on the wavevector transfer.

[9]In piezoelectric crystals, infrared active modes couple with the photons in the crystal to give a Raman spectrum which is also strongly dependent upon the momentum transfer.

the adiabatic approximation, the polarizability is a second rank tensor which has six independent components. These components form a representation which may be reduced to give the irreducible representations of the point group. For the point group $m3m$ the representations are:

$$\Gamma_1 + \Gamma_{12} + \Gamma'_{25} \tag{3.37}$$

These different irreducible representations correspond to a different form of polarizability, e.g. Γ_1 and Γ_{12} are of the form $P_{\alpha\beta} = C_1\delta_{\alpha\beta}$, while for Γ'_{25}, $P_{\alpha\beta} = C_2(1 - \delta_{\alpha\beta})$. The forms of these matrices for the different representations of all the crystal point groups are given in Ref. [51].

It follows from the methods of group theory, presented in Section 3.6.1, that a single phonon will contribute to the polarizability if and only if it belongs to one of the irreducible representations present in the reduction of the polarizability. Hence, a comparison of Eqs. 3.31 and 3.37 immediately shows that there are no first-order Raman-active phonons in the perovskite structure. The ease with which this result is obtained exemplifies the usefulness of the group theory method in evaluating Raman processes in crystals.

3.6.5 Two-Phonon Raman Scattering

The selection rules for the two-phonon Raman processes may be obtained using very similar techniques to those described for the one-phonon process. The transformation properties of the product $A(\vec{\mathbf{q}}j)A(-\vec{\mathbf{q}}j')$ may be calculated by reducing the product of the irreducible representation of mode $(\vec{\mathbf{q}}j)$ with that of mode $(\vec{\mathbf{q}}j')$ within the little group of the wavevector, $\vec{\mathbf{q}}$. The polarizability is then also expressed in terms of these irreducible representations and hence the selection rules are obtained. The selection rules for the two-phonon Raman process in the perovskite structure, considered earlier, have been determined by Cowley [50]. The Raman spectra of many other molecular [72], ionic, covalent and metallic crystals [73] have also been considered in detail.

3.6.6 Identification of Phonons

In the preceding sections, Raman scattering by one-phonon processes has been discussed and its symmetry properties evaluated. In this section, these results will be expanded upon and the use of selection rules to identify different phonon types will be considered. Most Raman experiments are carried out by scattering through 90°. An example of such

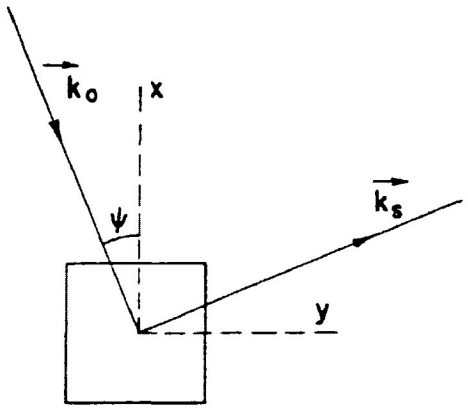

Figure 3.4: Schematic diagram of a typical scattering configuration with the z axis of the crystal perpendicular to the scattering plane.

an arrangement is illustrated in Fig. 3.4. As evident from this diagram, the crystal z-axis is perpendicular to the plane of the scattering and the x-axis is at an angle ψ to the incident light. Previously, in Section 3.6.2, the symmetry of the Raman tensor was discussed and it was shown that in cubic crystals there are three components to this tensor, I_{xxxx}, I_{xyxy}, and I_{xxyy}. When both the incident and scattered light are polarized in the scattering plane the intensity is given by

$$\frac{1}{2}\left(I_{xxxx} - I_{xxyy}\right)\sin^2 2\psi + I_{xyxy}\cos^2 2\psi \tag{3.38}$$

If the incident light is polarized in the scattering plane and the scattered light perpendicularly, the intensity is I_{xyxy}. If the incident light is polarized perpendicularly to the scattering plane, the intensity is I_{xyxy} in the scattering plane and I_{xxxx} perpendicular to it.

A commonly used method of denoting the crystal and polarization directions in Raman experiments is referred to as Porto notation. In this notation, the scattering geometry is usually expressed as $A(BC)D$; where A is the direction of incident radiation $\vec{k}_o$, B is the direction of incident polarization $\vec{E}_B$, C is the direction of observed polarization $\vec{E}_C$, and D is the direction of observation $\vec{k}_s$. The letters in parentheses give the components of the polarizability tensor that are measured by the observation.

An important quantity in many Raman scattering experiments is the depolarization ratio ρ. This quantity is defined as the ratio of the scattered intensity, polarized perpendicular to the plane of the scattering, to that of the intensity polarized in that plane.

In the example of Fig. 3.4, for unpolarized light, the ratio is given by

$$\rho = \frac{I_{xxxx} + I_{xyxy}}{\frac{1}{2}(I_{xxxx} + I_{xxyy})\sin^2 2\psi + I_{xyxy}(1 + \cos^2 2\psi)} \tag{3.39}$$

It is clear that the depolarization ratio depends on the crystal orientation.

Using the expressions for the intensity of the Raman scattering as a function of various crystal orientations and polarizations of the light, it is possible to distinguish between the modes on the basis of polarization measurements. The one-phonon Raman scattering enables the frequencies and the symmetry assignments of the long wavelength phonon modes to be obtained. This information may then be compared with that obtained from other experimental techniques and used to deduce models for the interatomic forces in crystals.

3.7 Scattering by Defects and Electronic Excitations

While outside the scope of this brief review, scattering by defects and electronic and magnetic excitations can also play a large role in the Raman spectra of crystals. In the case of defects, the presence of an impurity destroys the translational periodicity of the lattice and hence the $\vec{k} = 0$ selection rule. This makes it possible to induce a first order Raman spectrum in crystals which do not normally possess one. Also, in many such cases the first order line spectrum is replaced by a continuous spectrum reflecting the singularities in the frequency spectra and the resonant local modes [74]. Reviews of Raman scattering by defects and a variety of electronic and magnetic excitations are given in Refs. [75, 76] and [77].

3.8 Application to Material Characterization

Using the methods described in this chapter, various properties of semiconductor samples can be characterized. Many specific Raman techniques, summarized in Refs. [78] and [79] have been used to conduct tailored investigations of semiconductor interfaces and heterojunctions. Raman spectroscopy is particularly well suited to investigations pertaining to the composition and crystal structure of alloy compounds. As well, Raman techniques are commonly applied to measure stress and strain in thin semiconductor films. A number of characteristic examples of such measurements are briefly reviewed in the following sections.

3.8.1 Alloy composition

As noted above, the Raman spectra of alloy semiconductor films can yield much information on the composition of these materials. In a study of $In_{1-y}Al_yAs$ grown on InP, Emura *et al.* [80] showed that the Raman spectra displayed a two-mode behavior involving both AlAs- and InAs-like modes. They concluded that the ratio of intensities of the peaks of these modes was proportional to the corresponding ratio of their compositions. As well, the frequency of the AlAs-like mode was found to increase linearly with increasing Al composition, while the frequency of the InAs-like mode was found to be independent of In composition.

A similar study of $In_xGa_{1-x}As$, lattice-matched to InP, by Estrera *et al.* [81] also established the existence of two-mode behavior in this ternary alloy. A linear relationship between the Raman frequencies and film composition, as determined from x-ray diffraction studies, was found for near-latticed-matched conditions ($0.42 < 1 - x < 0.52$). In addition, another phonon mode was identified and attributed to compositional alloy disorder in the films under investigation.

3.8.2 Stress and strain in thin films

In addition to measuring the composition of alloy heterostructures, Raman spectroscopy can also be used to quantitatively study the strains present in heteroepitaxial films [82]. In an investigation of $In_xGa_{1-x}As$ films grown on GaAs, Burns *et al.* [83] measured the phonon frequencies (Raman technique) and the strains (x-ray rocking curve technique) of films ranging from perfect epitaxial to those that were relaxed by different amounts. They then calculated the strain-induced frequency shifts of the samples using the phonon deformation constants and the measured strains. From their measurements and calculations they were able to show that the frequency shifts due to the strain and the equivalent bulk frequencies for the phonon gave internal agreement.

These techniques have been further applied to more complicated structures. Recently, Gilpérez *et al.* [43] used the Raman method to analysis the strain in a series of MBE-grown InGaAs/AlGaAs pseudomorphic heterostructures. In this work, Raman scattering experiments performed on both strained heterostructures and bulk-relaxed reference layers, allowed a direct measurement of the strain from the observed shift in the GaAs-like *LO* phonon frequency.

3.8.3 Crystalline structure

As noted above, it is possible to draw important conclusions regarding the crystalline quality of materials using the Raman technique [84, 85]. For example, Welch *et al.* [86], in a study of $Al_{0.48}In_{0.52}As$ films grown by MBE, used the ratio of the allowed *LO* phonons (of both the AlAs- and InAs-like type) to their respective forbidden TO phonon counterparts, as an indication of crystalline quality. Previous studies [87] had found intensity ratios of 1:1, but Welch *et al.* found ratios of high as 10:1 and interpreted this result as an indication of high quality crystalline materials. Also in this study, the line width of the Raman peaks were investigated as a function of substrate growth temperature. In cases where the line width increased, the broadening was deemed to be caused by a reduction in the correlation length within the crystal (after Parayanthal *et al.* [88]). It was concluded that as more crystalline defects occurred, the correlation length within the crystal was decreased, thereby increasing the uncertainty in the wavevector of the phonon. This in turn, relaxed the $\vec{k} = 0$ selection rule and hence gave rise to transitions further out along the phonon dispersion curve.

Chapter 4

Experimental Procedure

4.1 Photoluminescence Instrumentation

As briefly outlined in Chapter 1, the primary materials of interest in this study are $Cd_{1-x}Mn_xTe$ ($0 \leq x \leq 0.69$) and $In_{1-x-y}Ga_xAl_yAs$ ($x + y \simeq 0.47$). The corresponding energy gaps E_g at low temperatures for these alloys are $1.6 - 2.7$ eV and $0.81 - 1.51$ eV, respectively. Hence, in order to study these materials in and below their fundamental gap regions, it was necessary to investigate the spectral energy range from $0.5 - 2.7$ eV. In terms of the units often employed in spectroscopy[1], the wavelength range is 2.5 μm - 460 nm and the wavenumber range is $4,000 - 22,000$ cm^{-1}. To perform the PL measurements over such a wide spectroscopic range it was necessary to utilize two different optical instruments, namely a fast-scan Fourier transform infrared spectrometer and a dispersive grating-based triple spectrometer.

The basic experimental apparatus employed in the PL investigations undertaken in this work is illustrated in Fig. 4.1. The photoluminescence signal was excited with either a Spectra-Physics HeNe laser or an Innova 70-4 argon ion (Ar^+) laser manufactured by Coherent. The HeNe laser emits a 20 mW unpolarized beam at 632.8 nm, while the Ar^+ ion laser is capable of putting out up to four watts of cw power in multi-line operation. A prism on the back end of the Ar^+ laser cavity can be added so that single lines may be selected. The 70-4 lases on eight lines between 457.9 nm and 514.5 nm with a maximum single-line output of 1.7 watts available at the latter wavelength. The use of lasers as excitation sources

[1]Note that $h\nu$ (eV) $= 1.239852/\lambda_{vacuum}(\mu m) = 1.239852 \times 10^{-4} \nu_{vacuum}(cm^{-1})$ and that $\lambda_{vacuum}/\lambda_{air} = 1.00028$.

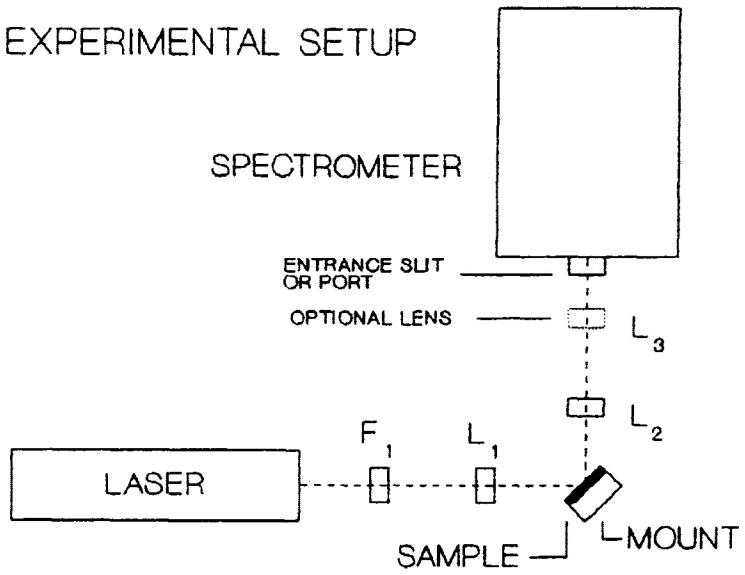

Figure 4.1: Typical experimental setup for optical characterization investigations.

not only permits localized spatial resolution at the sample but also allows a determination of the sample penetration depth.

As shown in Fig. 4.1 the laser light must be passed through filter F_1 to suppress unwanted laser plasma lines before it can be focussed onto the sample. These filters are available in both interference and dispersive-based forms. The interference type of filter is the more commonly used of the two and typically has losses of about 50%. The dispersive based filters, while offering losses as low as 10% in some cases, do suffer from the fact that their ability to separate spectral components is directly dependent upon the physical distance between the dispersing element and the occluding aperture. Once the beam has passed through the filter it is focussed by lens L_1 to a spot on the sample, typically 0.2 mm in diameter.

Samples were cemented to the cold finger of a CTI closed cycle helium refrigerator using rubber cement. Only one corner of the sample was attached to the finger to prevent strain after cooling. The cold finger is equipped with both resistive heating wire and GaAs diode thermometry allowing precise temperature control from 11 - 300 K. The PL measurements were normally carried out in the 90° scattering geometry. Lens, L_2, (in Fig. 4.1) is chosen so that it collects the optimum solid angle of radiation emitted from the sample. This lens in normally coated with an anti-reflecting film having minimum reflectivity centered near the spectral region of interest. Once collected, the light from the sample is either directed as a collimated beam into the external port of the FTIR or focussed onto the entrance slit of the triple spectrometer. In the following sections we will briefly examine

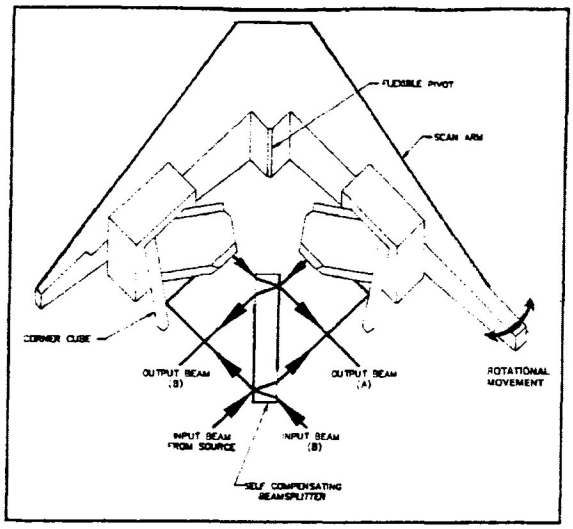

Figure 4.2: Light path inside the MB series Michelson interferometer.

the design, operation and limitations of each of these two systems.

4.1.1 Fourier Transform Infrared Spectrometer

Figure 4.2 (from Ref. [89]) shows the light path inside the Bomem Inc. MB-155 Series Michelson Interferometer. The incoming collimated beam from the external source port strikes the lower portion of the beamsplitter at a 45° angle. The transmitted and reflected beams hit the lower portion of the hollow cube corner retroreflectors and the return beams are shifted upward because of the reflections inside the cube corners. The beam then recombines in the upper portion of the beamsplitter. Two beams exit the interferometer, one at 90° to the incoming source radiation (output beam A) and one back to the source but displaced vertically (output beam B).

The common configuration of a Michelson interferometer, shown in Fig. 4.3 (from Ref. [89]), uses a compensator plate to equalize the amount of beamsplitter material that each beam passes through. In this design, each beam undergoes four passes through the compensator and beamsplitter substrate material. At each interface, reflection losses occur which lower the overall efficiency of the interferometer system. The design of the MB-155 used in this study is shown in Fig. 4.4 (from Ref. [89]). Here the IR beam in each arm undergoes the same number of passes through the beamsplitter substrate material. This design eliminates the need for a compensator plate and minimizes the reflection losses in the system, thus increasing the overall efficiency of the interferometer.

Digitization of the interferogram produced during the operation of the MB-155

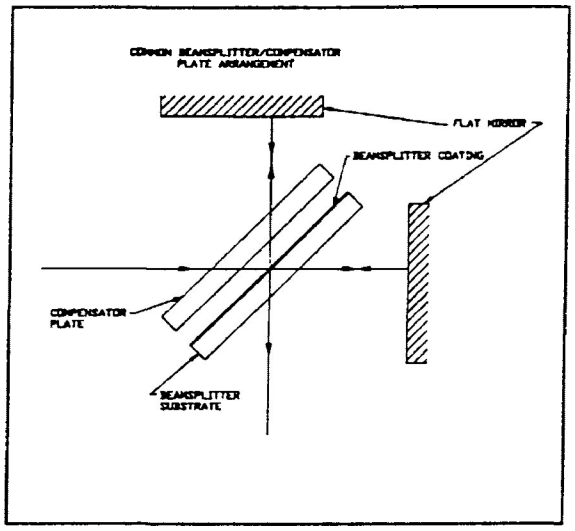

Figure 4.3: Common beamsplitter/compensator plate arrangement.

requires precise monitoring of the optical path in the interferometer. This is accomplished by an internal HeNe laser emitting at 15,803 cm^{-1}. Figure 4.5 (from Ref. [89]) shows the travel of the HeNe laser light inside the interferometer. This monochromatic laser radiation gives a sinusoidal interferogram which is detected and digitized to yield an optical path difference feedback. Conversion of the infrared signal from analog to digital is triggered at the zero crossings of the laser fringe signal. However, a single laser is not enough. First of all, the direction in which the scan arm is moving needs to be detected in order to correctly monitor and control the optical speed of the interferometer. Secondly, the laser signal itself does not give a reference point from which the location of the zero path difference can be determined.

To solve the first problem, quadrature laser signals are used to find the scanning direction. Figure 4.5 schematically shows what happens to the incoming laser beam. The incident beam is randomly polarized and can then be seen as two different but colinear beams, one horizontally polarized and one vertically polarized. The beams are separated and recombined in the interferometer much like the infrared beam, but in one of the arms, the beams are transmitted through a special birefringent optical material. The index of refraction of this material has the useful characteristic of giving a different optical retardation for the horizontally and vertically polarized beams. This means that an optical path difference is introduced between the two polarizations. At the output of the interferometer, these two polarizations are separated from one another and directed to different detectors. If one monitors the laser intensity at these two detectors, they will find that there is a shift

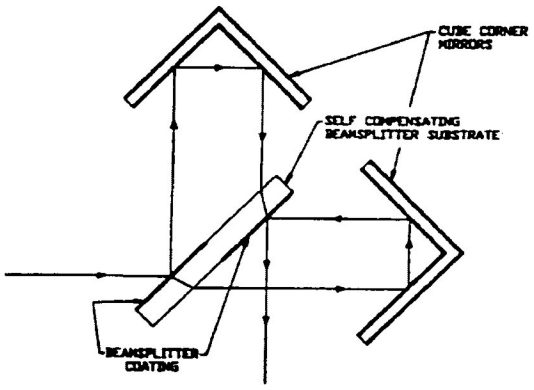

Figure 4.4: MB series self-compensating beamsplitter arrangement.

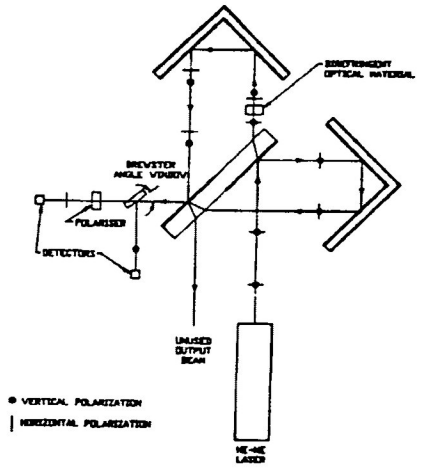

Figure 4.5: HeNe laser light path within the MB series interferometer module.

between the two observed sinusoidal waveforms. The digital electronics recognizes the relative phase relationship and can determine direction from these two signals. This technique is extremely accurate, allowing millions of scans to be executed without a single fringe count error.

The second problem necessitates the use of a temporary white light system in order to find the zero path difference location. This is done with a temporary white light system. Each time the spectrometer is turned on, or when excessive vibrational forces cause the unit to reset itself, a small visible source is lit whose radiation goes through the interferometer using the portion of the beamsplitter that the laser uses. The detected

white light interferogram is a sharp spike because of the high optical frequency content and broadband emission of the visible source. This signal is detected and used to determine the position of the zero path difference. Once the system has identified this location, the white light source is turned off until the system is reset again.

The principal advantage of Fourier transform (FT) spectroscopy is a consequence of the fact that the interferogram contains information about all spectral elements (Fellgett or multiplex advantage). To briefly expand upon this, we designate the number of spectral elements by N. Each particular spectral element is therefore studied for the total time T which is required to record the interferogram. In a grating spectrometer, in contrast, one studies the spectral element only during the time interval T/N, thereafter switching to the next spectral element. Since the accuracy of spectroscopy in the IR is limited, to a large extent, by the noise from the detection system, a gain in the signal-to-noise ratio is realized using Fourier transform spectroscopy compared to conventional grating spectroscopy. For equal times of observation this amounts to $\sqrt{N}$. Consequently, for equal signal-to-noise ratios in both spectroscopic techniques, the measuring time is considerably shorter in FT spectroscopy.

While the multiplex advantage of FT-IR spectrometers may enable them to gather a full high quality infrared spectrum in a few seconds, the necessary transformation of raw interferograms to usable spectra is very computer intensive. This Fourier transform step often greatly offsets the FT-IR speed advantage when performed on low cost microcomputer-based systems. In order to reduce this calculation time to nearly zero, relative to the computation time on an IBM/AT type computer, the MB-155 was used in conjunction with a DSP100 digital signal processor. The DSP100 is an IBM/AT compatible electronic board based on a 10 MIPS (million instructions per second) Digital Signal Processor circuit from Motorola. The board has 64 Kilobytes of on-board fast static RAM and when interfaced with the MB-155 is capable of transforming a 32,768 points interferogram to a 1 cm^{-1} resolution raw spectrum in 391 ms [90]. This directly provides the host microcomputer with a usable spectrum allowing it to perform other tasks while data is being collected.

The MB-155 can be used in conjunction with several interchangeable detectors allowing highly sensitive measurements to be carried out over the entire spectral range of the beamsplitter (14,000 - 400 cm^{-1}). For optimum speed and sensitivity in the energy region of interest in this work, either InSb or Si detectors were normally employed. The InSb detector is a high quality, LN_2 cooled, single crystal p-n junction. It yields a high speed,

low noise signal with excellent uniformity, linearity and stability and provides excellence performance ($D^* \simeq 1 \times 10^{11}$ cm·Hz$^{1/2}$W^{-1}) in the 12,000 to 1,800 cm^{-1} region. The Si detector, while only useful from 14,000 to 9,000 cm^{-1}, operates at room temperature and is about two orders of magnitude more sensitive than the InSb detector over this range. The resolution of the MB-155 instrument is variable from 2 to 128 cm^{-1} using these detectors and has an ultimate resolution of 1 cm^{-1} when used in conjunction with a DTGS detector over a limited range (7,901-400 cm^{-1}). Although the MB-155 was an invaluable instrument used in a large fraction of the PL investigations undertaken in this work a number of specific studies did require the use of the dispersive spectrometer described below. Reasons for this change in instrument include:

1. Some of the samples studied required investigation of spectral regions beyond the 14,000 cm^{-1} high energy limit imposed by the FTIR beamsplitter.

2. Photon-counting sensitivity for long spectral scans was required when studying PL signals from the $E_o + \Delta_o$ gap region of several of the materials characterized.

3. Some of the investigations undertaken required higher resolution than the 2 cm^{-1} offered by the FTIR spectrometer above 7901 cm^{-1}.

4.1.2 Dispersive Grating-Based Triple Spectrometer

The triple monochromator system used in this work consists of a DHR-320S medium resolution, subtractive double monochromator (manufactured by Jobin Yvon) used as a pre-filter for a dispersive single monochromator. The filter stage is a 320 mm focal length, subtractive double monochromator with an aperture of $f/4.4$ and an entrance slit typically set between 50 and 100 μm. It contains two 600 groove/mm ruled, (68 mm $\times$ 68 mm) gratings, blazed for 500 nm attached to a single shaft. This results in a maximum resolution of 0.8 nm and a reciprocal linear dispersion of 4.8nm/mm, with a stray light rejection ratio of 5×10^{-9} measured 8 nm from the 632.8 nm HeNe laser line.

A typical double monochromator dispersing system is shown in Fig. 4.6 (from Ref. [91]). C_1 to C_4 are concave mirrors for collimating and focussing the radiation, C_5 and C_6 are plane mirrors, G_1 and G_2 are plane diffraction gratings and S_1, S_2 and S_3 are the entrance, intermediate and exit slits, respectively. A double monochromator is two single monochromators coupled is series so that their dispersions are either additive or subtractive.

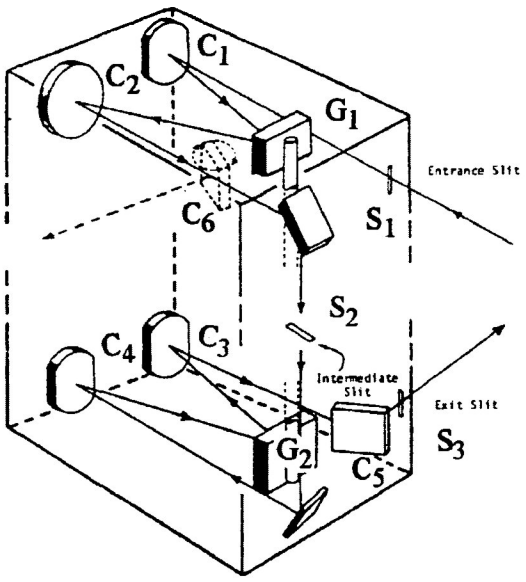

Figure 4.6: Light path in a typical double monochromator grating dispersing system.

In the DHR-320S the first grating disperses the input radiation and the second, which is coupled to the first grating in a subtractive dispersion mode (one grating has an angular offset), collapses the dispersed radiation so that the net result is zero dispersion at the entrance slit to the single monochromator. The band pass (intermediate) slit within the filter stage blocks unwanted radiation and passes a band of wavelengths. The band pass of the filter stage is dependent upon the dispersion of the two gratings as well as the slit width, which is adjustable from $0 - 200$ μm. The exit slit of this filter stage also acts as an entrance slit for the final dispersive stage and is usually set to a width of between 10 and 100 μm, depending on the application.

The HR-640 single monochromator used in this work was also manufactured by Jobin Yvon (Instruments S.A.). The light path inside the HR-640 is shown in Fig. 4.7 (from Ref. [92]). The light beam enters through entrance slit S_1 or S_3. The beam is then reflected by the collimator mirror M_2 which renders it parallel and directs it to grating G. The grating diffracts the light and sends a collimated spectrum to M_3 which focuses the image of the entrance slit at S_2 or as a spectrum at S_4. Wavelength scanning at the exit slit plane is accomplished by rotation of the grating.

The ability of a monochromator to differentiate between light of the narrow band selected $\lambda \pm \delta\lambda$, and light of other wavelengths is referred to as its spectral purity. It depends essentially upon factors like the resolving power, dispersion and slit width. Through defects in the dispersing system, mainly scattering at optical surfaces (particularly the grating), a small fraction of light of wavelength λ_o will appear in the output focal plane at positions

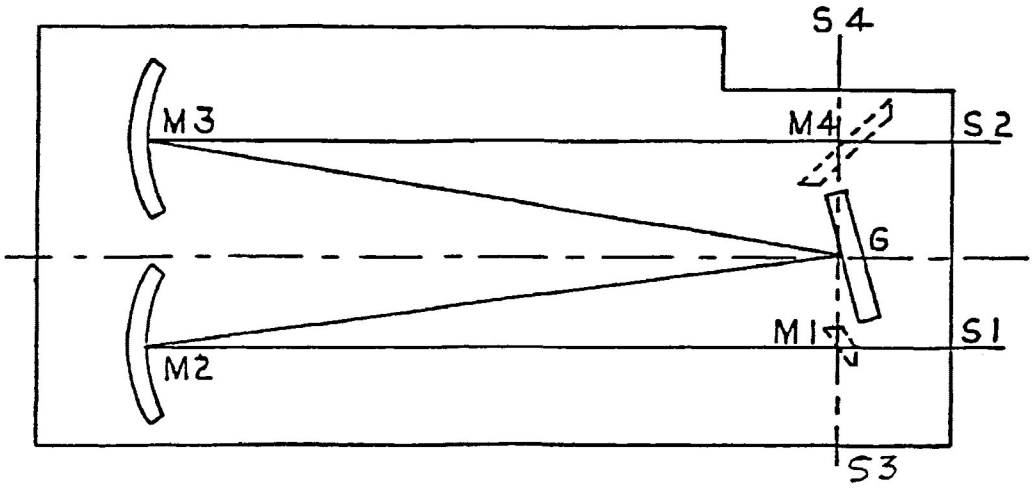

Figure 4.7: Light path inside the HR640 grating spectrometer.

corresponding to other wavelengths in the neighborhood of λ_o. In the HR640 about 10^{-5} or 0.001% of the radiation at $\lambda_o = 632.8$ nm will masquerade as light at 632.8 ± 1 nm.

The HR-640 is a 640 mm focal length single monochromator with an aperture of $f/5.5$. It contains a (110 mm $\times$ 110 mm) mount which can be fitted with a variety of gratings. When used in conjunction with an 1800 groove/mm holographic grating, the instrument has an ultimate resolution of 0.01 nm and a reciprocal linear dispersion of 0.8 nm/mm. If the output slit is set to 20 μm the resolution is given by

$$0.8\text{nm/mm} \times 0.02\text{mm} = 0.016\text{nm}$$

or 0 .6 cm^{-1} in the region of 514.5 nm. It should be noted that unlike the FTIR instrument described in the previous section, the triple spectrometer system is not internally calibrated. Calibration of this instrument is normally accomplished by comparing the emission spectrum of a known source obtained with the instrument, to that of a pre-calibrated standard. A low pressure Ne lamp was used for this purpose as it has a rich emission spectrum of very narrow lines (<1 cm^{-1}) ranging from approximately 400 to 1,000 nm.

Inclusion of the optional output mirror M_4 in the HR-640 light path (Fig. 4.7) determines whether the instrument is used as a scanning monochromator or as a spectrograph. If the mirror is removed from the light path then the image of the entrance slit is focussed at exit slit S_2 and the instrument is in the monochromator mode. If it is placed within the light path the image of the entrance slit is focussed as a spectrum at exit slit S_4 and the HR-640 is setup in the spectrograph mode. As will be seen below, the type of

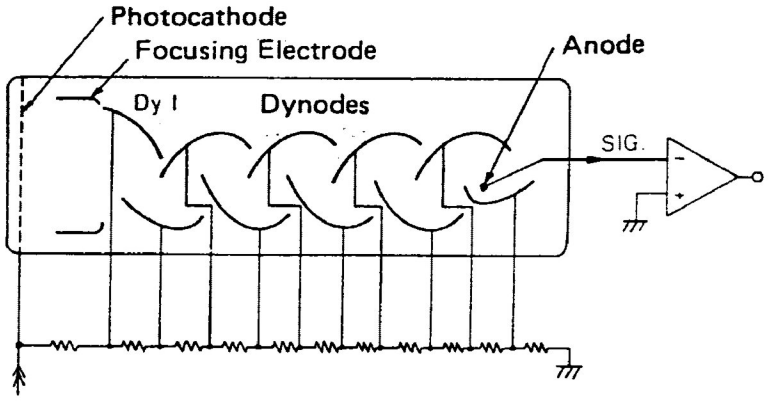

Figure 4.8: Typical configuration of a photomultiplier tube (PMT).

detectors used in combination with these two configurations are quite different.

When the instrument is configured as a monochromator it is used in conjunction with a photomultiplier tube (PMT). The PMT, as shown in Fig. 4.8 (from Ref. [93]), consists of a photoemissive surface called a photocathode, secondary emission electrodes called dynodes, and an anode with a potential difference set up between the various electrodes. The photocathode emits electrons with a given quantum efficiency in response to incident photons striking its surface. Being attracted by the potential difference between the photocathode and the first dynode, the emitted electrons are drawn to the first dynode and cause the secondary emission of electrons when they strike its surface. This process is repeated throughout the series of dynodes until finally a large charge is available at the anode as the output signal.

Such PMT's, because of their high intrinsic S/N ratio, fast response, and high gain, are very useful for the measurement of extremely low light levels. The photomultiplier tube used in this work was an R943-02 photon-counting PMT manufactured by Hamamatsu. This detector is of the head-on type and consists of an opaque GaAs:Cr photocathode in combination with ten dynode stages. It was normally run at an anode-to-cathode voltage of -2,000 volts as supplied by a Keithley high voltage supply. The PMT is responsive from $160 - 930$ nm, but is most sensitive throughout the $300 - 700$ nm region. It has a D* value approximately two orders of magnitude greater than that of the Si detector used with the MB-155. The quantum efficiency, or percentage of photons that enter the detector and are actually sensed by the PMT, is very high, i.e. 50%. This means that one pulse is

created for every two photons striking the cathode. To reduce dark current noise the PMT is used in conjunction with a water-cooled thermoelectric cooler and normally operated at -25 C°. The output from the photomultiplier tube was fed to an Ortec model 9301 fast preamplifier which amplified the signal. An Ortec model 9302 amplifier discriminator was used to discriminate against low level pulses originating from thermally emitted electrons. A counter/timer operated under computer control was then used to count the pulses over a specified time interval.

This combination of instrument (monochromator and photon-counting PMT) is normally used in the scanning mode and offers very high sensitivity in the detection of low light level phenomena. When in operation, precautions must be taken to prevent exposure of the PMT to high light levels (i.e. normal room light) which would rapidly destroy the tube. The major disadvantage associated with the scanning monochromator is the long collection times that are required when covering broad energy ranges. As well, small movements in the collection apparatus and or laser beam during such scans can drastically change the intensity of signal detected.

When the optional output mirror M_4 (in Fig. 4.7) is in place and the HR-640 is configured as a spectrograph, a CCD spectroscopic multichannel analyzer (CSMA) is used as the detection system. The CSMA is a computer controlled, two-dimensional multichannel image detector capable of detecting, measuring and manipulating spectra at high acquisition rates. It has a large dynamic range (16 bits/exposure ADC 65536:1) and displays both excellent thermal and temporal stability. The particular system used in this study (manufactured by Princeton Instruments Inc.) consists of an IBM/AT type computer, a detector controller, and a LN_2-cooled charge coupled device (CCD) array detector. The ST-130 detector controller provides power, thermostating, and timing signals to the detector head, coordinates data gathering with the experiment, sets the exposure time, digitizes and averages data, and transmits it to the computer. To understand how data is collected by the CSMA it is useful to briefly consider how the CCD array operates.

A charge coupled device can be thought of as a two dimensional grid of individual photodiodes (pixels), each containing its own charge storage "well". Each pixel senses the intensity of light falling upon its collection area, and stores a corresponding amount of charge in its associated "well". Reading out the data stored in the CCD in spectroscopic mode corresponds to sequentially shifting the charge from one column of "wells" to the next, column by column. With each shift, one column of charge is moved to the shift

register, a special column of "wells". Once the charge from a column of pixels reaches the shift register, the shift register "wells" are emptied out one at a time into the measurement circuitry which determines and records the amount of charge found in each. In this manner it is possible to form an electronic map of the optical image on the array.

The CCD array detector used in this system is an area array consisting of 576×384 pixels, each with an area of 22 μm $\times$ 22 μm. The array has exceptionally low readout noise ($12 - 16$ electrons rms) and very few dark counts ($\simeq$typically $3 - 6$ electrons/pixel/hour). It has an extremely linear response (better than 1%) over its entire range of operation ($400 - 1,060$ nm). Its quantum efficiency varies from $5 - 28\%$ with peak sensitivity occurring near 825 nm.

The combination of spectrograph and CCD array detector is particularly well suited to investigations over relatively narrow energy regions (defined by the grating chosen and the finite width of the pixels in the array). The array is specifically designed for exposure during long signal integration times (i.e. minutes to hours) and this is important when dealing with low light level signals. Depending on the spectral region under investigation the CCD array is typically $2 - 10$ times less sensitive than the PMT described previously.

4.2 Raman Instrumentation

The experimental setup employed in the Raman investigations undertaken in this work is essentially identical to the triple spectrometer apparatus used for some of the photoluminescence measurements as described in the previous section. There are however, a number of considerations worth noting.

Most of the Raman spectra were taken using the triple spectrometer in combination with the CCD array detector. As mentioned above, this setup is particularly well suited to investigations over relatively narrow energy regions. Since most of the Raman spectral information for the materials studied in this work is found within 500 cm^{-1} of the Rayleigh line, it was often possible to analyze the entire region of interest in a single wavelength sampling.

The stray light rejection ratio, also considered earlier, is of utmost importance in the study of Raman scattering. Rayleigh scattering, which always occurs with Raman scattering, is typically 10^{12}-10^{14} times more intense than Raman scattering in solids and can easily overwhelm the Raman signal if the rejection ratio of the instrument used is too

low. Recent advances in the development of holographic reject filters hold promise for future investigations. Filters designed for use with the common Ar^+ ion laser lines have optical densities[2], $O.D. = 4$ across a 350 cm^{-1} wide region and transmit over 80% ($O.D. = 0.1$) of the light outside this band. The high $O.D.$ band, or "notch", is tunable up to 10 nm by angular rotation of the filter between $\theta = 0 - 15°$. Hence, use of a single monochromator in combination with two of these filters in series yields a theoretical stray light rejection ratio of approximately 10^{-13}.

The FTIR instrument, heavily utilized in the NIR-MIR photoluminescence studies, could not be put to use in the Raman investigations because:

1. The sensitivity of the detectors available on-site for use with the FTIR instrument are significantly lower than that required. Typically a LN_2-cooled InGaAs detector would be used.

2. The MB-155 is equipped with a multimode HeNe laser for internal calibration. When looking for weak signals, characteristic of the Raman scattering process, internal scattering from these multimode laser lines will be comparable in intensity to the Raman scattered radiation, and may in fact overwhelm it.

[2]The optical density of a material is defined as the common logarithm of the inverse of its transmittance T (i.e. $O.D. = -\log_{10} T$).

Chapter 5

Results and Discussion

5.1 (111)CdTe/(111)GaAs and (001)CdTe/(001)InSb heterostructures

5.1.1 Introduction

Epilayer growth of a wide variety of II-VI semiconductor compounds, is currently attracting considerable attention for both single and multilayer applications [94, 95, 96, 97, 98, 99, 100, 101]. As many of the best quality, large area substrates are III-V compounds, considerable interest has been directed at the growth of II-VI materials on III-V substrates. In particular, the growth of micron thick epilayers of CdTe on GaAs has recently received attention [102, 103]. This attention has resulted from the fact that commercially available CdTe wafers do not exceed about one inch in diameter and more importantly, bulk CdTe is characterized by a large number of defects and dislocations that spread into epitaxial layers grown on such wafers. It is hoped that the arrangement of CdTe platforms on GaAs substrates may provide the CdTe epilayer with the large area, low defect density qualities of the substrate. As well as leading to the successful hybridization of II-VI materials with III-V GaAs, such materials would have important applications in the subsequent fabrication of infrared detector structures.

Another (II-VI) epilayer/(III-V) substrate heterostructure which has also received considerable recent interest is the CdTe/InSb material system [104, 105, 106]. This mixed heterostructure has a near perfect lattice match ($\Delta a/a \simeq 0.04\%$ at room temperature) and a large difference in band gaps between the constituent materials; CdTe ($E_g = 1.44$ eV) and

InSb ($E_g = 0.18$ eV). This band gap difference is accommodated by conduction and valence band offsets of the order of 0.3 and 0.95 eV, respectively. As a result, this material system offers great potential for the fabrication of quantum well lasers and detectors spanning the photon energy range from 0.2 - 0.5 eV (2.5 - 6.0 μm) [107, 108], as well as for high-electron mobility transistors (HEMT) [109, 110].

The CdTe films characterized in this report were grown using the pulsed laser evaporation and epitaxy technique (PLEE) at the National Research Council (NRC) of Canada in Ottawa, Ontario. There is considerable evidence that the PLEE approach offers sizable cost and materials handling advantages over more conventional methods of thin film deposition, and many high quality heterojunctions have been produced using this process [85, 111, 112, 113, 114, 115, 116]. During PLEE growth, some of the ablated ions and neutrals are more energetic than the vapour constituents of thermal evaporation processes and can range in energy up to hundreds of eV [115]. This can play a significant role during the epitaxy process as a built-in assist mechanism for surface atom migration.

In earlier studies [112, 113], Raman investigations showed that the PLEE technique produces epilayers of CdTe on both GaAs and InSb which exhibit high quality crystalline structure. In particular, the films grown on InSb were relatively free of indium-telluride complexes which frequently accompany other growth methods [117, 118]. The Raman measurements were carried out under near resonant conditions using the lines of an Ar^+ ion laser. Most of the shorter wavelength lines lie close to the $E_o+\Delta_o$ gap energy of the CdTe epilayer. Some photoluminescence (PL) from this $E_o+\Delta_o$ gap was observed accompanying the Raman signal from epilayers deposited on both the InSb and GaAs substrates. This PL was virtually absent when the Raman spectra for the CdTe target material was studied separately. Thus, the presence of the interface appears to have been a major factor in producing this effect. In this study the photoluminescence technique is employed to further investigate this higher gap luminescence for CdTe films deposited on both (111)GaAs and (001)InSb substrates.

5.1.2 Experiment

As mentioned above, the samples were grown using the PLEE technique which has recently been reviewed by Dubowski [115]. Crystalline CdTe was obtained from Cominco and is referred to as Target-A and Target-B materials. The targets contain small amounts

of different and initially undetermined residual impurities. The GaAs substrate, obtained from Sumitomo Electric Inc., was Si-doped to $\sim 2\times10^{18}$ cm^{-3} to facilitate direct electrical connection, while the p-type InSb was obtained from Cominco. Prior to deposition, the (111)GaAs substrate surface was degreased in standard solvents and etched for two minutes in a solution of H_2SO_4-H_2O_2-H_2O (7:1:1). It was then rinsed in deionized water, blown dry with N_2 and mounted on a Mo block using high purity In. Ion etching with 250 eV Ne^+ ions completed the surface treatment and produced a high purity surface suitable for the epitaxial growth of CdTe. With the exception of the acid etch, the InSb substrate surface underwent the same treatment. The CdTe epilayer was grown at approximately 300°C on the GaAs surface to a thickness of 2.2 μm. The InSb substrate was held at 190°C during growth and the film thickness obtained was 0.96 μm.

The photoluminescence signal was measured in the 2.68 to 1.40 eV range using the Instruments SA triple spectrometer and Hamamatsu R943-02 photon counting photomultiplier or Princeton Instruments CCD array detector as described in Section 4.1.2. Various lines of an Ar^+ ion laser were used for sample excitation and the beam was typically focused to a line image of approximately 0.2 mm × 3.0 mm using crossed cylindrical lenses to reduce the power density at the sample. Total power to the sample was approximately 10 mW in scans covering the 2.68 to 1.65 eV range (which includes the CdTe $E_o+\Delta_o$ region) and was reduced by a factor of five for scans covering the epilayer and substrate E_o gap range of 1.65 to 1.40 eV. The slit settings used produced a spectral resolution of approximately 4 cm^{-1}.

Overlapping spectra from 1.65 to 0.6 eV were obtained using the Bomem MB-155 FTIR instrument in the FT-PL geometry in combination with the liquid nitrogen cooled InSb detector. Approximately 3 mW of power from either Ar^+ ion or HeNe laser excitation was used in these scans. The FTIR resolution was set at 2 cm^{-1}. The PL measurements were carried out in the 90°-scattering geometry in both cases. The samples were cemented to the cold finger of the closed cycle helium refrigerator and cooled to 11.5 Kelvin.

5.1.3 Results

(111)CdTe/(111)GaAs:Si heterostructure

Figure 5.1 shows the photoluminescence spectra from (a) the Si-doped (111)GaAs substrate, (b) the CdTe Target-A ablation source material, and (c) the epitaxially grown

heterojunction. The GaAs substrate material exhibits broad unresolvable excitonic structure in the E_o gap region (1.52 - 1.30 eV) as well as strong luminescence centered near 1.2 eV. The latter appears to be due to the formation of Si clusters in the GaAs since the spectrum is nearly identical to that reported in Ref. [119] where an investigation of the annealing dependence of Si clusters in Si-doped GaAs was carried out. Further evidence supporting this designation is presented later in Section 5.2.3. It is important to note at this point that no discernible luminescence was detected above the E_o gap region of the GaAs.

Figure 5.1 (b) shows the PL spectrum of Target-A. The principle features are a gap-edge excitonic peak at 1.593 eV, with associated phonon replicas, and an intense deep lying impurity or defect component at 1.473 eV. No detectable PL signal was recorded above the CdTe E_o gap region (1.60 - 1.35 eV). In an attempt to determine the origin of the structure present in the PL spectra of this material, higher resolution investigations were performed and the results of such are presented in Fig. 5.2.

From examination of the inset in Fig. 5.2 it is possible to identify a number of gap-edge excitonic processes. The notation, line positions, and corresponding assignments for all the peaks found in Fig. 5.2 are summarized in Table 5.1. The high resolution (≈ 0.75 cm^{-1}) spectra of the inset shows clear free-exciton (FE) features and strong, partially resolved bound exciton (BE) lines. The peak denoted $(\chi)_{n=1}$ is the ground state of the FE, while that labelled $(\chi)_{UP}$ has been previously identified by Suga *et al.* [120] as the upper branch of the polariton-free exciton interaction. The exciton emission at 1.593 eV, denoted by D'_μ is commonly observed in CdTe and has been attributed to exciton trapping at shallow chemical donors by Noblanc *et al.* [121]. Using a binding energy of 2.3 meV (E_b = 1.5953 eV -1.593eV) and a ratio of 0.2, after Haynes' rule (described previously in Section 2.4.1) yields an ionization energy of 11.5 meV which is characteristic of shallow hydrogenic donors in CdTe [122]. Therefore, the 1.593 eV emission is associated with excitons trapped at impurity donors such as In or residual halogens and group III elements. The first two excited states of this BE are denoted by D'_ν and D'_λ. The shoulder on the low energy side of the dominant D'_μ structure, labelled D^+, is attributed to the recombination of excitons bound to the ionized state of the donor impurities or complexes responsible for the D' emission series.

In comparison with similar resolution measurements performed by Feng and co-workers [123] on MOCVD grown CdTe, the FE features at 1.5970 eV and 1.5953 eV in the

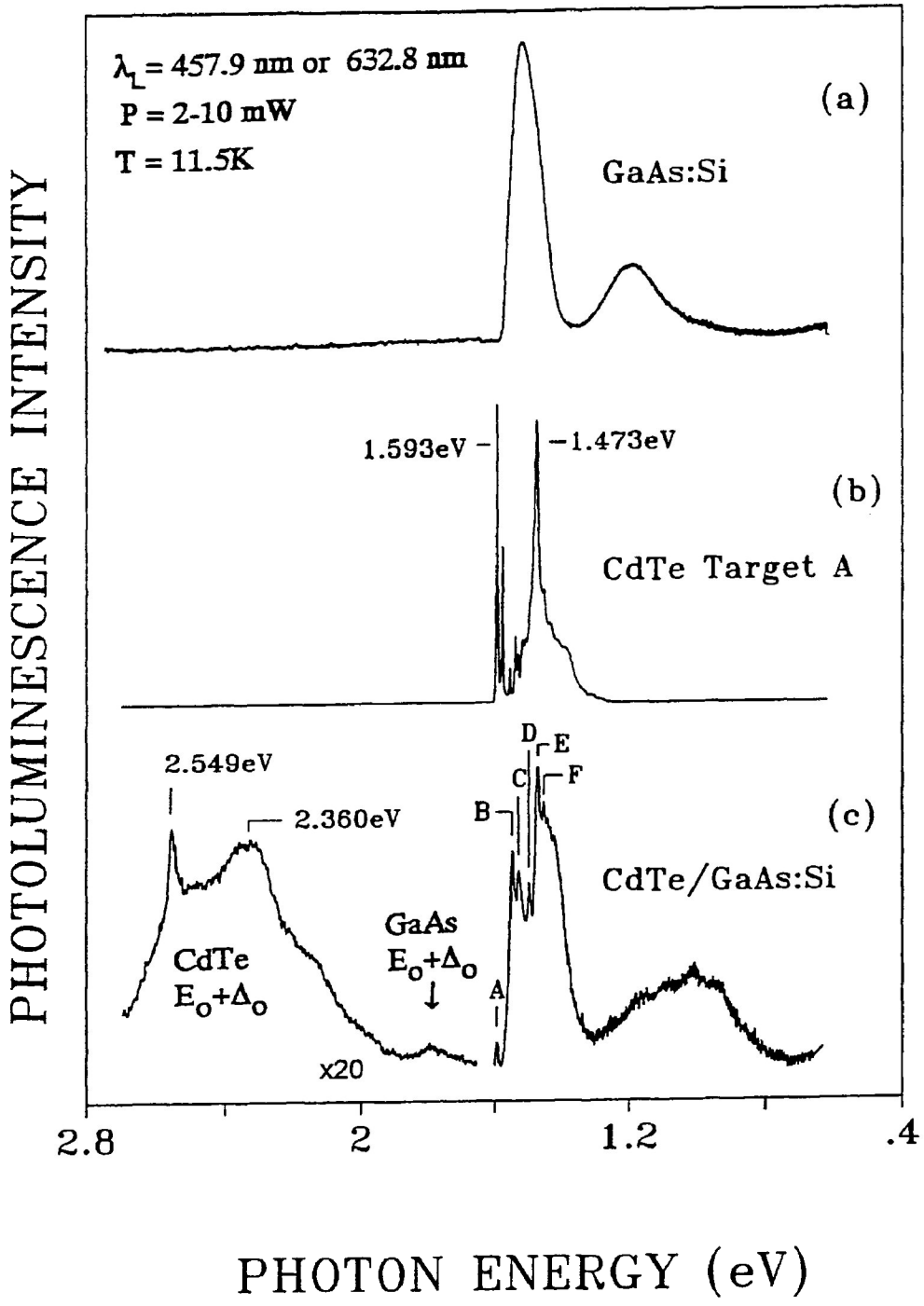

Figure 5.1: PL spectra of (a) the Si-doped GaAs substrate, (b) the CdTe ablation source material (Target A) and (c) a (001)CdTe/GaAs:Si heterojunction.

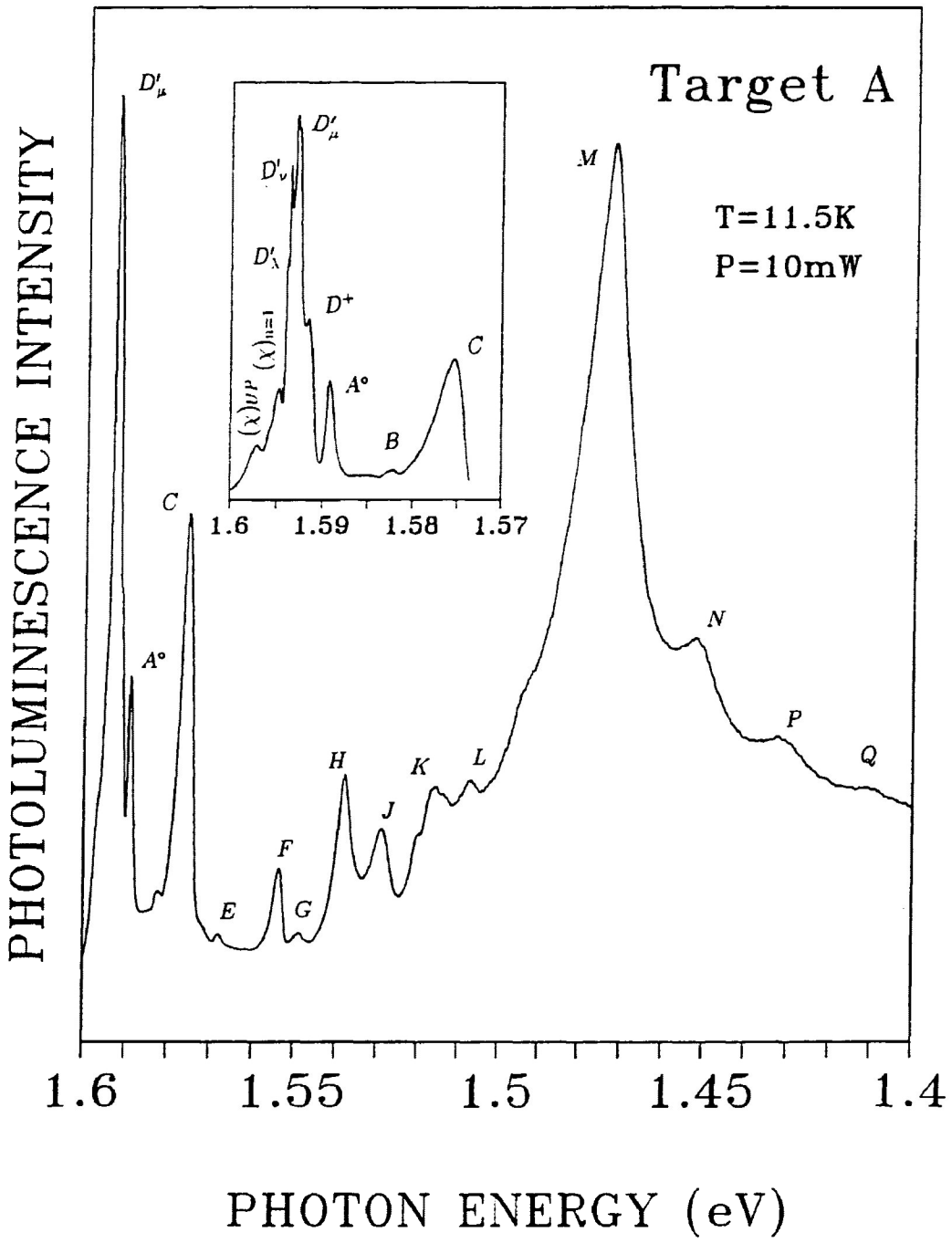

Figure 5.2: PL from CdTe ablation target material A. Inset shows the gap edge region of the material under higher resolution (approx. 0.75 cm-1).

Notation	Position (eV)	Assignment
$(\chi)_{UP}$	1.5970	FE upper polariton
$(\chi)_{n=1}$	1.5953	FE n=1 ground state
D'_{λ}	1.5941	(D^o, X) n=3 excited state
D'_{ν}	1.5937	(D^o, X) n=2 excited state
D'_{μ}	1.5930	(D^o, X) n=1 ground state
D^+	1.5916	(D^+, X)
A^o	1.5893	(A^o_{Na}, X) or (A^o_{Li}, X)
B	1.5825	(D^o, X) to leave D^+
C	1.5753	$(D^o, X) - TO$
E	1.5678	$(A^o, X) - LO$
F	1.5536	$(D^o, X) - TO - LO$
G	1.5489	$(A^o, X) - 2LO$
H	1.5380	(D^o, A^o_{Na})
J	1.5288	DAP
K	1.5155	$(D^o, A^o_{Na}) - LO$
L	1.5070	$DAP - LO$
M	1.4730	BE @ defect center
N	1.4517	$BE - LO$
P	1.4323	$BE - 2LO$
Q	1.4112	$BE - 3LO$

Table 5.1: Notation, position, and assignments for the emission lines in the 11.4 K PL spectra of CdTe target material A.

inset of Fig. 5.2 have the same energies as those denoted in a similar fashion in Ref. [123]. As well, the donor-BE lines at 1.5930 eV, 1.5937 eV, and 1.5941 eV in the inset of Fig. 5.2 are also in very good agreement with identically designated peaks in Ref. [123] at 1.5930 eV, 1.5936 eV, and 1.5940 eV respectively. The transition labelled A^o in the inset of Fig. 5.2 lies at 1.5893 eV and coincides well with a peak previously identified [31, 39] as resulting from the recombination of excitons bound to Li or Na acceptors. The ionization energies of Li and Na are too close together (57.8 meV and 58.8 meV, respectively [29]) to allow them to be resolved here.

The weak feature denoted by B lies approximately 10.5 meV below the (D^o, X) transition and as such is attributed to the recombination of donor-bound excitons where the donor atoms involved are left in an ionized state. The final prominent feature is the inset of Fig. 5.2 is labelled C and lies 17.7 meV below the principal (D^o, X) energy. As the TO-phonon energy in CdTe is $\simeq$ 17.3 meV [124], this feature may be a phonon replica of the higher energy (D^o, X) transition.

The three peaks in Fig. 5.2 denoted by E, F, and G have energies which lie close to expected phonon replicas of higher energy transitions and their tentative designations are also presented in Table 5.1. The features labelled H, J, K, and L are attributed to two different donor-acceptor pair transitions with their associated LO-phonon replicas. The H peak lies very close to (D^o, A^o_{Na}) and (D^o, A^o_{Li}) transitions at 1.539 eV and 1.540 eV, previously identified by Molva *et al.* [125]. The second DAP transition likely involves a different and unidentified acceptor.

The dominant feature in Fig. 5.2 is clearly that of the strongly luminescent, phonon-replicated, broad band centered near 1.473 eV. The origin of this structure, labelled M, has recently been the subject of much discussion [40, 126, 127, 128]. In particular, Onodera *et al.*, [126] while studying PL, PLE, and time-resolved PL from CdTe films grown on (100) GaAs substrates, concluded that this luminescence peak resulted from the recombination of excitons bound to extended defects, similar to that found in ZnSe by Dean *et al.* [127]. For a given BE transition, Dean and co-workers noted that the ratio of the intensities of the one-phonon replica line (I_1) to that of the zero-phonon line (I_0) rapidly increased with increasing values of binding energy E_b. Hence, based on the large value of E_b associated with the 1.473 eV transition, this ratio (referred to as the electron-LO phonon coupling strength, S) is expected to be $\simeq$ 2 and not 0.4 as determined from Fig. 5.2. An explanation for this discrepancy based on binding delocalization arguments is presented in

Ref. [127]. Once again, it is to be noted that no significant photoluminescence was observed above or below the E_o gap region of the target material.

The PL spectrum of the CdTe/GaAs:Si heterojunction, illustrated in Fig. 5.1 (c), shows numerous structures which appear to originate from both the target and substrate materials. In particular, much of the excitonic structure associated with the E_o gap region of the CdTe target material is found superimposed on a broad PL background arising from the underlying GaAs substrate. While interpretation of the resulting spectrum is greatly complicated by the addition of the substrate component, a number of features may be noted.

The first of these structures, labelled A, is the gap-edge donor-BE also found in the target spectrum of Fig 5.1 (b). While the relative intensities of the BE peaks in the target and film spectra are quite different, they both displayed a linear dependence upon excitation power density and hence, their intensities could be readily matched by adjusting the output power of the pump laser. The broad background signal extending from 1.52−1.30 eV occurs precisely at the region of the GaAs E_o emission illustrated in Fig. 5.1 (a) and hence, is believed to arise from the substrate. Three other peaks, denoted B, C, and D, are superimposed on this broad emission and occur at energies of 1.548 eV, 1.527 eV, and 1.498 eV, respectively. The 1.548 eV transition lies very close to a (D^o, A_N^o) transition at 1.547 eV in bulk nitrogen-doped CdTe [129]. The interaction of this peak with the CdTe *LO* phonon is, in turn, responsible for the 1.527 eV emission. Determining the origin of the 1.498 eV transition is complicated by the fact that phonon replicas of this peak, if they exist, lie under the high energy shoulder of the intense 1.47 eV emission, making their presence difficult to ascertain. If this peak is in fact a DAP transition, it may be related to a 1.491 eV (D^o, A_{Ag}^o) mechanism identified in a silver diffusion study of bulk CdTe by Chamonal *et al.* [30]. Also occurring in the heterojunction spectrum is the strong 1.47 eV luminescence peak discussed earlier. This emission, denoted by E, is again accompanied by several phonon replicas, the first of which is labelled F. Below the combined E_o region the broad luminescence emission (from 1.3 to 0.9 eV) appears due primarily to the GaAs substrate Si cluster processes with a smaller contribution from the CdTe. The mechanisms responsible for the evolution of the Si cluster luminescence are considered in more detail later in Sect. 5.2.3. The notation, peak position and tentative assignments of the features present in the PL spectrum of Fig. 5.1 (c) are summarized in Table 5.2.

In addition to the structure present in and below the CdTe E_o gap region, features also appear in the $E_o + \Delta_o$ gap regions of both the epilayer and substrate materials which

Notation	Position (eV)	Assignment
	2.549	CdTe $(E_o + \Delta_o)$
	2.360	$(E_o + \Delta_o)BE$ @ defect centre
GaAs $(E_o + \Delta_o)$	1.807	GaAs $(E_o + \Delta_o)$
A	1.594	(D^o, X) n=1 ground state
B	1.548	(D^o, A_N^o)
C	1.527	$(D^o, A_N^o) - LO$
D	1.498	DAP
E	1.471	BE @ defect center
F	1.453	$BE - LO$
	1.020	Si cluster PL

Table 5.2: Notation, position, and assignments for the emission lines in the PL spectra of the CdTe/GaAs:Si heterostructure.

require the presence of the heterojunction interface. The most notable and pronounced of these structures is the strong peak centered at 2.549 eV in Fig. 5.1 (c). This emission, ascribed to transitions occurring in the CdTe epilayer between Γ_6 conduction band states and Γ_7 spin-orbit split-off valence states, is in excellent agreement with CdTe $\Gamma_6 - \Gamma_7$ transitions reported at 2.538 eV and 2.546 eV by Feng [112] and Olego [130], respectively. As the PL signals from these transitions are usually very weak, investigations of energy gaps other than that of the fundamental E_o gap, usually require the use of modulation-based spectroscopic techniques. In fact, prior to the work of Feng *et al.* [112], the CdTe $\Gamma_6 - \Gamma_7$ gap had only been seen, using conventional PL techniques, in HgTe-CdTe superlattices [130] where carrier confinement increased the concentration of Γ_7 holes in the CdTe layers so the $\Gamma_6 - \Gamma_7$ transition was strengthened. Feng and co-workers, studying PLEE grown CdTe/GaAs heterostructures, were still able to observe this higher gap emission even though holes in their films were not confined to the Γ_7 states. They attributed their unusual observation of the $E_o + \Delta_o$ PL band to the high crystalline quality of the samples they investigated, in conjunction with the employment of sensitive OMA detection techniques. As this earlier study was primarily concerned with outgoing multi-phonon resonant Raman scattering in the CdTe samples, the energy region investigated did not extend further than about $1,600$ cm^{-1} from the exciting laser line. As a result, additional structure present in and below the CdTe and GaAs $E_o + \Delta_o$ gap regions was not revealed. It should also noted that the $E_o + \Delta_o$ PL recombination observed from the CdTe/GaAs:Si heterostructure investigated in this study was only $10^{-1} - 10^{-2}$ times weaker than the recombination across

the E_o gap. This is $10^3 - 10^4$ times stronger than that recorded in Refs. [112, 130] and it is felt that higher carrier concentrations and or impurity levels in this sample may be responsible for the increased luminescence intensity.

Another significant feature associated with the CdTe $E_o + \Delta_o$ gap region in Fig. 5.1 (c), is the broad luminescence emission centered at 2.360 eV. This feature is significantly wider (a factor of five) then the 2.549 eV structure. If one subtracts the CdTe split-off energy Δ_o = 920 meV [131] from the 2.360 eV luminescence, the resulting difference is 1.44 eV. Taking into consideration both this energy difference and the strong intensity of the defect related 1.47 eV emission in both the target and heterojunction spectra of Figs. 5.1 (b) and (c), it is proposed that the 2.360 eV luminescence is the result of electrons bound to the defect center responsible for the 1.47 eV luminescence recombining with holes in Γ_7 valence states. It is believed that this is the first observation, using conventional PL methods, of luminescence structure other than band to band recombination itself, associated with the $E_o + \Delta_o$ gap in CdTe.

The final significant feature in Fig. 5.1 (c) is that of the broad peak in the 1.66 to 1.88 eV range. This structure has no counterpart in the spectrum of Target-A and is attributed to $E_o+\Delta_o$ luminescence from the GaAs substrate since it occurs at the correct energy and would be enhanced in a manner similar to that of the epilayer. Both this signal and that of the CdTe $E_o + \Delta_o$ gap are much weaker than that of the epilayer due to above-gap absorption in the CdTe epilayer for energies in this range.

An interesting and important aspect of the heterojunction spectrum is the breadth of the energy range which must be scanned (460 to 660 nm) in order to cover the entire PL structure. As seen in Fig. 5.1 ((a) & (b)) and as noted during the Raman studies mentioned earlier [112, 113] the CdTe $E_o+\Delta_o$ PL is not present in the component spectra of the heterojunction and only occurs once the interface is formed. Because the enhancement is so strong and the structure so spread out in energy for higher gaps in particular, it appears that contributions from this type of effect should be considered carefully during heterostructure engineering.

(111)CdTe/(001)InSb heterostructure

Figure 5.3 (a) shows the PL produced by CdTe Target-B. The spectrum exhibits strong phonon replicas and is considerably different from the spectrum of Target-A. Again

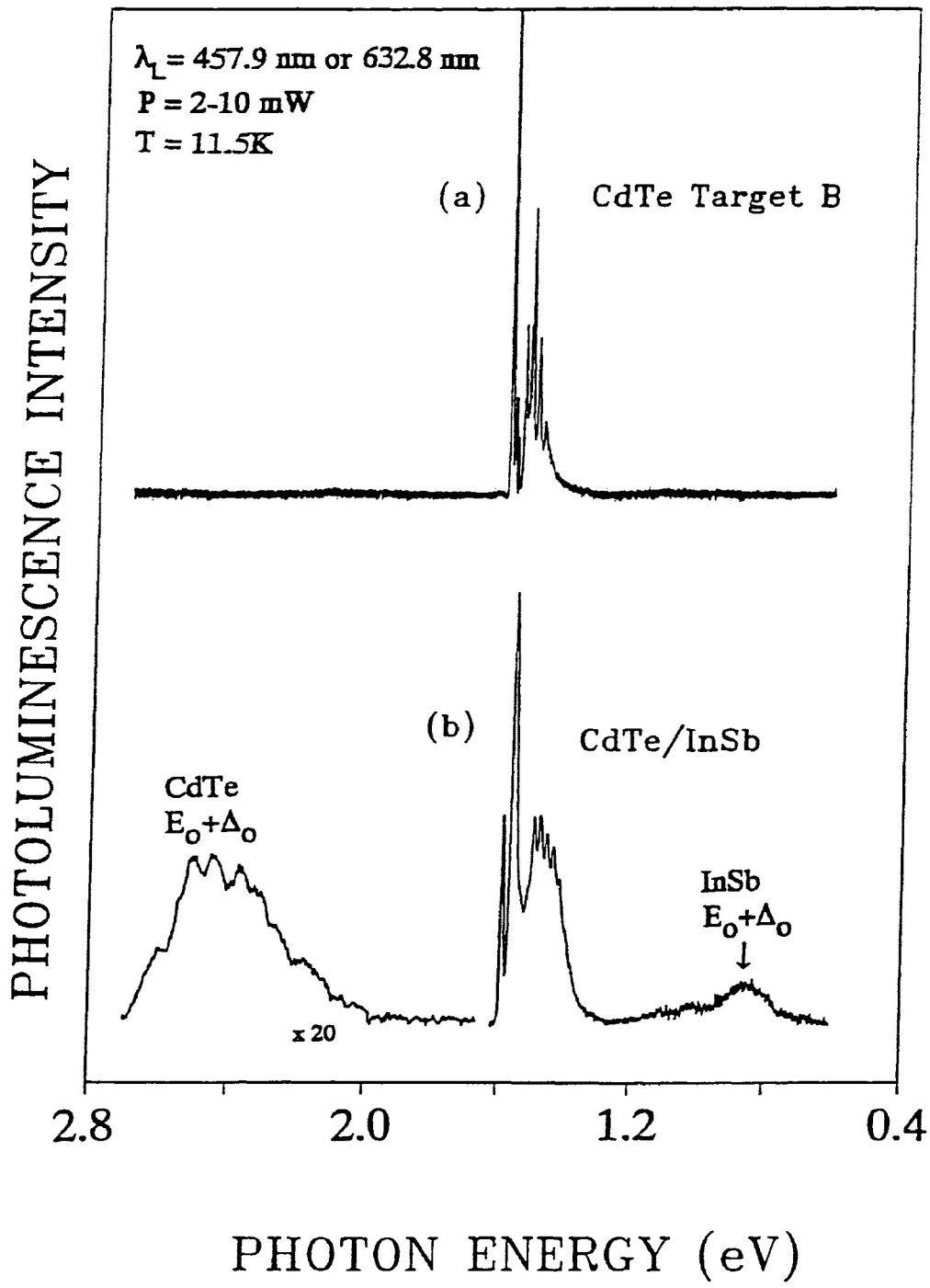

Figure 5.3: PL spectra of (a) the CdTe ablation source material (Target-B) and (b) a (001)CdTe/(001) InSb heterojunction with 0.96 um thick epilayer. The InSb substrate alone showed no disernable PL.

there is no measurable photoluminescence signal near the CdTe $E_o+\Delta_o$ gap energy. Figure 5.3 (b) is a spectrum obtained after ablation of this target and PLEE growth on an InSb substrate. The epilayer CdTe E_o and $E_o+\Delta_o$ regions show excitonic and phonon replica structure quite similar to that of the E_o region of the target material. Just as the PL from the substrate GaAs $E_o+\Delta_o$ region was discernible in Fig. 5.1 (c), there is a significant luminescence starting at an energy of 0.86 eV, which is the threshold energy of the InSb $E_o+\Delta_o$ gap. This was not discernible in the PL from the (001)InSb substrate alone.

The use of double [130] or triple spectrometers ([112] and this work) with their excellent stray light rejection, along with photon counting detection sensitivity may be a critical factor when searching for low intensity PL luminescence at higher gap energies. When the structure of interest is spread out over such a large wavelength range and the signal is so weak, the PL method tends to preserve relative intensity information better than a derivative (modulation spectroscopy) technique. In this study, recombination from a transition associated with the CdTe spin-orbit, split-off band, other than the direct $\Gamma_6 - \Gamma_7$ transition, has been observed for the first time.

The enhanced PL signals associated with the $E_o+\Delta_o$ regions of the film and substrate materials seen once the heterojunction is produced underscores the importance of the interface. At least in the case of these mixed II-VI/III-V heterostructures, it appears that interface states produced by differences in species valence, along with high carrier concentrations and or impurity levels in the samples, are sufficiently long lived to promote radiative decay across higher gaps. If this is so, then heterostructures developed for optoelectronic transduction should be carefully checked for radiative decay across these higher gap channels since any such decay mechanisms reduce the effective carrier generation efficiency.

5.2 (111)$Cd_{1-x}Mn_xTe$/(111)GaAs:Si heterojunctions

5.2.1 Introduction

In recent years, diluted magnetic semiconductors (DMS), also known as semimagnetic semiconductors (SMSC), have attracted interest in both the scientific and industrial communities. These materials have some unique properties which enhance their potential for use in a wide range of opto-electronic devices. DMS are semiconductors with a fraction of their constituent ions replaced by transition metal ions (i.e. Mn, Fe or Co).

The band gap and lattice parameters of these materials can be altered by changing the concentration of the magnetic ions appropriately. The possibility for band gap engineering in these materials makes them useful for a variety of device applications. The tunability of the lattice parameter with magnetic ion content also extends their utility into the field of heterostructures where lattice matching is important.

The presence of strong paramagnetic ions in the DMS results in magnetic properties which distinguish them from ordinary semiconductors. In contrast to normal semiconductors, the magnetic ions in DMS respond to an external applied magnetic field by changing their energy band and impurity level parameters. A unique and important feature of DMS is the spin-spin exchange interaction which occurs between the localized magnetic moments of the paramagnetic ions and the charge carriers. This interaction affects the energy band, electronic structure and impurity level parameters of the semiconductors resulting in new physical effects, particularly when the correlation effects are strong. The consequences, reviewed in Refs. [8, 132, 133], can be quite dramatic: g-factors may be effectively enhanced by as much as two orders of magnitude, Faraday rotations can become very large and the magneto-resistance can become negative, reaching exceptionally large values and leading to an insulator to metal transition induced by increasing the magnetic field.

The most commonly and extensively studied DMS are those in which Mn^{2+} ions are introduced into II-VI compound semiconductors. These are the DMS which can accommodate the highest possible magnetic ion concentration without the crystallographic quality and structure of the host materials being destroyed. As a result, these materials have the potential to be used in a wide variety of device applications [134, 135, 136, 137, 138].

A strong enhancement of $E_o+\Delta_o$ photoluminescence was seen in the study of II-VI CdTe deposited on the III-V materials InSb and GaAs presented in the previous section. This PL enhancement near the $E_o+\Delta_o$ energy was observed for both the substrate and epilayer and was attributed to effects arising from differences in the surface states of the epilayer and substrate in the region of reconstruction. Also in the previous section, evidence for Si clustering in the substrate was found in the combined PL spectrum of the CdTe epilayer deposited on the GaAs:Si. This was of interest because Suezawa *et al.* [119], in a study of the Si clustering in silicon doped GaAs showed that the cluster PL changed from a single broad peak to a double peak emission when the annealing temperature was raised above approximately 550°C.

It has been shown [139, 140] that when heteroepitaxy occurs between either materials with group IV diamond structure and groups III-V zinc-blende structure or between groups II-VI and III-V zinc-blende structures, an ideal planar geometry is not allowed when each atom bond does not contain its full complement of two electrons at the interface. For example, in the case of II-VI/III-V (100) or (111) heteroepitaxy of (Cd,Mn)Te on GaAs, this involves either abutting an As-terminated GaAs surface to a CdMn-terminated (Cd,Mn)Te surface, or a Ga terminated GaAs surface to a Te-terminated (Cd,Mn)Te surface. In the first case, the interface atoms would be ideally composed of 7/4 electron bonds while in the latter case, there would be 9/4 electron bonds. Such structures produce charge accumulation at the interface resulting in compensatory processes which have the effect of destroying the ideal planar nature of the interface.

Such processes could include electric field enhanced diffusion, electric field enhanced desorption or possibly valence state changes in multivalent elements like Mn. When lattice mismatch is added as an additional parameter, the net reconstruction occurring in the first layers of epitaxial growth for such cases is difficult to predict. While the effects of the substrate on the properties of the epilayer are often difficult to fully determine, systems which have this change in valence at the interface (i.e. II-VI/III-V) deserve additional attention because of the interface surface state effects which may result.

In this section, the PL enhancement at the GaAs substrate $E_o+\Delta_o$ gap induced by the presence of the interface is further investigated by presenting the results of an earlier study [141] of the PL produced by a series of $Cd_{1-x}Mn_xTe$ (CMT) epilayers on (111)GaAs:Si for manganese mole fraction in the range $0.44 < x < 0.69$ and epilayer growth temperatures from 210°C to 290°C. At the same time, information about the interface growth dynamics associated with the PLEE process is obtained from the substrate Si cluster photoluminescence.

5.2.2 Experiment

The $Cd_{1-x}Mn_xTe$ samples studied in this work were also produced using the PLEE technique. Many high quality $Cd_{1-x}Mn_xTe$ heterojunctions have been produced using this method [85, 111, 114, 115, 116]. The system used has been described elsewhere [111, 138] but in brief, to grow CMT layers of varying Mn fraction, two separate lasers and two targets were used. A XeCl laser operating at 308 nm with a pulse width of 30 ns and triggered

Sample	Substrate temp. (°C)	Thichness (μm)	Composition (x)
CMT-600	210	0.8	0.69
CMT-605	250	0.6	0.54
CMT-606	270	1.4	0.52
CMT-610	290	1.8	0.44

Table 5.3: Properties of PLEE-grown $Cd_{1-x}Mn_xTe$/GaAs heterostructues.

at rates up to 80 Hz vaporized the CMT target (x = 0.56). At the same time, a Nd:YAG laser operating at 1.06 μm, with a pulse width of 90 ns and triggered at 0.5 - 1.0 kHz, vaporized a Cd pellet to generate a variable Cd over pressure in the growth chamber. This over pressure was varied to change the Cd to Mn ratio in the samples in order to investigate the feasibility of using this method for epitaxial growth of $Cd_{1-x}Mn_xTe$ in the zinc blende crystal structure over a sizeable range of Mn composition. The adjustable frequencies of the pulse triggers, peak energies of the lasers and substrate temperatures determined the growth conditions. The average growth rate was 0.8 - 1.2 μm/hr, so the film thicknesses (which varied from 0.6-1.8 μm) required proportionate growth times.

The parameters of the CMT films are presented in Table 5.3. The films were deposited on the polished As face of a high quality (111)-oriented Si-doped GaAs (Sumitomo Electric, Inc.) wafer. The wafers were degreased in chloroform, acetone and isopropyl alcohol and etched in a solution of H_2SO_4:H_2O:$2H_2O$ (7:1:1). The substrates were mounted with high purity In on a Mo block and prior to growth they were thermally treated at 580°C for ~2 min. This treatment led to an oxide free GaAs surface. Film thickness was monitored during growth. Raman analysis was used to obtain the Mn composition (x) for each film.

The photoluminescence signal was excited with various lines of an Ar^+ ion or HeNe laser. Each beam was focused to a line image about 0.2 mm × 3.0 mm using crossed cylindrical lenses. The visible and NIR photoluminescence was analyzed using the Jobin-Yvon S-3000 triple spectrometer and Hamamatsu R943-02 photon counting PMT outlined earlier. The slit settings in the system corresponded to about 3 cm^{-1} resolution. Overlapping spectra from the NIR to MIR were taken using the Bomem MB-155 FTIR spectrometer with the liquid nitrogen cooled InSb detector. The FTIR resolution was 2 cm^{-1}. The PL measurements were carried out in the 90°-scattering geometry. The samples were cooled to 11.5 K with the CTI closed cycle helium refrigerator as previously described.

5.2.3 Results

GaAs:Si heat treatment:

Figure 5.4 shows the photoluminescence spectra from a portion of the Si-doped (111)GaAs substrate. Figure 5.4 (a) is the result before heat treatment, (b) after one hour of vacuum annealing at 400°C, (c) after an additional hour at 500°C and (d) after a further 2 hours at 600°C. The GaAs is heavily doped with Si (2×10^{18}cm^{-3}) and exhibits broad unresolvable excitonic structure in the E_o gap region from 1.52 - 1.30 eV, along with a strong luminescence feature centered at 1.2 eV, previously attributed to the formation of Si clusters by Suezawa *et al.* [119]. The spectrum in Fig. 5.4 (b) is quite similar to that of the unannealed substrate material and differs only in the ratio of the gap-edge to Si cluster single peak intensities. The spectra in Figs. 5.4 (c) and (d) display an additional, relatively broad PL peak at approximately 1.0 eV which only appears after the anneal at 500°C.

During their work, Suezawa and coworkers, combined a 20 hour high temperature "homogenizing" anneal (under an As overpressure) with subsequent lower temperature isothermal anneals to develop the Si clusters. They observed that the 1.0 eV peak was considerably enhanced after an anneal at 600°C which is quite close to the 500°C result observed in this work. From IR absorption analysis, they infer that this peak is due to the added presence of another type of clustering associated with a change in bonding within the Si sub-system.

Figure 5.4 (d) shows the end result of extended high temperature vacuum treatment on the substrate material. It is included to show that while the GaAs signal has disappeared, the Si cluster effects are still strong. The elimination of the GaAs E_o peak may be due to a combination of different processes. It has been reported that vacuum heat treatment of GaAs in the absence of an As overpressure results in degradation of the surface due to the loss of arsenic [103, 142]. Also a SIMS study of CdTe layers grown by PLEE on GaAs [143] showed intensive migration of Ga to the surface of the epilayer. In order to duplicate the vacuum growth conditions during epitaxy, no attempt was made to reduce the loss of either element during the annealing treatment. It is likely that progressive evaporation of one or both of these elements, particularly at the higher anneal temperatures, is responsible for the missing GaAs gap-edge PL. It is clear, however, from the spectrum of Fig. 5.4 (c) and reference [119] that the occurrence of the Si peak at 1.0 eV is an indication that the substrate has been subjected to an 'effective temperature' of 500°C or greater

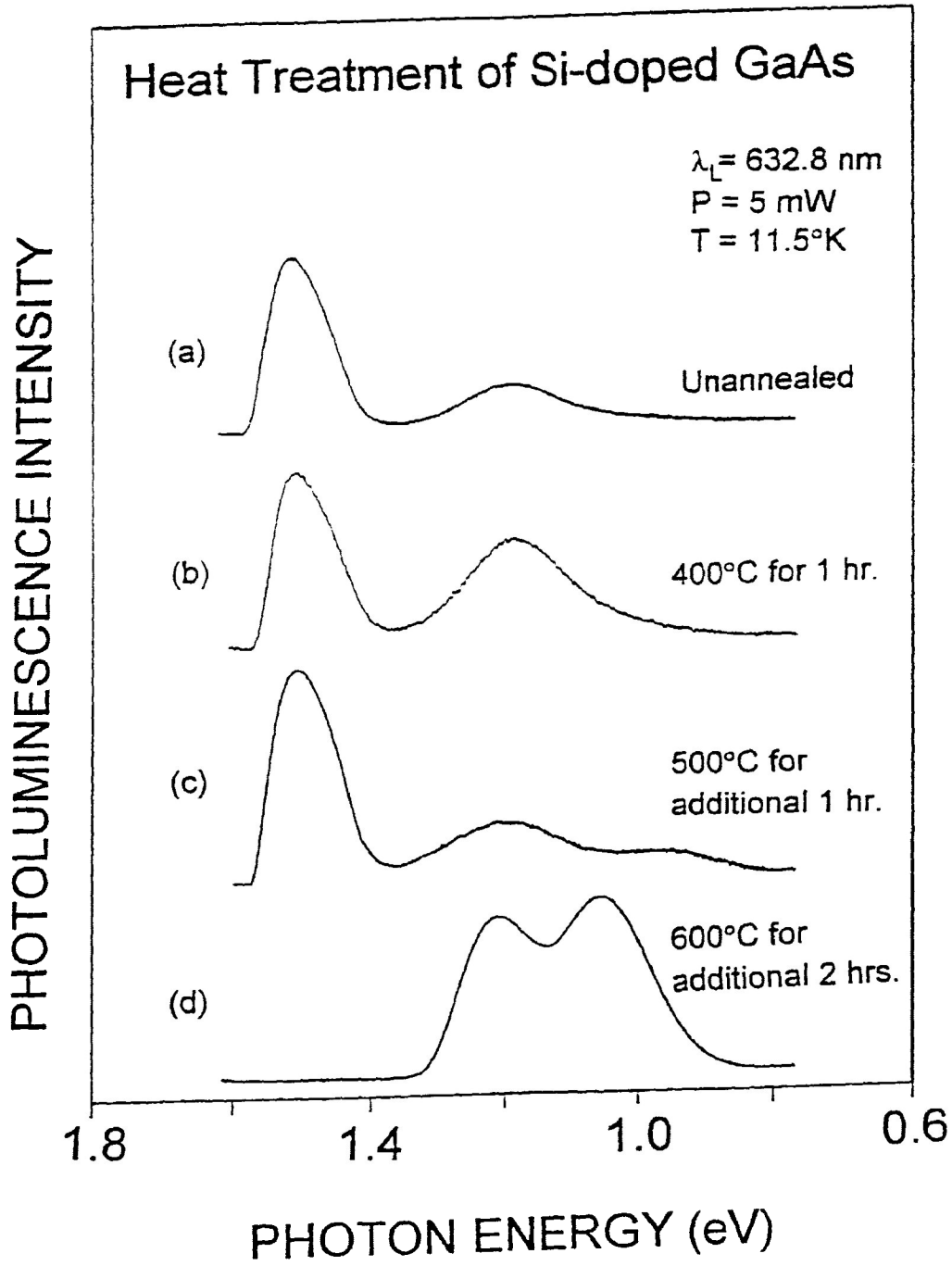

Figure 5.4: PL spectra from a portion of the Si-doped (111) GaAs substrate: (a) is the result before heat treatment, (b) after one hour of vacuum annealing at 400 C, (c) after an additional hour at 500 C, (d) after a further 2 h at 600 C.

during the PLEE growth.

$Cd_{1-x}Mn_xTe$ epilayers on (111)GaAs:

Figure 5.5 shows a series of spectra identified by the Mn fraction x for $Cd_{1-x}Mn_xTe$ epilayers grown on the GaAs at different substrate temperatures. The dominant features in the high energy portion of the spectra are the Mn^{2+} concentration dependent and well studied, bound magnetic polaron (BMP) and the approximately 2.0 eV manganese luminescence [144, 145, 146].

All of the $Cd_{1-x}Mn_xTe$/GaAs spectra in Fig. 5.5 clearly exhibit both the GaAs substrate E_o region excitonic structure near 1.52 eV and the ~1.2 eV Si cluster PL. On close examination of this figure it becomes apparent that the GaAs E_o peak decreases in width and is shifted to slightly lower energy when the growth temperature increases. It is likely that these changes are due to a loss of carriers in the E_o gap region to competing processes resulting in a reduced Burstein-Moss shift [147]. The heterojunction spectra of Fig. 5.5 also exhibit varying degrees of PL signal in the region of the GaAs $E_o+\Delta_o$ band gap at 1.86 eV [148]. This PL is not discernible in the spectrum of the substrate when studied alone so its occurrence appears to be dependent on the presence of the interface. The intensity of this peak is seen to vary from being virtually negligible in the spectrum with $x = 0.69$ (grown at 210°C) to being comparable in size to that of the Mn^{2+} PL peak in the spectrum with $x = 0.44$ (grown at 290°C). Several parameters are changing in this alloy group as one moves from the $x = 0.69$ to $x = 0.44$ spectra in Fig. 5.5. The lattice mismatch between epilayer and substrate increases by approximately 1% as the Mn fraction decreases and the epilayer thickness increases with growth temperature (Table 5.3). Due to the increased inherent anneal at higher growth temperature, the interface reconstruction will be affected. Raman results for these samples [85] showed stronger phonon signatures for the epilayers grown at higher temperature and it was concluded that they were the better samples in the group. Thus, the increase in the GaAs substrate $E_o+\Delta_o$ recombination PL reported here, for the same alloy sequence, may be a consequence of enhancement in carrier diffusion lengths which allow carriers (electrons, holes and excitons) generated in the epilayer to penetrate to the interface region before radiatively recombining.

While not distinguishable in the spectrum of the unannealed GaAs substrate or the heterojunction grown at 210°C, the 1.0 eV Si cluster peak appears in all spectra grown at

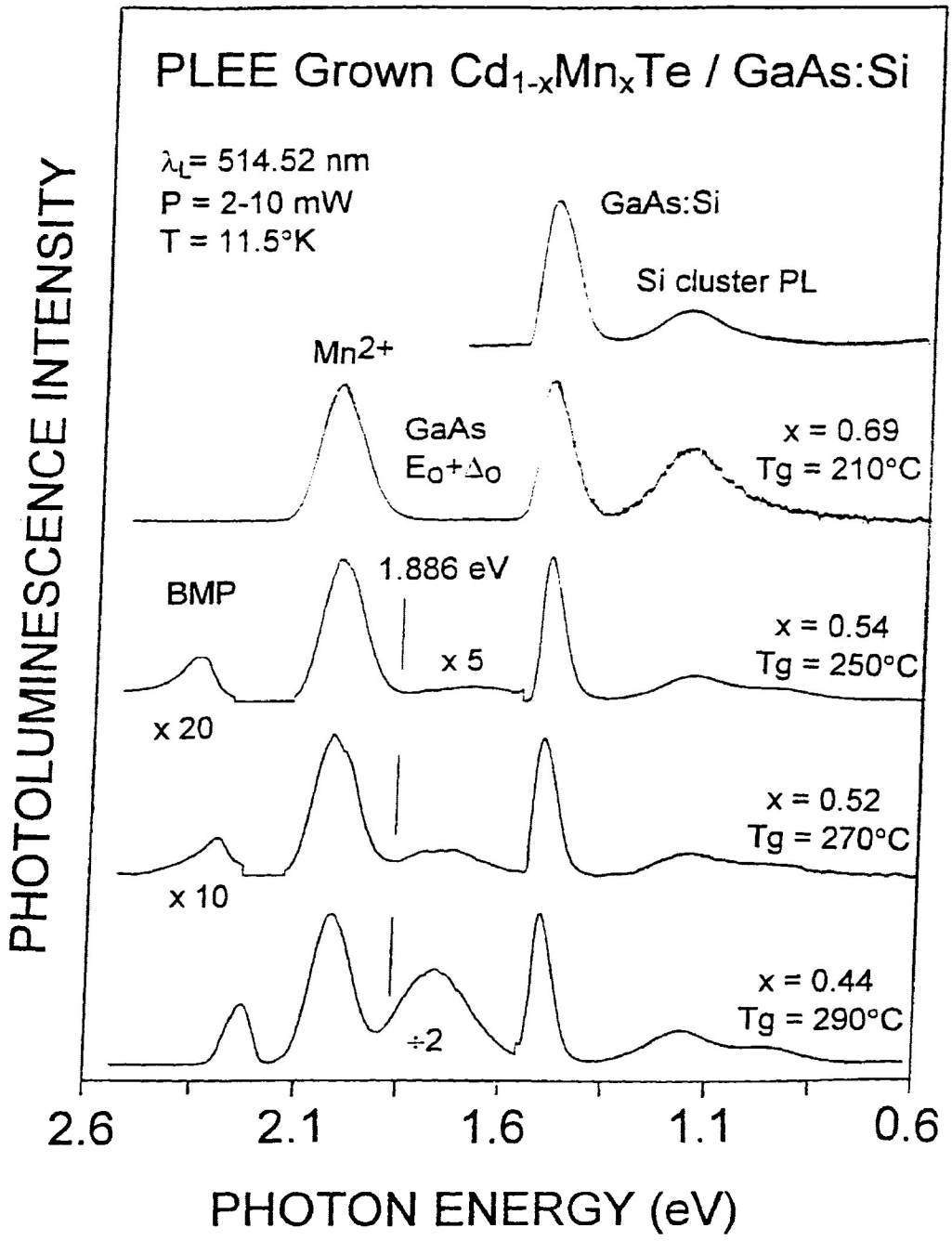

Figure 5.5: PL from a series of spectra identified by the Mn fraction (x) and substrate temperature during growth (Tg) for CdMnTe epilayers grown on the GaAs. Epilayer thicknesses are listed in Table 5.3.

or above $T_g = 250°C$. Once this peak is established, its intensity changes only slightly as the growth temperature and time are increased. This is in contrast to the intensity of the GaAs $E_o+\Delta_o$ peak, which also first appears in the 250°C spectrum. Since the 1.0 eV PL is produced as a consequence of Si migration in the substrate only, while the $E_o+\Delta_o$ luminescence may be the result of carriers generated both in the epilayer and substrate, the difference in the dependencies appears to be reasonable.

Although the substrates were heated to 580°C for up to 2 minutes to remove oxides before the growth was initiated, based on the annealing study presented above and the absence of the 1.0 eV peak in the $T_g = 210°C$ spectrum of Fig. 5.5, it is unlikely that this amount of heat treatment would provide sufficient time for the second Si cluster type to form. The 1.0 eV Si peak in the lower spectra of Fig. 5.5 is almost identical to that of spectrum (c) in Fig. 5.4, after the additional anneal at 500°C for 1 hr. The energy necessary to facilitate this process is likely derived from thermal heating of the substrate during the growth process in combination with a significant contribution from the impinging particles produced by the laser ablation. It is concluded that the kinetic component can substantially assist in surface diffusion as it appears to raise the effective substrate surface temperature above the measured supporting block temperature.

5.3 $In_{1-x-y}Ga_xAl_yAs$ heterostructures lattice-matched to InP

5.3.1 Introduction

Semiconductor lasers and erbium-doped fiber lasers operating at 1.30 and 1.55 μm are the key sources for low-loss fiber optic communication systems. During the last decade most efforts in this area of research have concentrated on quantum well (QW) lasers based on the $In_{1-x}Ga_xAs_{1-y}P_y$ system, lattice-matched to InP. An alternative material which can also be grown lattice-matched to InP is $In_{1-x-y}Ga_xAl_yAs$, with $(x + y = 0.47)$ [149]. This quaternary covers essentially the same wavelength range as the $In_{1-x}Ga_xAs_{1-y}P_y$ system and has only recently been considered a serious challenger for optoelectronic communications applications [9, 150, 151]. Several devices based on this material system have already proven of interest in high-performance microelectronics [152] and appear to offer several advantages over their $In_{1-x}Ga_xAs_{1-y}P_y$ counterparts.

Some results of recent measurements (summarized in Ref. [153]) on these two

quaternary systems are compared in Table 5.4. The electron and hole effective masses vary linearly with composition, and are very similar in both cases. The band gaps and refractive indices are also alike. The major difference between these two systems lies in the size and variability of the band offsets that can be generated. In the $In_{1-x}Ga_xAs_{1-y}P_y/InP$ system, the largest possible conduction band offset (ΔE_c) that can be produced results from the growth of $Ga_{0.47}In_{0.53}As$ on InP. When Al replaces P in this quaternary mix, the ΔE_c value can be effectively doubled with growth of the bi-ternary heterostructure, $Ga_{0.47}In_{0.53}As/Al_{0.48}In_{0.52}As$, lattice-matched to InP. From the data presented in Table 5.4, it can be established that the ratio's between the conduction band offsets and the band gap differences in these systems are 40% and 75%, respectively. In principle, this difference favours the Al-based system for laser and quantum modulator applications. Specific advantages of the InGaAlAs/InP system over its InGaAsP/InP counterpart include:

1. It has been shown [154] that for symmetric wave functions in QW's corresponding to the first, third, and fifth, etc. electron energy levels, E_e, solutions are given by

$$\tan\left(\frac{L}{2}\sqrt{\frac{8\pi^2 m_e^*(w)E_e}{h^2}}\right) = \left(\frac{m_e^*(w)}{m_e^*(b)}\right)^{\frac{1}{2}}\sqrt{\frac{\Delta E_c - E_e}{E_e}} \tag{5.1}$$

where $m_e^*(w)$ is the electron effective mass in the well material, $m_e^*(b)$ is the electron effective mass in the barrier and L is the well width. Similarly, for antisymmetric wave functions corresponding to the second, fourth, and sixth, etc. energy levels

$$\cot\frac{L}{2}\left(\sqrt{\frac{8\pi^2 m_e^*(w)E_e}{h^2}}\right) = \left(\frac{m_e^*(w)}{m_e^*(b)}\right)^{\frac{1}{2}}\sqrt{\frac{\Delta E_c - E_e}{E_e}} \tag{5.2}$$

Calculations of the hole energy levels, E_h, in the valence band yield similar relationships. Since larger values of ΔE_c are possible in the Al-based quaternary system, then correspondingly wider well widths can be used for given values of E_e and E_h. This results in larger carrier confinement factors [155] and more effective photon generation in QW lasers based on this material system.

2. The larger values of ΔE_c attainable in InGaAlAs based heterostructures results in better confinement of the free electron gas in QW's. This leads to higher optical gains per well by reducing the gain broadening resulting from coupling between electron levels in neighboring wells, and by reducing the electron spill-out from the wells into the optical guiding region at high carrier injection levels.

Properties	GaInAsP	AlGaInAs
Bandgaps (300 K)	0.75 - 1.34 eV	0.75 - 1.45 eV
m_c/m_e	0.041 - 0.08	0.041 - 0.083
m_v/m_e	0.47 - 0.85	0.47 - 0.87
μ (cm^2/Vs)	13000 - 6000	13000 - 4600
Offsets (ΔE_c)	269 meV	525 meV
Schottky barrier	on InP: 0.43	on AlInAs: 0.77 - 0.85
Refractive indices	3.58 - 3.17	3.58 - 3.21

Table 5.4: Data for GaInAsP and InGaAlAs heterostructures lattice-matched to InP.

3. With respect to quantum modulator applications, it has been shown [156] that in the presence of an external electric field, the energy shift of the exciton ground state level in an isolated QW is proportional to the fourth power of the well width. Hence, efficient modulation requires relatively thick wells and this again favours the InGaAlAs system.

4. The lower ΔE_v in InGaAlAs, as compared to InGaAsP, provides a major advantage for high-frequency modulator operation since the holes can easily tunnel through the lower barriers. Under polarization, their sweeping out by the electric field should not limit the band-width of modulators based upon this system. For the same reason, the applied electric field will not be screened by hole pile-up in the wells. Thus, the modulation contrast should not decrease at a high-input optical intensities.

5. Another important advantage of the InGaAlAs system is that its does not suffer from the difficult As/P ratio control problem encountered in the growth of InGaAsP using conventional molecular beam epitaxy (MBE) systems.

From the discussions above, it appears that the InGaAlAs/InP system is a very good candidate for the production of both electronic and optoelectronic devices. Although many of the properties associated with this alloy have been previously reported [153], ongoing controversy over some of the most fundamental of these characteristics has continued. Most notably, PL investigations undertaken by three groups (Refs. [151, 157, 158]) have yielded a linear relationship between the band gap energy of $In_{1-x-y}Ga_xAl_yAs$ and Al composition y, while studies by two others (Refs. [9, 159]), report parabolic relationships. The departure from linearity in the latter two cases was significant and could not be explained by experimental uncertainties.

In this report the compositional dependence of the $In_{1-x-y}Ga_xAl_yAs$ band gap is further investigated using low temperature PL, with emphasis placed on the $0 < y < 0.07$ range. Results of this study indicate that contrary to earlier findings [150, 157], high quality InGaAlAs/InP heterostructures can be produced using conventional MBE techniques. Line widths associated with the gap-edge PL emissions are determined and found comparable to the best published data for MBE, MOVPE and MOCVD grown materials. As well, Raman results presented in this work comprise, what is believed to be, one of the first such investigations of the phonon modes in this novel material system.

5.3.2 Experiment

The MBE method of film growth, recently reviewed in Refs. [160, 161, 162], is a widely employed technique used in the production of a variety of high-quality thin-films materials. The $In_{1-x-y}Ga_xAl_yAs$/InP heterostructures studied in this report were grown using a modified V80H MBE system at NRC's Institute for Microstructural Sciences. Details of the growth process are given elsewhere [163], but briefly, the $In_{1-x-y}Ga_xAl_yAs$ epilayers were grown on either semi-insulating InP:Fe or heavily S-doped (10^{18}) InP substrates. The arsenic dimer As_2 was used as the group V element and was generated with a solid source valved arsenic cracker cell with the tantalum/rhenium cracking zone kept at 950° C (better than 90% cracking efficiency). The arsenic overpressure used was about twice the level necessary to sustain As-stabilized reconstruction for InGaAs or InAlAs layers. The group-III elements were supplied from the appropriate melts of ultrahigh purity elements using modified solid source effusion cells.

The specific compositional construction of the samples investigated are summarized in Table 5.5. Growth rates for the films produced were between $2.4 - 2.7$ Å/s. In all cases, conditions were such that no re-evaporation of the group-III elements from the growth surface occurred. Hence, the growth rate of the InGaAlAs was the sum of the growth rates for the GaAs, AlAs, and InAs components. The growth rates and compositions for the InGaAs and InAlAs films were first estimated from the ongoing growth rate calibrations and later confirmed by x-ray double crystal rocking curve measurements. In the case of the InGaAlAs epilayers, these quantities were estimated from the ongoing calibrations and the molecular flux measurements of the group-III fluxes immediately prior to the growth (this is accomplished by placing a vacuum ion gauge in the wafer position).

Sample	Film	Substrate	Cap
1492	$In_{0.512}Ga_{0.488}As$	InP:S doped to (10^{18})	n/a
1510	$In_{0.541}Ga_{0.459}As$	InP:S doped to (10^{18})	n/a
1545	$In_{0.53}Ga_{0.44}Al_{0.03}As$	InP:Fe semi-insulating	n/a
1471	$In_{0.53}Ga_{0.42}Al_{0.05}As$	InP:S doped to (10^{18})	50Å $In_{0.53}Ga_{0.47}As$
1514	$In_{0.53}Ga_{0.40}Al_{0.07}As$	InP:Fe semi-insulating	50Å $In_{0.53}Ga_{0.47}As$
1515	$In_{0.53}Ga_{0.40}Al_{0.07}As$	InP:Fe semi-insulating	50Å $In_{0.53}Ga_{0.47}As$
1511	$In_{0.507}Al_{0.493}As$	InP:S doped to (10^{18})	n/a
1493	$In_{0.52}Al_{0.48}As$	InP:S doped to (10^{18})	n/a

Table 5.5: Compositional construction of $In_{1-x-y}Ga_xAl_yAs$/InP heterostructures.

Mirror smooth morphology and layer thickness uniformity of better than 1% over the entire 2 inch wafers was achieved in all cases. For wafers grown at or above 400° C, the temperature of the films was measured using infrared pyrometry. The pyrometer was calibrated against the melting point of InSb. For samples grown at lower temperatures, readings from a thermocouple mounted behind the wafer holder were used to estimate the growth temperature. Such readings are usually 50 to 100° C higher than the actual growth temperature, but can be corrected using the extrapolation of this temperature difference from the higher temperatures where the pyrometer still yields reliable readings. All of the layers listed in Table 5.5 (with the exception of samples #1543 and #1515) were produced at 490 – 500° C. The growth of samples #1543 and #1515 was carried out at 300° C.

The PL signal was measured at 11.4 K over the 1.6 to 0.6 eV range using the Bomem MB-155 FTIR instrument in combination with a LN_2-cooled, InSb detector. The FTIR resolution was set at 2 cm^{-1} and approximately 10 mW of the 514.5 nm Ar^+ ion laser line was used for sample excitation. The Raman signal was recorded at 300 K using the Instruments SA triple-spectrometer and Princeton Instruments CCD array detector as described in Section 4.1.2. Approximately 80 mW of the 488.0 nm Ar^+ ion laser line was used for sample excitation. The beam was typically focused to a line image of approximately 0.2 mm × 3.0 mm using crossed cylindrical lenses to reduce the power density at the sample. The measurements were carried out in the 90°-scattering geometry in both the PL and Raman investigations.

5.3.3 Photoluminescence Results

Figure 5.6 shows the PL spectra of four $In_{1-x-y}Ga_xAl_yAs/InP$ heterostructures with y values ranging from $0-7\%$. With the exception of the result in (c), the emission spectra of the samples consist mainly of a strong, well-defined gap-edge peak along with a weaker, lower energy contribution. In the case of the $In_{0.541}Ga_{0.459}As/InP$ spectrum, presented in Fig. 5.6 (a), these two peaks occur at 0.795 and 0.768 eV, respectively. The 0.795 eV emission, with a line width of 7.7 meV, is very similar to a BE peak (@ 0.802 eV with FWHM $\simeq$ 5 meV) identified in $In_{542}Ga_{458}As/InP$ grown by vapour phase epitaxy (VPE) [164]. The predicted spectral positions of several near-band-gap emission lines in $In_{0.53}Ga_{0.47}As$ were calculated in Ref. [164] and the results indicated that recombination luminescence due to (FE), (D^o,X), (D^+,X), (A^o,X), and (D^o,h) transitions would all lie in a 3 meV wide band, approximately 3.5 meV below the gap edge. Any of these transitions occurring in the InGaAs spectrum of Fig. 5.6 (a) would lie under the 0.795 eV emission and hence, this peak is likely the result of a combination of such processes. The weaker 0.768 eV emission in the spectrum lies precisely at the same position as a donor-acceptor pair (D^o,A^o_{Si}) transition, identified in VPE grown InGaAs by Macrander and Swaminathan [165], and is tentatively attributed as arising via this mechanism.

The PL spectrum of the $In_{0.53}Ga_{0.44}Al_{0.03}As/InP$ heterostructure, illustrated in Fig. 5.6 (b), is very similar to that considered in Fig. 5.6 (a). As the Al concentration, y, has increased from 0 to 3%, in going from the film represented in (a) to that in (b), the band gap energy of the material has increased accordingly. It is noted that the both the 0.841 and 0.811 eV peaks in Fig. 5.6 (b) appear shifted by $\approx$ 45 meV relative to the corresponding peaks at 0.795 and 0.768 eV in the spectrum of Fig. 5.6 (a). Based on this observation, and the fact that the line widths and relative intensities of the pairs of peaks are alike, it is argued that the mechanisms responsible for the PL transitions determined in (a) are fundamentally the same as those generating the luminescence spectrum in (b).

The PL from the $In_{0.53}Ga_{0.42}Al_{0.05}As/InP$ heterostructure, illustrated in Fig. 5.6 (c), is notably different than that presented for the previous two films. The high energy component of the spectrum at 0.885 eV is not the dominant radiative decay mechanism, and both the intensity and line width associated with the lower energy peak at 0.820 eV are considerably enhanced. In addition, a third weak emission, located 21 meV below the 0.885 eV peak, is also detected. The presence of the broad, highly luminescent structure

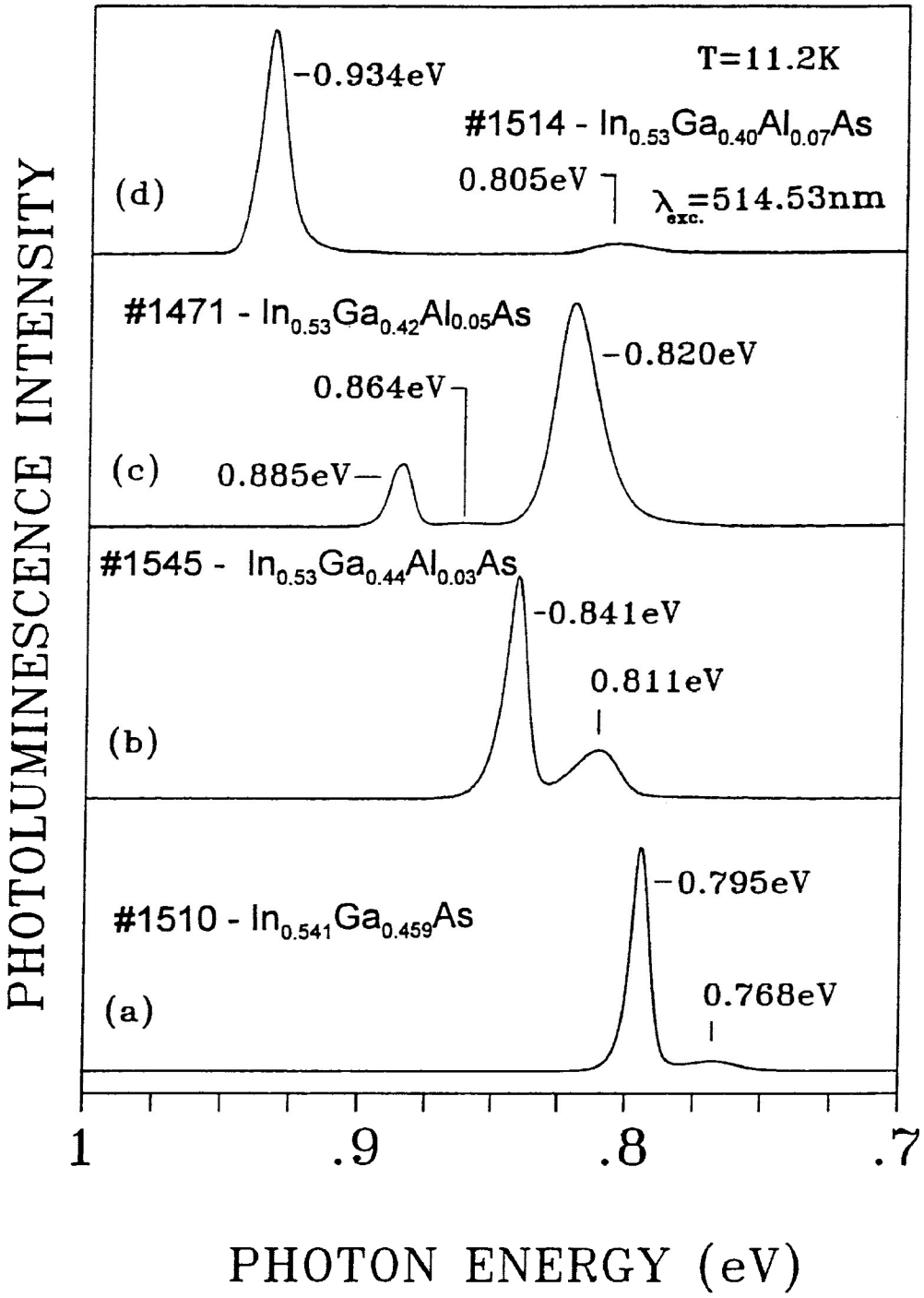

Figure 5.6: PL at 11.2 K from a series of InGaAlAs/InP heterostructures with different Al concentrations. The four curves correspond to concentrations of (a) y=0, (b) y=0.03, (c) y=0.05, and (d) y=0.07, respectively.

below the gap edge transition in this film suggests that this material suffers from poor crystalline quality. The 0.885 eV contribution was found to saturate almost immediately upon exposure to moderate light levels, and hence it was determined that this emission was not the result of BE recombination. Based on this observation and the relatively narrow FWHM of this peak ($\simeq$ 9.9 meV), it is postulated that this feature results from either (D,h) or (e,A) transitions in the alloy. The weak 0.864 eV emission may be related to a DAP process, while the stronger 0.820 eV transition likely involves a deep defect or vacancy center, characteristic of poor quality, nonuniform material.

In contrast, the PL spectrum of the $In_{0.53}Ga_{0.40}Al_{0.07}As/InP$ heterostructure in Fig. 5.6 (d) is that of a high quality film. The dominant emission of this spectrum, centered at 0.934 eV, has a FWHM of just 10.5 meV. This value is comparable with the narrowest line width ever reported for a conventional MBE-grown InGaAlAs layer in this range [151, 166]. To determine the origin of this emission, its integrated luminescence intensity was measured as a function of both excitation density and sample temperature.

No discernible noise level is observed in any of the spectra recorded in Fig. 5.6 since the intensities of the PL signals collected from the epilayers investigated are very strong. It should be noted that the intensity axes of Figs. 5.6 (a)-(d) were expanded to the point where the noise level became recognizable, and no additional peaks were observed.

Figure 5.7 shows the variation of the luminescence intensity of the 0.934 eV peak as a function of excitation power density. As evident from examination of this figure, the intensity of the peak increases linearly with excitation over three orders of magnitude. Detailed balance calculations by Bimberg *et al.* [167] have shown that this is the expected excitation dependence of BE recombination processes. This fact, in combination with the narrow FWHM of the peak allow the transition to be attributed to BE recombination.

The thermal activation energies of the exciton line at 0.934 eV are determined from the integrated intensity, shown in Fig. 5.8, versus the inverse temperature. Examination of the figure shows that there are two competing ionization mechanisms with different activation energies. The measured temperature dependence is fitted using a simplex-based algorithm [168], to the theoretical expression derived by Bimberg *et al.* [169]

$$\frac{I_T}{I_o} = [1 + C_1 \exp(T_1/T) + C_2 \exp(T_2/T)]^{-1} \tag{5.3}$$

In this expression I_T and I_o are the emission intensities at the temperatures T and $T = 0$ K respectively, C_1 and C_2 are the ratio's of the degeneracies of the BE energy levels, and

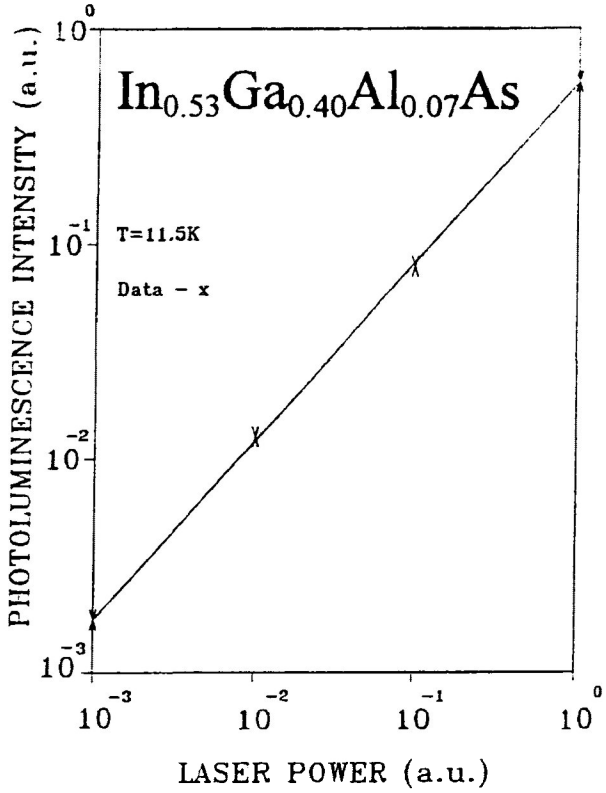

Figure 5.7: Variation of the integrated PL intensity of the main 0.934 eV peak with excitation power density for InGaAlAs/InP sample number 1514.

k_BT_1 and k_BT_2 are activation energies. Good agreement is given between the measured points and Eq. 5.3 with the parameters given in Table 5.6.

The resulting activation energies are $k_BT_1 = 4.7$ meV and $k_BT_2 = 14.3$ meV. It is believed that the first of these, k_BT_1, is associated with a dissociation process in which a free hole and a free electron are created from an acceptor bound exciton (i.e. $(A^o, X) \rightarrow A^o + e + h$). The activation energy related to such a process is given by

$$E_{t_1} = E_x + E_b \tag{5.4}$$

where E_x is the exciton binding energy and E_b is the binding energy of the exciton system to the acceptor site. Linearly interpolating between the exciton binding energies of $In_{0.53}Ga_{0.47}As$ ($E_x = 2.0$ meV) and $In_{0.52}Al_{0.48}As$ ($E_x = 5.1$ meV) (after Ref. [9]), one obtains a value of $E_x = 2.5$ meV for $In_{0.53}Ga_{0.40}Al_{0.07}As$. Hence, setting $k_BT_1 = E_{t_1}$ yields an acceptor binding energy of $E_b = 2.2$ meV. In accordance with Haynes' rule ($E_b/E_A = 0.1$; see Section 2.4.1), this difference may be associated with an acceptor ionization energy of $E_A \simeq 10 \times 2.2$ meV or 22 meV. This value of E_A agrees with the ionization energy of zinc (with $E_A \simeq 22$ meV) as identified in $In_{0.53}Ga_{0.40}Al_{0.07}As$ by Ref. [164] and may be related

Curve	C_1	k_BT_1 (meV)	C_2	k_BT_2 (meV)
1	12	4.7	184	14.3
2	12	4.7	–	–
3	–	–	184	14.3

Table 5.6: Parameters used in the theoretical fit of luminescence intensity vs. inverse temperature data for sample 1514.

to this impurity.

The second activation energy k_BT_2 is much larger and hence is attributed to dissociation of the acceptor bound exciton resulting in two free holes and one free electron. (i.e. $(A^o, X) \rightarrow A^- + h + h + e$). The activation energy associated with this process is given by

$$E_{t_2} = E_x + E_b + E_A \tag{5.5}$$

Setting $k_BT_2 = E_{t_2}$ and applying Haynes' rule again yields an acceptor binding energy given by $E_A \simeq 11$ meV. As the values of E_A obtained in both of these dissociation processes are quite different, it is believed that their initial (A^o, X) complexes do not involve the same neutral acceptor element.

The band gap energy at 11 K as a function of Al concentration (y) is plotted in Fig. 5.9 for the six $In_{1-x-y}Ga_xAl_yAs$ epilayers, lattice-matched to InP substrates, listed in Table 5.5. To obtain the band gap energy of the epilayers from the PL spectra, a total exciton binding energy of $\simeq 5$ meV or an acceptor ionization energy of 11 meV was added to the gap edge peak, depending on its previous assignment. From this graph it is possible to infer that the band gap energy, $E_g(y)$, varies linearly from 0.80 to 0.94 eV with y increasing from 0 to 7% according to

$$E_g(y) = 2.02y + 0.80 \text{ (eV)} \tag{5.6}$$

Clearly this relationship cannot be used to describe the compositional dependence of the band-gap throughout its entire lattice-matched range ($0 \leq y \leq 0.48$) as it predicts a value of $E_g = 1.77$ eV for $In_{0.52}Al_{0.48}As$ ($\sim$ 17% too large, based on $E_g = 1.511$ eV [170]). Hence, this suggests a simple linear dependency is not adequate to accurately describe the band-gap energy versus Al concentration relationship throughout this range. Indirectly, this result agrees with the earlier findings by Böhrer [9], Kopf [158] and Olego [159] and disagrees with those of Praseuth [151], Sacilotti [150], and Hiyamizu [157]. It is noted that in each of these previous studies, just a single data point with $y \leq 7\%$ was used in the

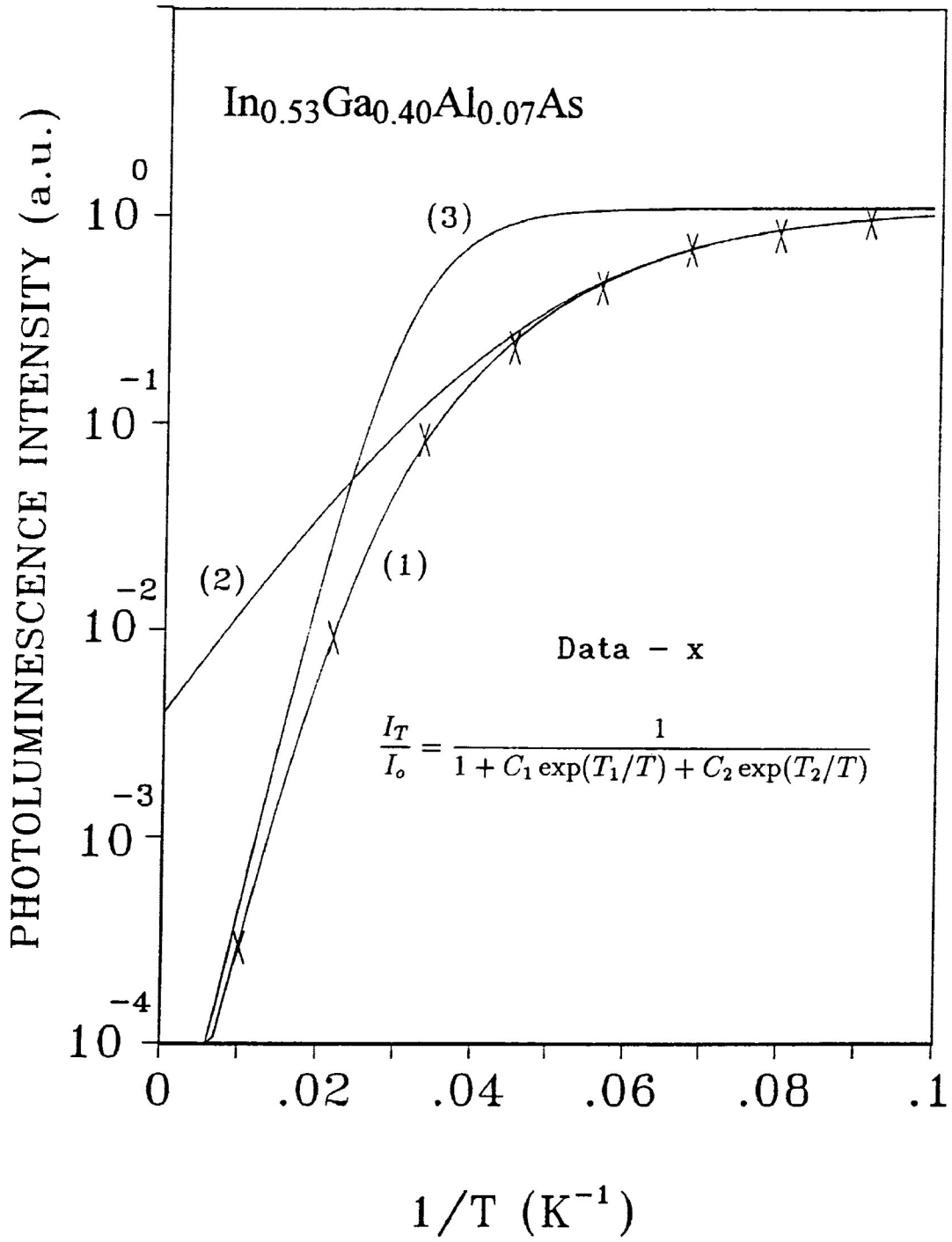

Figure 5.8: Integrated intensity of the exciton line at 0.934 eV for sample number 1514 as a function of 1/T. The experimental points are denoted by x. Curves (1), (2) and (3) are theoretical fits with Eq. 5.3, assuming either one or two activation energies.

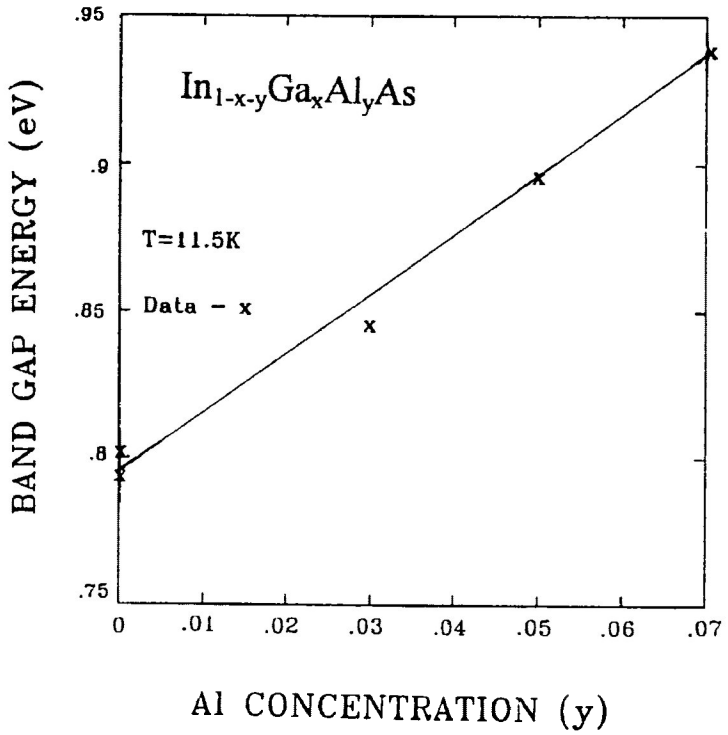

Figure 5.9: Band-gap energy of InGaAlAs deduced from PL spectra as a function of compostion over the range of Al concentration from 0 to 7 percent. The solid line represents a linear fit to the experimental data.

evaluation of the $E_g(y)$ dependency. Thus, the relationship presented in Eq. 5.6 provides the first such investigation of this property for low Al composition $In_{1-x-y}Ga_xAl_yAs/InP$ heterostructures.

5.3.4 Raman Results

Figure 5.10 shows the Raman spectra of five $In_{1-x-y}Ga_xAl_yAs/InP$ heterostructures with Al composition ranging from $0 \leq y \leq 0.48$. The *LO* and *TO* phonon energies for the constituent compounds in this quaternary/substrate heterostructure are given in Table 5.7. While all but one of the spectra have $y \leq 0.07$, the $In_{0.52}Al_{0.48}As/InP$ result was included to depict the AlAs-like modes in the upper y limit of the quaternary system.

The spectra of Fig. 5.10 (a) displays the two-mode type behavior, (i.e. two *LO* modes associated with the respective end compounds) which has been reported [80] for the $In_{1-y}Al_yAs$ ternary over its entire range. Total laser power to the samples of $\leq$ 80 mW and integration times of 800 seconds were used for each scan. The spectra displayed in the figure represent the sum of three such scans. The energies of the peaks at 238.2 and 370.7

Compound	*TO* phonon (cm^{-1})	*LO* phonon (cm^{-1})
InAs	218.5	243.5
GaAs	267.7	285.3
InP	308.1	344.4
AlAs	363.7	401.6

Table 5.7: Phonon energies for selected binary compounds.

cm^{-1} in this spectrum are in good agreement with published values of 241 and 372 cm^{-1} for InAs- and AlAs-like *LO* phonon modes in $In_{1-y}Al_yAs$, respectively [171]. The asymmetry associated with the peaks is characteristic of multi-element alloys and is quite evident in the results of Mestres *et al.* [171] as well. The line widths of these peaks are 12.8 and 7.4 cm^{-1}, respectively. These results are comparable with some of the best values reported for $In_{1-y}Al_yAs$ epilayers [86]. In addition to the *LO* phonon modes, there is evidence in spectrum (a) of two additional emissions centered near 189 and 349 cm^{-1}. These peaks are assigned to scattering by InAs- and AlAs-like *TO* phonon modes. The generation of pairs of binary-like *LO* and *TO* phonon modes in ternary systems is not unique to $In_{1-y}Al_yAs$ and has been well documented in the $Cd_{1-x}Mn_xTe$ material system [172].

It is noted at this point that as the crystal orientation of the epilayers was not known at the time of this study, a polarization dependent Raman scattering analysis of the samples was not performed. Hence, the theory presented in the corresponding sections of chapter 3 were included purely for reasons of completeness.

Near the other end of the Al concentration scale (i.e. $y = 0$) in the $In_{1-x-y}Ga_xAl_yAs$/InP lattice-matched material system is $In_{0.541}Ga_{0.459}As$/InP. The Raman spectrum of this heterostructure is presented in Fig. 5.10 (e). This sample has a Raman signature very similar to that reported in Ref. [81]. In this earlier investigation, Estrera and co-workers used detailed line shape analysis to deconvolve the complicated spectral responses lying in the 210 to 290 cm^{-1} Raman shifted region. This allowed them to identify four features: an InAs-like *LO* phonon (@ 233 cm^{-1}), a GaAs-like *TO* phonon (@ 255 cm^{-1}), a GaAs-like *LO* phonon (@ 270 cm^{-1}), and an alloy disorder related mode (@ 244 cm^{-1}). Similar curve-fitting techniques were applied to the spectrum in Fig. 5.10 (e) and the best fit to the data required the three Lorentzian profiles presented in Fig. 5.11. These peaks, centered at 232, 252 and 270 cm^{-1}, were attributed to InAs-like *LO* phonons, GaAs-like *TO* phonons and GaAs-like *LO* phonons, respectively. It is important to note that the best fit to the data in Fig. 5.10 (e) did not include the 244 cm^{-1} alloy disorder mode present

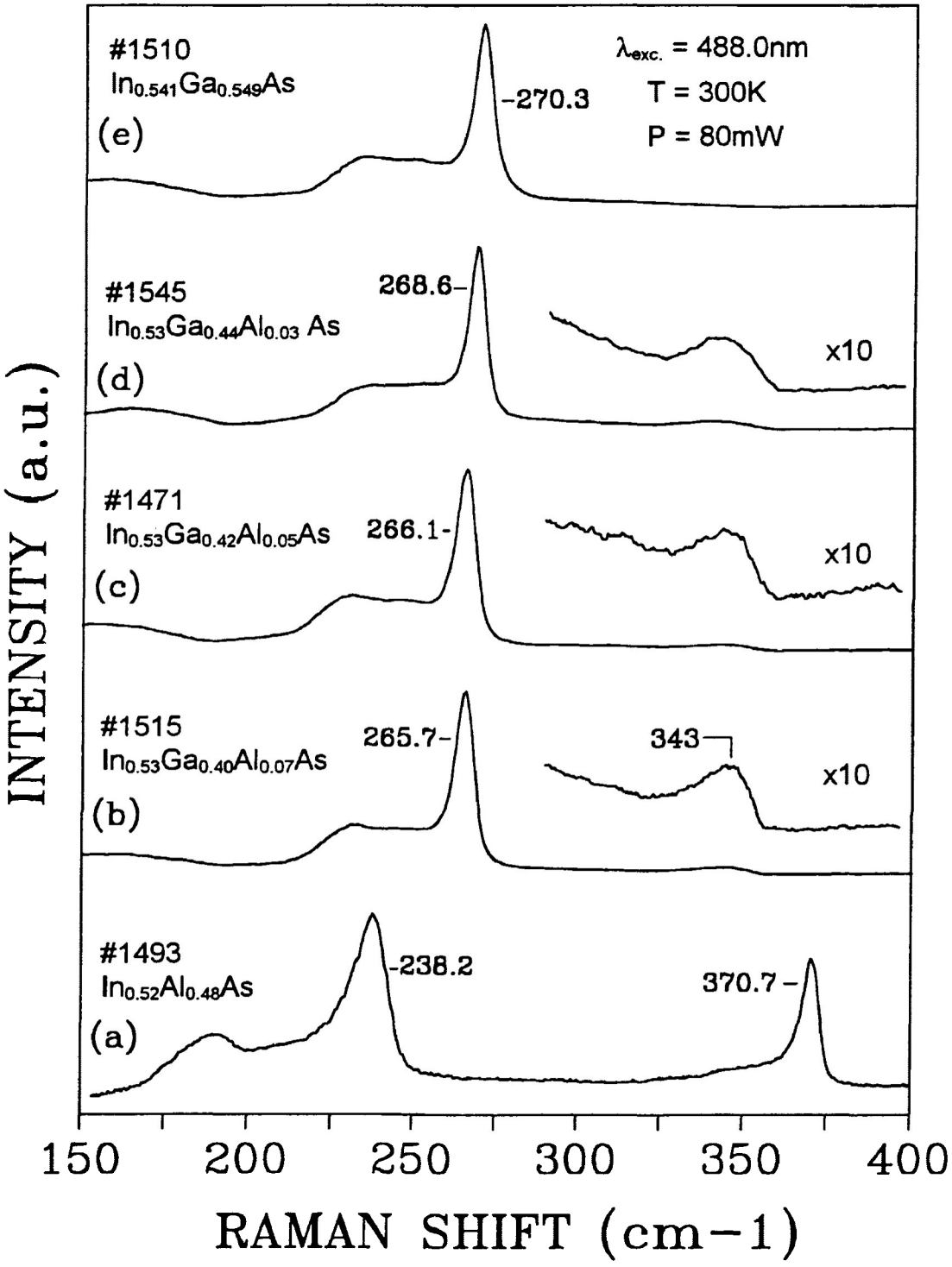

Figure 5.10: Raman spectra obtained at 300 K for InGaAlAs/InP heterostructures with Al concentrations ranging from 0 to 48 percent. The curves correspond to (a) y=0.48, (b) y=0.07, (c) y=0.05, and (d) y=0.

in the work of Estrera *et al.* [81]. This fact, in combination with the narrow FWHM (4.7 meV) of the GaAs-like *LO* phonon peak (a factor of two narrower than that reported in Ref. [81]) suggest that a high quality, low disorder epilayer has been produced.

The remaining three spectra in Figs. 5.10 (b), (c) and (d) correspond to $In_{0.53}Ga_{0.40}Al_{0.07}As/InP$, $In_{0.53}Ga_{0.42}Al_{0.05}As/InP$ and $In_{0.53}Ga_{0.44}Al_{0.03}As/InP$ heterostructures, respectively. All of these samples show Raman modes quite similar to those in the $In_{0.541}Ga_{0.459}As/InP$ spectrum of (e). As the Al concentration of the epilayers increases from 0 to 7%, going from the spectrum in (e) to that in (b), the Raman shift due to the strong GaAs-like *LO* phonon mode decreases by $\simeq 4.5$ cm^{-1}. Also distinguishable in the spectra of figures (b), (c) and (d) is a weak component centered near 343 cm^{-1}. Although this emission occurs near the bulk InP *LO* phonon mode at 344.5 cm^{-1}, there is no evidence for it in the $In_{0.541}Ga_{0.459}As/InP$ spectrum of figure (e) and hence the signal is not believed to originate in the substrate. This contention is supported by the earlier PL results of Section 5.3.3 which showed no discernible emission from the InP in any of the epilayer investigations. Instead, the 343 cm^{-1} structure is attributed to scattering by an AlAs-like *LO* phonon mode.

In the Raman investigation of $In_{1-y}Al_yAs$ by Emura *et al.* [80], the Raman shift associated with the AlAs-like *LO* phonon mode was found to increase linearly with increasing Al composition. Based on the results of this study, a Raman shift of 343 cm^{-1} in the ternary material would correspond to scattering by an AlAs-like *LO* phonon in an $In_{0.92}Al_{0.08}As$ epilayer. Likewise, in the study of $In_{1-x}Ga_xAs$ by Brodsky *et al.* [173], which also displayed evidence of two-mode Raman behavior, the phonon shift associated with the GaAs-like *LO* mode was found to decrease linearly with decreasing Ga concentration. Based on this work, a GaAs-like *LO* phonon mode at 266 cm^{-1} would correspond to scattering in an $In_{0.58}Ga_{0.42}As$ ternary system. Comparing the compositional structure of these two predicted films with that of the quaternary material depicted in Fig. 5.10 (b) one notices a distinct correlation between the Al (y) and Ga (x) concentrations in the three epilayers. The 8% total Al concentration in the predicted $In_{0.92}Al_{0.08}As$ material is very near the 7% value in the film of Fig. 5.10 (b). Similarly, Ga concentrations of 42% and 40% are found corresponding to the predicted $In_{0.58}Ga_{0.42}As$ material and that of Fig. 5.10 (b).

Based on these comparisons it appears, at least in the near ternary case of the quaternary system (i.e. $y \leq 0.07$), as though the Al and Ga atoms in the quaternary mix effectively 'see' each other as In atoms. As a result, the phonon modes in the qua-

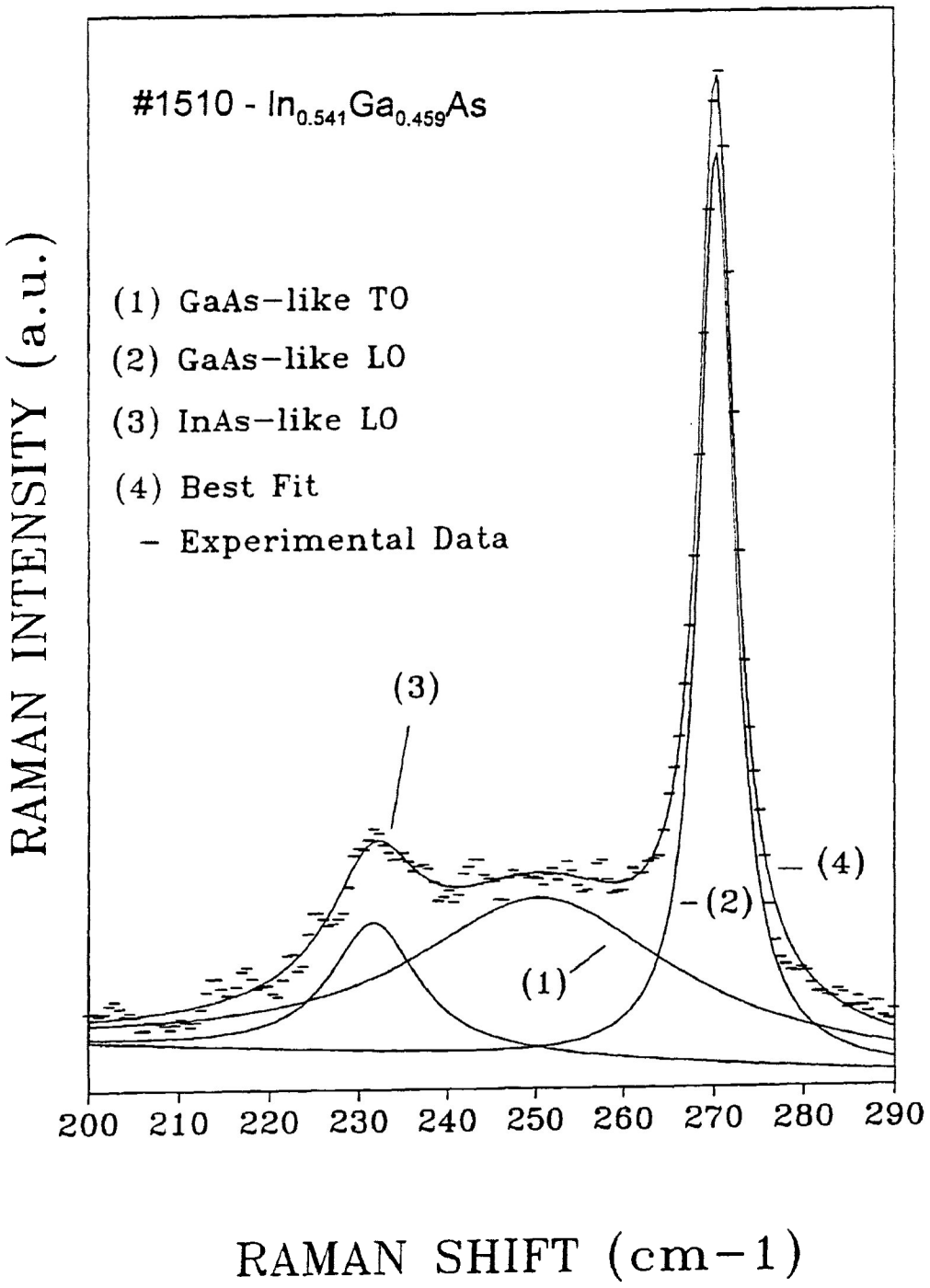

Figure 5.11: Raman intensity of InGaAs/InP sample number 1510. The various phonon components making up the structure are deconvolved and indicated as marked.

ternary heterostructure behave as appropriately weighted ternary constituents, wherein the $In_{1-x-y}Ga_xAl_yAs$ *LO* phonon modes occur at energies defined by the hypothetical ternaries $In_{1+x-y}Al_yAs$ and $In_{1-x+y}Ga_xAs$. Potentially this is an important conclusion, for if it holds true throughout the entire compositional range possible in this alloy, it may provide a quick and simple method of unambiguously determining the proportions of group-III elements in $In_{1-x-y}Ga_xAl_yAs$/InP heterostructures.

Chapter 6

Conclusions

6.1 (111)CdTe/(001)GaAs:Si and (001)CdTe/(001)InSb heterostructures

The photoluminescence emitted from PLEE grown (111)CdTe/(001)GaAs:Si and (001)CdTe/(001)InSb heterostructures has been studied at 11.5 K. Investigations of the CdTe E_o gap region of one of the targets and its corresponding epilayer resulted in the identification of a number of radiative recombination mechanisms. As well as displaying similar donor BE peaks, the PL spectra of the target material and its epilayer both included a strong luminescence signal near 1.47 eV. This emission was associated with excitons bound to extended defects.

Luminescence from the $E_o+\Delta_o$ gaps of both the epilayer and substrate target materials was virtually absent in the heterostructure components (i.e. substrates and targets) before growth and was considerably enhanced by the presence of the interface. As well detecting band-to band recombination directly across the CdTe $\Gamma_6 - \Gamma_7$ gap, PL signal from the $E_o + \Delta_o$ region of one of the epilayers included a significant luminescence component centered near 2.36 eV. Based on its energy position and line width, relative to the 1.47 eV peak, this emission was attributed to transitions occurring between holes in the Γ_7 spin-orbit, split-off valence band and electrons trapped at the same extended defect centers responsible for the 1.47 eV peak. It is believed that this is the first observation using conventional PL techniques of radiative recombination arising from transitions associated with the CdTe Γ_7 band, other than that of direct $\Gamma_6 - \Gamma_7$ transitions.

The enhanced PL signals associated with the $E_o+\Delta_o$ regions of the film and substrate materials seen once the heterojunction is produced underscores the importance of the interface. At least in the case of these mixed II-VI/III-V heterostructures, it appears that interface states produced by differences in species valence, along with high carrier concentrations and or impurity levels in the samples, are sufficiently long lived to promote radiative decay across higher gaps. If this is so, then II-VI/III-V heterostructures developed for optoelectronic transduction should be carefully checked for radiative decay across these higher gap channels since any such decay mechanisms reduce the effective carrier generation efficiency.

6.2 (111)$Cd_{1-x}Mn_xTe$/(111)GaAs:Si heterostructures

The PL spectra from a series of PLEE grown heterojunctions consisting of (111)$Cd_{1-x}Mn_xTe$ epilayers of various Mn concentrations, on heavily Si doped (111)GaAs substrates have been studied. Over the energy range of 2.5 to 0.6 eV, components originating in both the substrate and epilayer regions of the samples were observed. The intensity of the PL from the substrate $E_o+\Delta_o$ gap was found to increase rapidly with growth temperature and time in samples produced at or above T_g = 250 °C. It is believed that the samples grown at these higher temperatures have an improved epilayer crystal quality, a confirmation of earlier Raman results. The PL, starting at the substrate $E_o+\Delta_o$ energy of 1.886 eV in the higher growth temperature samples, is likely enhanced because of an increase in carrier diffusion length in combination with the changes in interface states produced by the mixed II-VI/III-V heterojunction. This allows single carriers and excitons to migrate into the interface region prior to radiative recombination.

The PL signal from Si clusters present in the GaAs substrate, was observed in single peak and double peak forms in the heterojunction spectra. The unannealed substrate and the junction grown at a temperature of 210 °C exhibited the single peak result while junctions grown at higher temperatures produced the double peak form. Substrate annealing experiments showed that the second cluster peak did not develop until a temperature of 500 °C was exceeded. This suggests that during PLEE heterojunction growth the ablation products can transfer a significant amount of energy to the growth surface, hence increasing the effective temperature above T_g at the growth surface.

6.3 $In_{1-x-y}Ga_xAl_yAs$ heterostructures lattice-matched to InP

Preliminary measurements on an important new class of quaternary semiconductor have been reported and the initial results are very encouraging. Raman scattering at 300 K and photoluminescence at 11.5 K from MBE-grown $In_{1-x-y}Ga_xAl_yAs$ epilayers, lattice-matched to InP, have been studied. In most cases, the PL signal from the films exhibit strong, gap-edge BE emissions with line widths comparable to the best published results for this quaternary system. This was interpreted as an indication that high quality MBE-grown films had in fact been produced.

The band-gap $E_g(y)$ dependence of this material system on Al concentration (y) has been investigated over the $0 \leq y \leq 0.07$ region for the first time. Results of this work indicate that over this range a linear relationship, given by $E_g(y) = 2.02y + 0.80$ eV, exists between these two variables. As this equation predicts a value of $E_g(0.48) = 1.77$ eV (17% too large for $In_{0.52}Al_{0.48}As$), it is suggested that a simple linear dependency, as predicted to exist by some authors, is not adequate to describe the relationship throughout the entire lattice-matched range.

Raman scattering results for $In_{1-x-y}Ga_xAl_yAs$ epilayers, over the range $0 \leq y \leq 0.48$, have been presented and all of the spectra obtained for the films exhibited very narrow line widths. This supports the contention that high quality quaternary films have been grown. The phonon modes associated with one of the $In_{0.541}Ga_{0.459}As$/InP heterostructures was examined and detailed line shape analysis was used to deconvolve the complicated spectral responses lying in the 210 to 290 cm^{-1} Raman shifted region. Results of this analysis displayed evidence for GaAs-like LO, InAs-like LO, and GaAs-like TO phonon modes. Unlike earlier studies, no evidence for alloy disorder-related modes was found.

The Raman spectra of the epilayers with Al concentrations corresponding to 3%, 5% and 7%, were very similar to those of the $In_{0.541}Ga_{0.459}As$ films. The prominent GaAs-like LO mode near 270 cm^{-1} in the $In_{0.541}Ga_{0.459}As$ film, shifted to approximately 268.5 cm^{-1} as the Al concentration increased from 0% to 7%. As well, a weak emission near 343 cm^{-1}, not found in the $In_{0.541}Ga_{0.459}As$ epilayers, was evident in the $y \neq 0$ films. This peak was attributed to Raman scattering by AlAs-like LO phonons and is reported for the first time. Studying the Raman shift associated with this mode may prove very useful in determining the proportions of group-III elements in $In_{1-x-y}Ga_xAl_yAs$/InP lattice-matched heterostructures.

Bibliography

[1] G.F. Neumark, in *Widegap II-VI Compounds for Opto-electronic Applications*, edited by H.E. Ruda (Chapman & Hall, London, 1992), pp. 280-294.

[2] J.-i. Nishizawa and K. Suto, in *Widegap II-VI Compounds for Opto-electronic Applications*, edited by H.E. Ruda (Chapman & Hall, London, 1992), pp. 323-350.

[3] P.J. Dean, A.G. Cullis, and A.M. White, in *Handbook on Semiconductors,* edited by T.S. Moss (Elsevier Science Publishing Co., New York, 1987), Vol. 3, p. 144.

[4] I.C. Bassignana, C.J. Miner, and N. Puetz, J. Appl. Phys. **65,** 4299 (1989).

[5] Y. Hirayama, Woo-Young Choi, L.H. Peng, and C.G. Fonstad, J. Appl. Phys. **74**, 570 (1993).

[6] S. Monéger, A. Tabata, C. Bru, G. Guillot, A. Georgakilas, K. Zekentes and G. Halkias, Appl. Phys. Lett. **63**, 1654 (1993).

[7] G.A. Thomas and V.B. Timofeev, in *Handbook on Semiconductors*, edited by T.S. Moss (North Holland, New York, 1986), Vol. 2.

[8] M. Jain, in *Diluted Magnetic Semiconductors*, (World Scientific, New Jersey, 1991).

[9] J. Böhrer, A. Krost, and D.B. Bimberg, Appl. Phys. Lett. **63**, 1918 (1993).

[10] See, for example, W.A. Harrison, *Electronic Structure and the Properties of Solids,* (Freeman, San Francisco, 1980).

[11] G.H. Wannier, Phys. Rev. **52**, 191 (1937).

[12] D.C. Reynolds, T.C. Collins, *Excitons: Their Properties and Uses,* (Academic, New York, 1981).

[13] J.O. Dimmock, in *Semiconductors and Semimetals*, edited by R.K. Willardson and A.C. Beer (Academic Press, Inc., New York, 1967), Vol. 3, pp. 259-319.

[14] See, for example, C. Kittel, *Introduction to Solid State Physics,* (Wiley, New York, 1986), 6th ed., p.193.

[15] D.L. Dexter and R.S. Knox, *Excitons,* (Wiley, New York, 1965).

[16] C.W. Litton et al., Phys. Rev. **B13**, 5392 (1976).

[17] R. Romestain, C. Weisbuch, Phys. Rev. Lett. **45**, 2067 (1980).

[18] G. Beni and T.M. Rice, Phys. Rev. **B18**, 768 (1978).

[19] C. Weisbuch and R.G. Ulbrich, in *Light Scattering in Solids III*, edited by M. Cardona and G. Güntherodt (Springer-Verlag, New York, 1982).

[20] K.K. Smith, Thin Solid Films **84**, 171 (1981).

[21] D.G. Thomas, M. Gershenzon and F.A. Trumbore, Phys. Rev. Lett. **133**, A269 (1964).

[22] E. Zacks and A. Halperin, Phys. Rev. B. **6**, 3072 (1972).

[23] See, for example, H.B. Bebb and E.W. Williams, in *Semiconductors and Semimetals,* edited by R.K. Willardson and A.C. Beer (Academic Press, Inc., New York, 1972), Vol. 8, pp. 299-317.

[24] E.I. Rashba and G.E. Gurgenishvili, Sov. Phys.-Solid State, **4**, 759 (1962).

[25] M. Voos, R.F. Leheny, and J. Shah, in *Handbook on Semiconductors,* edited by T.S. Moss (Elsevier Science Publishing Co., New York, 1986), Vol. 2, p. 361.

[26] E.C. Lightowlers, in *Growth and Characterization of Semiconductors*, edited by R.A. Stradling and P.C. Klipstein (Adam Hilger, Bristol, 1990), pp. 135-163.

[27] J.J. Hopfield, Proc. 7th Int. Conf. on the Physics of Semiconductors (Dunod, Paris, 1964), p.725.

[28] M.L.W. Thewalt, in *Excitons*, edited by E.I. Rashba and M.D. Sturge (North Holland, Amsterdam, 1982). pp. 393-485.

[29] J.M. Francou, K. Saminadayar, J.L. Pautrat, J.P. Gaillard, A. Million, and C. Fontaine, J. Cryst. Growth **72**, 220 (1985).

[30] J.P. Chamonal, E. Molva, and J.L. Pautrat, Solid State Commun. **43**, 801 (1982).

[31] N.C. Giles, J. Lee, D. Rajavel, and C.J. Summers, J. Appl. Phys. **73**, 4541 (1993).

[32] D.M. Hofmann, P. Omling, H.G. Grimmeiss, B.K. Meyer, K.W. Benz, and D. Sinerius, Phys. Rev. B **45**, 6247 (1992).

[33] H.A. Mar and N. Salansky, J. Appl. Phys. **56**, 2369 (1984).

[34] D.K. Schroder, in *Semiconductor Material and Device Characterization*, (John Wiley & Sons, New York, 1990), p. 564.

[35] M. Ekawa, K. Yasuda, T. Ferid, M. Saji, and A. Tanaka, J. Appl. Phys. **72**, 3406 (1992).

[36] J.R. Haynes, Phys. Rev. Lett. **4**, 361 (1960).

[37] J.M. Baranowski, M. Grynberg and S. Porowski, in *Handbook on Semiconductors*, edited by T.S. Moss (Elsevier Science Publishing Co., New York, 1983), Vol. 1, p. 341.

[38] R.E. Halsted and M. Aven, Phys. Rev. Lett. **14**, 64 (1965).

[39] S. Seto, A. Tanaka, Y. Masa, S. Dairaku, and M. Kawashima, Appl. Phys. Lett. **53**, 1524 (1988).

[40] W.J. Choyke, M.G. Burke, Z.C. Feng, M.H. Hanes, and A. Mascarenhas, Defects in Semiconductors - Material Science Forum Volumes 10-12 (1986), pp.769-774.

[41] O. Ka and G. Neu, J. Appl. Phys. **68**, 3386 (1990).

[42] P.M. Amirtharaj and N.K. Dhar, J. Appl. Phys. **67**, 3107 (1990).

[43] J.M. Gilpérez, F. Gonzalez-Sanz, E. Calleja, E. Muñoz, J.M. Calleja, N. Mestres, J. Castagné, and E. Barbier, Semicond. Sci. Technol. **7**, 562 (1992).

[44] S.M. Olsthoorn, F.A.J.M. Driessen, A.P.A.M. Eijkelenboom, and L.J. Giling, J. Appl. Phys. **73**, 7798 (1993).

[45] C. Pickering, P.R. Tapster, P.J. Dean and D.J. Ashen, in *GaAs and Related Compounds 1982*, edited by G.E. Stillman (Inst. Phys., Bristol, 1983), pp. 469-476.

[46] M. Tajima, Appl. Phys. Lett. **32**, 719 (1978).

[47] S. Seto, A. Tanaka, and M. Kawashima, J. Appl. Phys. **64**, 3658 (1988).

[48] G. Landsberg and L. Mandelstam, Naturwiss **16**, 557 (1928).

[49] E. Fermi and F. Rasetti, Z. Phys. **71**, 689 (1931).

[50] R.A. Cowley, in *The Raman Effect*, edited by A. Anderson (Marcel Dekker, New York, 1971), Vol. 1., pp. 95-181.

[51] R. Loudon, Adv. Phys. **13**, 423 (1964).

[52] See for example, *Light Scattering in Solids I*, edited by M. Cardona (Springer-Verlag, New York, 1983).

[53] R. Loudon, Proc. Roy. Soc. (London) **A275**, 218 (1963).

[54] O. Theimer, Can. J. Phys. **34**, 312 (1956).

[55] See for example, H.C. Ohanian, in *Principles of Quantum Mechanics*, (Prentice-Hall, New Jersey, 1990), p. 292.

[56] B. Kursunogla, in *Modern Quantum Theory*, (W.H. Freeeman, San Francisco, 1962).

[57] M. Born and K. Huang, in *Dynamical Theory of Crystal Lattices*, (Oxford University, Great Britian, 1968).

[58] See for example, F. Reif, in *Fundamentals of Statistical and Thermal Physics*, (McGraw-Hill, New York, 1965).

[59] J.L. Birman, in *Theory of Crystal Space Groups and Lattice Dynamics* (Springer-Verlag, Berlin, 1974).

[60] L.A. Woodward, in *Intoduction to the Theory of Molecular Vibrations and Vibrational Spectroscopy*, (Oxford University Press, Great Britian, 1972).

[61] G. Burns and A.M. Glazer, in *Space Groups for Solid State Scientists*, (Academic, Boston, 1990).

[62] L.D. Landau and E.M. Lifshitz, in *Statistical Physics*, (Permagon, London, 1958), p.153.

[63] M. Cardona, in *Light Scattering in Solids II*, edited by M. Cardona and G. Güntherodt, (Springer-Verlag, New York, 1982), pp. 19-178.

[64] R.M. Martin and L.M. Falicov, in *Light Scattering in Solids I*, edited by M. Cardona (Springer-Verlag, New York, 1983), pp. 79-146.

[65] A. Vincent, in *Molecular Symmetry and Group Theory*, (Wiley, London, 1977).

[66] V.V.J.S. Nyayapathi and M.A. Samuel, in *Group Theory Made Easy for Scientists and Engineers*, (Wiley, New York, 1979).

[67] C.J.H. Schutte, in *The Theory of Molecular Spectroscopy*, (North-Holland, Amsterdam, 1976), Vol. 1.

[68] G.F. Koster, in *Solid State Physics,* edited by F. Seitz and D. Turnbull (Academic, New York, 1957), Vol. V.

[69] R.A. Cowley, Phys. Rev. **134**, A981 (1964).

[70] A.A. Maradudin and S.H. Vosko, Rev. Mod. Phys. **40**, 1 (1968).

[71] J.L. Warren, Rev. Mod. Phys. **40**, 38 (1968)

[72] R. Savoie, in *The Raman Effect*, edited by A. Anderson (Marcel Dekker, New York, 1973), Vol. 2., pp. 759-810.

[73] G.R. Wilkinson, in *The Raman Effect*, edited by A. Anderson (Marcel Dekker, New York, 1973), Vol. 2., pp. 811-983.

[74] R.C. Newman, in *Growth and Characterization of Semiconductors*, edited by R.A. Stradling and P.C. Klipstein (Adam Hilger, Bristol, 1990).

[75] D.J. Lockwood, in *Light Scattering in Solids III*, edited by M. Cardona and G. Güntherodt (Springer-Verlag, Berlin, 1982).

[76] P. Grünberg, in *Light Scattering in Solids V*, edited by M. Cardona and G. Güntherodt (Springer-Verlag, Berlin, 1989).

[77] G. Abstreiter, M. Cardona, and A. Pinczuk, *Light Scattering in Solids IV*, edited by M. Cardona and G. Güntherodt (Springer-Verlag, Berlin, 1984).

[78] S. Nakashima and M. Hangyo, IEEE J. Quant. Electron. **25**, 965 (1989).

[79] F.H. Pollack and R. Tsu, Proc. SPIE **452**, 26 (1983).

[80] S. Emura, T. Nakagawa, S. Gonda, and S. Shimizu, J. Appl. Phys. **62**, 4632 (1987).

[81] J.P. Estrera, P.D. Stevens, R. Glosser, W.M. Duncan, Y.C. Kao, H.Y. Liu, E.A. Beam III, Appl. Phys. Lett. **61**, 1927 (1992).

[82] G. Landa, R. Carles, C. Fontaine, E. Bedal, and A. Muñoz-Yagüe, J. Appl. Phys. **66**, 196 (1989).

[83] G. Burns, C.R. Wie, F.H. Dacol, D. Pettit, and J.M. Woodall, Appl. Phys. Lett. **51**, 1919 (1987).

[84] A. Krost, W. Richter, D.R.T. Zahn, and O. Brafman, Semicond. Sci. Technol. **6**, A109 (1991).

[85] W.J. Keeler, H. Huang, and J.J. Dubowski, Phys. Rev. B **42**, 11335 (1990).

[86] D.F. Welch, G.W. Wicks, L.F. Eastman, P. Parayanthal, and F.H. Pollak, Appl. Phys. Lett. **46**, 169 (1985).

[87] D. Olego, T.Y. Chang, E. Silberg, A. Caridi, and A. Pinczuk, Inst. Phys. Conf. Ser. **65**, Ch. 3, 195 (1983).

[88] P. Parayanthal and F.H. Pollak, Phys. Rev. Lett. **52**, 1822 (1984).

[89] D. Lamarre and F. Baudais (Bomem Inc.), in "The MB Series FT-IR Optical Design from Bomem Inc.", Doc. Number: MB8904 (1990).

[90] C. Lafond, F. Baudais (Bomem Inc.), in "A New High-Throughput FT-IR Interface Card; Description & New Application Opportunities", Doc. Number: MB8906 (1990).

[91] A. Long, in *Raman Spectroscopy*, (McGraw-Hill, Great Britain, 1977), p. 138.

[92] (Jobin Yvon, Instruments SA, Inc.) "HR-640 Operators Manual" (1987).

[93] (Hamamatsu Corporation) "Photon Counters and Related Products" Cat. No. A5-126 (1985).

[94] See for example, *Widegap II-VI Compounds for Opto-electronic Applications*, edited by H.E. Ruda (Chapman & Hall, London, 1992).

[95] A. Nurmikko, Laser Focus World **29**, 16 (1993).

[96] J. Ren, Y. Lansari, and Z. Yu, J. Electron. Mater. **22**, 973 (1993).

[97] Selection of papers presented at the 34th Electronic Materials Conference, Massachusetts Institute of Technology (MIT) in 1992) J. Electron. Mater. **22**, 429 (1993).

[98] P. Gupta, K.K. Chattopadhyay, and S. Chaudhuri, J. Mater. Sci. **28**, 496 (1993).

[99] J. Gutowski, Semicond. Sci. Technol. **6**, A51 (1991).

[100] L.A. Kolodziejski, R.L. Gunshor, and N. Otsuka, J. Quantum Electron. **22**, 1666 (1986).

[101] M.A. Kinch and M.W. Goodwin, J. Appl. Phys. **58**, 4455 (1985).

[102] A. Waag, Y.S. Wu, R.N. Bicknell-Tassius, C. Gonser-Buntrock, and G. Landwehr, J. Appl. Phys. **68**, 212 (1990).

[103] J.J. Dubowski, D.F. Williams, J.M. Wrobel, P.B. Sewell, J. LeGeyt, C. Halpin, and D. Todd, Can. J. Phys. **67**, 343 (1989).

[104] G.M. Williams, C.R. Whitehouse, and T. Martin, J. Appl. Phys. **63**, 1526 (1988).

[105] T.D. Golding, M. Martinka, and J.H. Dinan, J. Appl. Phys. **64**, 1873 (1988).

[106] C.H. Wang, K.Y. Cheng, and S.J. Yang, J. Appl. Phys. **58**, 757 (1985).

[107] G.M. Williams, C.R. Whitehouse, N.G. Chew, G.W. Blackmore and A.G. Cullis, J. Vac. Sci. Technol. **B3**, 704 (1985).

[108] T.W. Kim, Y.H. Chang, Y.D. Zheng, A.A. Reeder, B.D. McCombe, R.F.C. Farrow, T. Temofonte, F.A. Shirland, and A. Noreika, J. Vac. Sci. Technol. **B5**, 980 (1987).

[109] R.G. van Welzenis and B.K. Ridley, Solid-State Electron. **27**, 113 (1984).

[110] See for example, C. Weisbuch and B. Vinter, in *Quantum Semiconductor Structures*, (Academic, San Diego, 1991).

[111] J.J. Dubowski, J. Cryst. Growth **101**, 105 (1990).

[112] Z.C. Feng, S. Perkowitz, J.M. Wrobel, and J.J. Dubowski, Phys. Rev. B **39**, 12997 (1989).

[113] W.J. Keeler and J.J. Dubowski, Can. J. Phys. **69**, 255 (1991).

[114] Z.C. Feng, S. Perkowitz, J.M. Wrobel, and J.J. Dubowski, J. Appl. Phys. **69**, 7782 (1991).

[115] J.J. Dubowski, Acta Physica Polonica A **80**, 221 (1991).

[116] J.M. Wrobel and J.J. Dubowski, in *Semiconductor Interfaces and Microstructures*, edited by Z.C. Feng (World Scientific, Singapore, 1992).

[117] D.R.T. Zahn, R.H. Williams, T.D. Golding, J.H. Dinan, K.J. Mackey, J. Geurts and W. Richter, Appl. Phys. Lett. **53**, 2409 (1988).

[118] D.R.T. Zahn, W. Richer, T. Eickhoff, J. Geurts, T.D. Golding, J.H. Dinan, K.J. Mackey and R.H. Williams, Appl. Surf. Sci. **41/42**, 497 (1989).

[119] M. Suezawa, A. Kasuya, Y. Nishina, and K. Sumino, in *The Twentieth Annual Conference on the Physics of Semiconductors*, Vol. 1, edited by E.M. Anastassiakis and J.D. Joannopoulos (World Scientific, Singapore, 1990), p. 678.

[120] S. Suga, K. Cho, P. Hiesinger, and T. Koda, J. Lumin. **12/13**, 109 (1976).

[121] J.P. Noblanc, J. Loudette, and G. Duraffourge, J. Lumin. **1, 2**, 528 (1970).

[122] H.H. Woodbury and M. Aven, Phys. Rev. B. **9**, 5195 (1974).

[123] Z.C. Feng, M.J. Bevan, M.J. Choyke, and S.V. Krishnaswamy, J. Appl. Phys. **64**, 2595 (1988).

[124] R.E. Halstead, M.R. Lorenz, and B. Segall, J. Phys. Chem. Solids **22**, 109 (1961).

[125] E. Molva, J.P. Chamonal, and J.L. Pautrat, Phys. Status Solidi B **109**, 635 (1982).

[126] C. Onodera and T. Taguchi, J. Cryst. Crowth **101**, 502 (1990).

[127] P.J. Dean, G.M. Williams, and G.B. Blakmore, J. Phys. D (Appl. Phys.) **17**, 2291 (1984).

[128] K. Ohba, T. Taguchi, Ch. Onodera, Y. Hiratate, and A. Hiraki, Japan. J. Appl. Phys. **28**, 1246 (1989).

[129] E. Molva, K. Saminadayar, J.L. Pautrat, and E. Ligeon, Solid State Commun. **48**, 955 (1983).

[130] D.J. Olego and J.P. Faurie, Phys. Rev. B **33**, 7357 (1986).

[131] J.A. Van Vechten, in *Handbook on Semiconductors*, edited by T.S. Moss (North-Holland, Amsterdam, 1987), Vol. 3., p.44.

[132] *Semimagnetic Semiconductors and Diluted Magnetic Semiconductors*, edited by M. Averous and M. Balkanski (Plenum, New York, 1991).

[133] *Semiconductors and Semimetals*, R.K. Willardson and A.C. Beer, Treatise Editors; J.K. Furdyna and J. Kossut, Volume Editors (Academic, Boston, 1988), Vol. 25.

[134] A.E. Turner, R.L. Gunshor, and S. Datta, Appl. Opt. **22**, 3152 (1983).

[135] N. Kullendorff and B. Hök, Appl. Phys. Lett. **46**, 1016 (1985).

[136] J. Stankiewicz and W. Giriat, in *Proceedings of the 15th IEEE Photovoltaic Specialists Conference* (IEEE, New York, 1981).

[137] D.L. Dreifus, R.M. Kolbas, R.L. Harper, J.R. Tassitino, S. Hwang, and J.F. Schetzina, Appl. Phys. Lett. **53**, 1279 (1988).

[138] J.J. Dubowski, K. Lebecki and M. Buchanan, in Proc. of the IEEE Instr. Meas. Technol. Conf. (Irvine, 1993).

[139] W.A. Harrison, E.A. Kraut, J.R. Waldrop, and R.W. Grant, Phys. Rev. **B6**, 4402 (1978).

[140] J.J. Farrell, M.C. Tamargo, J.L. de Miguel, F.S. Turco, D.M. Hwang, and R.E. Nahory, J. Appl. Phys. **69**, 7021 (1991).

[141] W.J. Keeler, D.A. Harrison, and J.J. Dubowski, J. Appl. Phys. **75**, 3045 (1994).

[142] J. Lagowski, H.C. Gatos, C.H. Kang, M. Skowronski, K.Y. Ko, and D.G. Lin, Appl. Phys. Lett. **49**, 892 (1986).

[143] J.J. Dubowski, J.M. Wrobel, J.A. Jackman, and P. Becla, Mater. Res. Soc. Symp. **131**, 143 (1989).

[144] M. Bugajski, P. Becla, P.A. Wolff, and D. Heiman, Phys. Rev. B **38**, 10512 (1988).

[145] L.R. Ram-Mohan and P.A. Wolff, Phys. Rev. B **38**, 1330 (1988).

[146] Y.R. Lee, A.K. Ramdas, and R.L. Aggarwal, Phys. Rev. B **38**, 10600 (1988).

[147] C.R. Pidgeon, in *Handbook on Semiconductors*, edited by T.S. Moss (North-Holland, Amsterdam, 1986), Vol. 2.

[148] Y. Petroff, in *Handbook on Semiconductors*, edited by T.S. Moss (North-Holland, Amsterdam, 1986), Vol. 2.

[149] H.C. Casey, Jr. and M.B. Panish, in *Heterostucture Laser, Part B* (Academic, New York, 1978).

[150] M. Sacilotti, F. Motisuke, Y. Monteil, P. Abraham, F. Iikawa, C. Montes, M. Furtado, L. Horiuchi, R. Landers, J. Morais, L. Cardoso, J. Decobert, and B. Waldman, J. Cryst. Growth **124**, 589 (1992).

[151] J.P. Praseuth, M.C. Joncour, M. Gérard, P. Hénoc, and M. Quillec, J. Appl. Phys. **63**, 400 (1988).

[152] C.E. Zah, R. Bhat, F.J. Favire, M. Koza, T.P. Lee, D. Darby, D.C. Flanders, and J.J. Hsieh, Electron. Lett. **28**, 2323 (1992).

[153] M. Allovon and M. Quillec, IEE Proc.-J **139**, 148 (1992).

[154] R.E. Eppenga and M.F.H. Schuurmans, Philips Tech. Rev. **44**, 137 (1988).

[155] Y. Kamamura, H. Asahi, and K. Wakita, Electron. Lett. **20**, 459 (1984).

[156] G. Bastard, E.E. Mendez, L.L. Chang, and L. Esaki, Phys. Rev. B **28**, 3241 (1983).

[157] S. Hiyamizu, T. Fujii, S. Muto, T. Inata, Y. Nakata, Y. Sugiyama, and S. Sasa, J. Cryst. Growth, **81**, 349 (1987).

[158] R.F. Kopf, M.H. Herman, M. Lamont Schnoes, A.P.Perley, G. Livescu, and M. Ohring, J. Appl. Phys. **71**, 5004 (1992).

[159] D. Olego, T.Y. Chang, E. Silberg, E.A. Caridi, and A. Pinczuk, Appl. Phys. Lett. **41**, 476 (1982).

[160] L.L. Chang, in *Handbook on Semiconductors*, edited by T.S. Moss (Elsevier Science Publishing Co., New York, 1987), Vol. 3, Ch. 9.

[161] M.A. Herman and H. Sitter, in *Molecular Beam Epitaxy*, (Springer-Verlag, New York, 1989).

[162] J.Y. Tsao, in *Materials Fundamentals of Molecular Beam Epitaxy*, (Academic, Boston, 1993).

[163] Z.R. Wasilewski (private communication).

[164] K.-H. Goetz, D. Bimberg, A.V. Solomonov, G.F. Glinskii, and M. Razeghi, J. Appl. Phys. **54**, 4543 (1983).

[165] A.T. Macrander and V. Swaminathan, J. Electrochem. Soc. **134**, 1247 (1987).

[166] T. Fujii, Y. Nakata, Y. Sugiyama, and S. Hiyamizu, Jpn. J. Appl. Phys. **25**, L254 (1986).

[167] D. Bimberg, M. Sondergeld, W. Schairer, and T.O. Yep, J. Lumin. **3**, 175 (1970)

[168] See for example, J.A. Nelder and R. Mead, Computer Journal, **7**, 308 (1965).

[169] D. Bimberg, M. Sondergeld, and E. Grobe, Phys. Rev. B **4**, 3451 (1971).

[170] Y. Kawamura, H. Asahi, and K. Wakita, Electron. Lett. **20**, 459 (1984).

[171] N. Mestres, L. Viña, A. Manescau, E. Calleja, B. Koiller, P. Daste, and P. Riglet, Solid State Commun. **78**, 835 (1991).

[172] S. Venugopalan, A. Petrou, R.R. Galazka, A.K. Ramdas, and S. Rodriguez, Phys. Rev. B. **25**, 2681 (1982).

[173] M.H. Brodsky and G. Lucovsky, Phys. Rev. Lett. **21**, 990 (1968).